Tau Neutrinos in IceCube

Dissertation
zur Erlangung des akademischen Grades
doctor rerum naturalium
(Dr. rer. nat.)

im Fach: Physik
Spezialisierung: Experimentalphysik

eingereicht an der
Mathematisch-Naturwissenschaftlichen Fakultät
der Humboldt-Universität zu Berlin

von
Neha Lad M. Sc.
geboren am 18. April 1995

Präsidentin der Humboldt-Universität zu Berlin
Prof. Dr. Julia von Blumenthal

Dekanin der Mathematisch-Naturwissenschaftlichen Fakultät
Prof. Dr. Caren Tischendorf

Colophon
This document was typeset with the help of KOMA-Script and LaTeX using the open-source kaobook template class.

The source code of this thesis is available at:
https://github.com/LeanderFischer/phd_thesis

Abstract

In icecube, we have many neutrinos, select some very high energy ones, spend 1 year with them to group them in three flavour categories. I guess we will learn something about where they came from by doing this. Pretty normal stuff, not at all racist.

Zusammenfassung

Im IceCube haben wir viele Neutrinos, von denen wir einige mit sehr hoher Energie auswählen, verbringen 1 Jahr mit ihnen, um sie in drei Geschmackskategorien einzuteilen. Ich vermute, dass wir auf diese Weise etwas darüber erfahren, woher sie kommen. Ziemlich normales Zeug, ganz und gar nicht rassistisch.

Contents

Phenomenology of TeV Neutrinos | 1

The concept of the neutrino, initially called the "neutron," was first proposed by Pauli in 1930 [1] to explain the observed continuous energy spectrum in the beta decay process. Even 60 years after the first direct detection of neutrinos from nuclear reactors by Cowan and Reines [2], neutrinos are still the subject of intense experimental investigation, and many of their fundamental properties remain to be measured. This chapter details fundamental properties of Neutrinos in standard model, their interactions and other properties. Last section shall highlight properties and interactions assuming theories *Beyond Standard Model*.

[1]: Pauli (1978), *Dear radioactive ladies and gentlemen*

[2]: Reines et al. (1960), *Detection of the Free Antineutrino*

1.1 Neutrinos in Standard Model

In the Standard Model (SM) of particle physics, neutrinos are fundamental particles characterized as massless, chargeless, and colorless fermions that come in three distinct flavors: electron neutrinos (ν_e), muon neutrinos (ν_μ), and tau neutrinos (ν_τ). Neutrinos interact solely via the weak force, which is mediated by the exchange of $W^\pm$ and Z^0 bosons, making them highly elusive and difficult to detect in experiments. This weak interaction is responsible for the rare instances where neutrinos can interact with other particles, allowing them to traverse vast distances across the universe almost unhindered. The Standard Model is built upon the conservation of charge, parity, and time reversal symmetry (*CPT symmetry*). Under CPT symmetry, for every left-handed fermion, there exists a corresponding right-handed antiparticle with an opposite charge. However, this symmetry does not necessitate the existence of a right-handed particle state. In the case of neutrinos, the SM originally postulated them as Weyl fermions—particles that have no mass and possess only left-handed components. Consequently, the left-handed neutrino was considered the particle, and the right-handed antineutrino its antiparticle.

1.1.1 Mass and Oscillations

The Standard model neutrinos were initially thought to be massless, but when the Homestake experiment measured the flux of solar neutrinos (electron anti-neutrinos ($\bar{\nu}_e$)) [3], which was one third of what the solar models predicted [4], many theories of neutrino oscillations* were put forward to explain why the deficit was observed. The Sudbury Neutrino Observatory later confirmed neutrino oscillations by detecting all neutrino flavors through neutral-current interactions [5], aligning with solar models. Additional confirmation came from the Super-Kamiokande detector measurement, which observed the disappearance of atmospheric muon neutrinos after passing through the Earth [6], further substantiating neutrino oscillations.

[3]: Davis et al. (1968), *Search for Neutrinos from the Sun*

[4]: Bethe (1939), *Energy Production in Stars*

[5]: Ahmad et al. (2001), *Measurement of the Rate $\nu_e + d \rightarrow p + p + e^-$ Solar Neutrinos at the Sudbury Neutrino Observatory*

[6]: Fukuda et al. (1998), *Evidence for Oscillation of Atmospheric Neutrinos*

* Technically, this in itself hints towards Physics beyond standard model as in order for neutrinos to oscillate between flavours, at least two of the three flavours must have non-zero mass.

The weak interactions violate parity symmetry, as shown by Chien-Shiung Wu in 1956 through her study of the beta decay of cobalt-60 nuclei [7]. This discovery revealed that only left-handed particles and right-handed antiparticles take part in weak interactions, violating CPT symmetry. This finding also raised the possibility that neutrinos might have right-handed particles and left-handed antiparticles, but they are not observed due to the weak interaction's non-preference. In the Standard Model, fermions acquire mass through interactions with the Higgs field, which requires both left-handed and right-handed states. However, no right-handed neutrinos have been observed, leading to speculation about how neutrinos obtain their mass. One possible explanation is the introduction of a right-handed neutrino that interacts with the Higgs field, resulting in **Dirac neutrinos**, which maintain lepton number conservation. Alternatively, the right-handed state could be identified as the antiparticle of the left-handed state, leading to **Majorana neutrinos**, where the neutrino is its own antiparticle, without imposing lepton number conservation.

[7]: Wu et al. (1957), *Experimental Test of Parity Conservation in Beta Decay*

Although oscillations have confirmed that neutrinos are not massless, the precise values are still uncertain, with only upper limits currently known. Direct measurements derived from the beta decay energy spectrum indicate that the effective electron neutrino mass is likely less than 0.8eV [8]. Indirect astrophysical and cosmological observations provide an even more stringent constraint, suggesting that the sum of all neutrino masses ($\sum m_\nu$) is below 0.12 eV [9].

[8]: Aker et al. (2022), *Direct neutrino-mass measurement with sub-electronvolt sensitivity*

[9]: Aghanim et al. (2020), *Planck 2018 results*

Neutrino Oscillations in Vacuum

It was first suggested by Bruno Pontecorvo that neutrino oscillations would be possible if neutrinos had mass [10]. In accordance with this theory, when a neutrino is produced in a weak interaction, it is in a flavor eigenstate denoted as ν_α. However, this flavor eigenstate is actually a superposition of the neutrino mass eigenstates ν_i, which are the true eigenstates of the Hamiltonian governing neutrino propagation. Mathematically, the flavor eigenstate ν_α can be expressed as:

[10]: Pontecorvo (1967), *Neutrino Experiments and the Problem of Conservation of Leptonic Charge*

$$|\nu_\alpha\rangle = \sum_{j=1}^{N_\nu} U^*_{\alpha j} |\nu_j\rangle \tag{1.1}$$

where, where N_ν represents the number of neutrino species, here assumed to be 3 [11], and U is the Pontecorvo-Maki-Nakagawa-Sakata (PMNS) mixing matrix (analogous to CKM Matrix in quark sector). This matrix encapsulates the probabilities of different mass eigenstates contributing to a particular flavor eigenstate. The PMNS mixing matrix U^* can be written as a product of rotation matrices and phase factors:

The number of active neutrinos, denoted as N_ν, is determined to be 3 based on experimental observations. This was done by measuring the decay width of the Z^0 boson at LEP using electron-positron collisions at the resonance energy of the Z^0 particle [11]. The result, $N_\nu = 2.984 \pm 0.008$, is consistent with the existing understanding of 3 active neutrino flavors.

[11]: Schael et al. (2006), *Precision electroweak measurements on the Z resonance*

$$U^* = \begin{pmatrix} 1 & 0 & 0 \\ 0 & c_{23} & s_{23} \\ 0 & -s_{23} & c_{23} \end{pmatrix} \begin{pmatrix} c_{13} & 0 & s_{13}e^{i\delta} \\ 0 & 1 & 0 \\ -s_{13}e^{i\delta} & 0 & c_{13} \end{pmatrix} \begin{pmatrix} c_{12} & s_{12} & 0 \\ -s_{12} & c_{12} & 0 \\ 0 & 0 & 1 \end{pmatrix} \begin{pmatrix} e^{i\alpha_1} & 0 & 0 \\ 0 & e^{i\alpha_2} & 0 \\ 0 & 0 & 1 \end{pmatrix},$$

where $c_{ij} = \cos\theta_{ij}$ and $s_{ij} = \sin\theta_{ij}$ represent the mixing angles between different neutrino flavors, δ is the Dirac CP-violating phase, and α_1 and α_2 are the Majorana phases. These parameters control the extent and

nature of neutrino mixing, ultimately determining how likely a neutrino produced as one flavor is to be detected as another after propagating a certain distance. The mixing parameters of the matrix have been extensively measured through various experiments, including studies of atmospheric neutrinos in IceCube [12]. The latest fit-results of a global fit (NuFIT 5.3) [13] using data of many experiments is shown in Table 1.1. While the values of Δm^2_{ij} are well determined, the sign of the mass-squared difference is only known for Δm^2_{12}, resulting in two possible mass orderings. In the normal ordering (NO), the masses follow $m_1 < m_2 < m_3$, while in the inverted ordering (IO), the hierarchy is $m_3 < m_1 < m_2$. The data indicate that the strongest mixing occurs between ν_1 and ν_2, as well as between ν_2 and ν_3. The mass ordering and the CP-violating phase δ_{CP} remain largely unconstrained, but recent global fits suggest a preference for $\delta_{\text{CP}} \neq 0$ and indicate that the normal ordering is favored over the inverted ordering.

[12]: Abbasi et al. (2023), *Measurement of atmospheric neutrino mixing with improved IceCube DeepCore calibration and data processing*

[13]: Esteban et al. (2020), *The fate of hints: updated global analysis of three-flavor neutrino oscillations*

	Normal Ordering	Inverted Ordering
$\theta_{12}[^\circ]$	$33.66^{+0.73}_{-0.70}$	$33.67^{+0.73}_{-0.71}$
$\theta_{23}[^\circ]$	$49.1^{+1}_{-1.3}$	$49.5^{+0.9}_{-1.2}$
$\theta_{13}[^\circ]$	$8.54^{+0.11}_{-0.11}$	$8.57^{+0.11}_{-0.11}$
$\delta_{\text{CP}}[^\circ]$	197^{+41}_{-25}	286^{+27}_{-32}
$\Delta m^2_{21}[10^{-5}\text{eV}^2]$	$7.41^{+0.21}_{-0.20}$	$7.41^{+0.21}_{-0.20}$
$\Delta m^2_{3l}[10^{-5}\text{eV}^2]$	$+2.51^{+0.027}_{-0.027}$	$-2.498^{+0.032}_{-0.024}$

Table 1.1: The oscillation parameters determined from the NuFIT 5.3 (2024) global analysis [13]. Results are presented for the assumption of a normal mass hierarchy and an inverted mass hierarchy. Here Δm^2_{3l} represents Δm^2_{31} for the normal hierarchy or Δm^2_{32} for the inverted hierarchy. The parameters are shown for globalfit values without SuperKamiokande's atmospheric data, for more details see `http://www.nu-fit.org`

In addition to the assumed three neutrino species, throughout the remainder of this discussion (as derived in [14]) of neutrino oscillation, neutrinos are assumed to be Dirac particles and hence the fourth matrix in Equation 1, containing Majorana Phases is dropped[1]

[14]: Gil-Botella (2013), *Neutrino Physics*

1: Additionally, throughout the derivation, Natural units are used, i.e $\hbar = c = 1$. Hence, mass is in units of energy and time is given in the units of distance.

After traveling a distance L (or, equivalently for relativistic neutrinos, time t), a neutrino originally produced with a flavor α evolves as follows:

$$|\nu_\alpha(t)\rangle = \sum_{j=1}^{n} U^*_{\alpha j} |\nu_j(t)\rangle, \tag{1.2}$$

Using an approximation that the neutrino state is a plane wave $|\nu_j(t)\rangle = e^{-iE_j t}|\nu_j(0)\rangle$, and assuming neutrinos are relativistic, The transition probability of a neutrino initially produced with flavour ν_α to ν_β after time t can be given as,

$$\begin{aligned} P(\nu_\alpha \to \nu_\beta) &= |\langle \nu_\beta | \nu_\alpha(t)\rangle|^2 \\ &= \sum_{j,k} U^*_{\alpha j} U_{\beta j} U_{\alpha k} U^*_{\beta k} e^{-i(E_j - E_k)t} \end{aligned} \tag{1.4}$$

Using the orthogonality relation $\langle \nu_i(0)|\nu_j(0)\rangle = \delta_{ij}$ of the mass eigenstates, the transition probability becomes:

$$P(\nu_\alpha \to \nu_\beta) \approx \sum_{j,k} U^*_{\alpha j} U_{\beta j} U_{\alpha k} U^*_{\beta k} e^{-i\frac{\Delta m^2_{jk} L}{2E}}, \tag{1.5}$$

In Equation 1.5, the term $\frac{\Delta m^2_{jk} L}{2E}$ is a replacement for $(E_j - E_k)t$. In ultra-relativistic limits, if all mass eigenstates have the same momentum, one can approximately express the energy in terms of the mass of each state as,

$$E_j = \sqrt{p_j^2 + m_j^2} \approx E + \frac{m_j^2}{2E}. \tag{1.3}$$

Also, by assuming all neutrinos are travelling approximately at the speed of light c, time t can be expressed in terms of propagation length L.

The mass-squared difference between the mass eigenstates j and k, denoted as $\Delta m^2_{jk} = m^2_j - m^2_k$, is calculated as the difference between m^2_j and m^2_k. The probability of flavor transition is a periodic function of the distance L between the source and the detector and is influenced by the mass-squared differences and the neutrino energy.

In most scenarios, neutrino oscillations can be approximated by two-flavor mixing due to the suppression of three-flavor mixing effects by the small value of θ_{13} and the large hierarchy between the two mass-squared splittings, where $\Delta m^2_{21} \ll \Delta m^2_{32}$. As a result, the problem is often simplified to two-flavor oscillations. The transition probability exhibits an oscillatory behavior, hence the name. If $L \gg L_{\text{osc}}$, the oscillating phase completes many cycles before detection and is averaged to 1/2., *Neutrino Oscillations*.

In the simplest case of two-flavor mixing, the mixing matrix depends on just one mixing angle, and there is only one relevant mass-squared difference. The probability[†] that a neutrino ν_α with energy E_ν oscillates into a neutrino ν_β after traveling a distance L (the so-called *transition probability*) is given by:

$$P(\nu_\alpha \to \nu_\beta) = \sin^2(2\theta)\sin^2\left(\frac{\Delta m^2 L}{4E_\nu}\right), \quad \alpha \neq \beta. \tag{1.7}$$

As opposed to the case where the probability that a neutrino ν_α with energy E_ν after traveling a distance L is still measured in state of ν_α (the so-called *survival probability*) is given by:

$$P(\nu_\alpha \to \nu_\alpha) = 1 - \sin^2(2\theta)\sin^2\left(\frac{\Delta m^2 L}{4E_\nu}\right), \quad \alpha = \beta. \tag{1.8}$$

The transition probability derived in Equation 1.7 has a period with the oscillation length (L_{osc}) determined by the neutrino energy (E_ν) and mass difference (Δm^2) as,

$$L_{\text{osc}} = \frac{4\pi E_\nu}{\Delta m^2} \tag{1.6}$$

and the amplitude is proportional to the mixing angle. From Equation 1.6 for an experiment to be sensitive to a specific value of Δm^2, it must be configured so that $E/L \approx \Delta m^2$. For example, to measure the parameters θ_{23} and Δm^2_{32}, an L/E value of approximately 500 km/GeV is required, which is typical for atmospheric neutrino studies. To probe the parameters θ_{12} and Δm^2_{12}, the appropriate L/E would be around 15,000 km/GeV, as seen in solar neutrino experiments. The distance between the neutrino sources and detector, is usually reffered to as *baseline* of the experiment

Neutrino Oscillations in Matter

The discussion so far has assumed that neutrinos travel through a vacuum. However, when neutrinos travel through matter, their interactions with the medium alter their properties. This happens because of coherent forward scattering on electrons and nucleons, which modifies the amplitude of their propagation. Initially the idea that the oscillation parameters of neutrinos are altered in matter was coined by Lincoln Wolfenstein's [15, 16]. In 1985, Stanislav Mikheyev and Alexei Smirnov predicted that a gradual decrease in the density of matter can resonantly enhance neutrino mixing [17].

In the presence of matter, the Hamiltonian of the system changes by experiencing an *Effective Potential* (V_{eff}). As a result, the mass eigenstates and eigenvalues of this effective hamiltonian changes, meaning that neutrinos in matter now have a different effective mass than they did in a vacuum. Since neutrino oscillations depend on the squared mass difference of the neutrinos, neutrino oscillations experience different dynamics than they did in a vacuum. This theory formed basis to solve the solar neutrino puzzle, where observed deficit of neutrino fluxes could only be explained by not only neutrino oscillations but also the matter

[15]: Wolfenstein (1978), *Neutrino oscillations in matter*
[16]: Wolfenstein (1979), *Neutrino oscillations and stellar collapse*
[17]: Mikheyev et al. (1985), *Resonance Amplification of Oscillations in Matter and Spectroscopy of Solar Neutrinos*

[†] The probability is the same for neutrinos and antineutrinos.

effects that the produced neutrinos in the sun core goes through while reaching the surface, and later crossing the threshold of higher matter density to vacuum [18, 19].

[18]: Bethe (1986), *Possible Explanation of the Solar-Neutrino Puzzle*
[19]: Rosen et al. (1986), *Mikheyev-Smirnov-Wolfenstein enhancement of oscillations as a possible solution to the solar-neutrino problem*

1.1.2 Interactions

In the Standard Model, neutrinos only interact through the weak interaction, which is mediated by the exchange of the $W^{\pm}$ and Z^0 bosons. These bosons have masses of $M_{W^{\pm}} = 80$ GeV and $M_{Z^0} = 91$ GeV [20]. The massiveness of these bosons contribute to the weakness of the interaction in normal conditions. Processes involving the W-boson are referred to as charged-current (CC) processes, while those involving the Z-boson are called neutral-current (NC) processes Neutrinos interact with charged leptons ($e^{\pm}$, $\mu^{\pm}$, $\tau^{\pm}$) through scattering processes and are produced in the decays of unstable charged leptons such as $\mu^{\pm}$ and $\tau^{\pm}$. They also interact with quarks, both in bound states (e.g., neutrons, protons, pions) through neutrino-nucleon scattering, and as individual quarks (partons) through deep inelastic scattering

[20]: Navas et al. (2024), *Review of Particle Physics*

This section will cover the general properties of neutrino interactions, focusing on their cross-sections across various energy scales. Later subsections will explore high-energy interaction processes, which are important for understanding neutrino behavior in extreme environments and are relevant to the analysis presented in this thesis.

Interaction Cross-Sections

Neutrino interactions can exhibit a wide range of behaviors [21] depending on the energy at which they occur and whether the interaction involves a neutrino or an antineutrino, as shown in Figure 1.1.

[21]: Formaggio et al. (2012), *From eV to EeV: Neutrino Cross Sections Across Energy Scales*

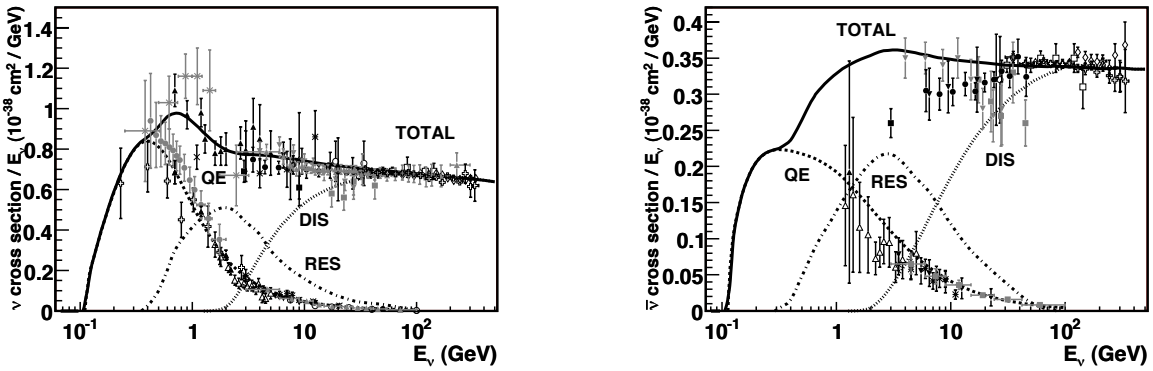

Figure 1.1: Total cross-sections for neutrinos (left) and antineutrinos (right) per nucleon in charged-current interactions (for an isoscalar target) divided by neutrino energy as a function of neutrino energy. Figure taken from [21]

At low energies, typically up to around 1 MeV, neutrino interactions are dominated by scattering off leptons and nuclei, both in charged and neutral forms. Two notable processes in this energy range are **coherent scattering** and **Neutrino Capture on Radioactive Nuclei**. These low-energy interactions can be described through electroweak theory, where the neutrino engages in two-body scattering processes. As the neutrino energy increases, it becomes possible to probe the target nucleus at

Inverse Beta Decay (IBD)

In IBD, $\bar{\nu_e}$ interacts with a proton, producing a e^+ and a neutron. The $\bar{\nu_e}$ must have a minimum kinetic energy of 1.806 MeV to initiate the reaction. This is due to the mass difference between the reactants and products. The positron receives most of the antineutrino's energy due to its smaller mass compared to the neutron.

$$\bar{\nu_e} + p \rightarrow e^+ + n \qquad (1.9)$$

progressively smaller length scales. While coherent scattering treats the nucleus as a unified structure, higher-energy neutrinos can resolve individual nucleons. One significant low-energy process is the Inverse Beta Decay (IBD). This process has been extensively studied in several experiments such as KamLAND [22] and Daya Bay [23], which measures neutrino oscillations using anti-neutrinos produced in fission nuclear reactors, typically probing energies up to around 10 MeV.

[22]: Gando et al. (2011), *Constraints on θ_{13} from A Three-Flavor Oscillation Analysis of Reactor Antineutrinos at KamLAND*

[23]: An et al. (2017), *Measurement of electron antineutrino oscillation based on 1230 days of operation of the Daya Bay experiment*

As the energy increases to the GeV range, neutrinos primarily interact through **quasi-elastic scattering** and **resonance production**. In quasi-elastic scattering, neutrinos interact with nucleons, producing charged leptons without breaking apart the nucleon. At slightly higher energies, resonance production becomes a crucial interaction mode. In this case, neutrinos excite the target nucleon into resonance states, such as Δ or N^*, which subsequently decay into various final states, yielding combinations of nucleons and mesons. The energy range of around 10 GeV is often called *the transition region* because it separates quasi-elastic scattering, where the target is a nucleon, from **the deep inelastic scattering (DIS)**, where the target is a quark (or *parton*) within the nucleon. As shown in Figure 1.1, above this transition region (> 100 GeV), the total cross-section exhibits an almost linear relationship with neutrino energy and DIS becomes the dominant process of all neutrino interactions. This scaling behavior, as predicted by the quark-parton model [24], assumes point-like scattering off quarks. However, these assumptions are not valid at lower neutrino energies, where lower momentum transfers have a greater impact on the interaction dynamics [21]. Since this energy range is critical for high-energy neutrino interactions in IceCube, especially for the analysis presented in this thesis, only DIS (and other relavnt processes at this energy, see Section 3) process shall be discussed in more detail.

[24]: Feynman (1969), *Very High-Energy Collisions of Hadrons*

[21]: Formaggio et al. (2012), *From eV to EeV: Neutrino Cross Sections Across Energy Scales*

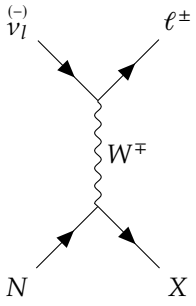

Figure 1.2: Feynman diagram of Neutrino-Nucleon DIS via CC interaction.

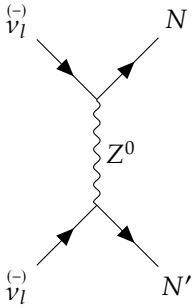

Figure 1.3: Feynman diagram of Neutrino-Nucleon DIS via NC interaction.

Neutrino-Nucleon Deep Inelastic Scattering

In Deep Inelastic Scattering (DIS), neutrinos interact with quarks inside nucleons, breaking them apart and producing a cascade of particles. In this high-energy regime, the neutrino can be seen as scattering off individual partons, but a scattered parton cannot remain free for long. It quickly creates a jet of hadrons through pair production, a process known as hadronization or fragmentation. Both charged-current (CC) and neutral-current (NC) interactions can occur this way, resulting in either an outgoing charged lepton or neutrino. Feynman diagrams of CC and NC interactions for neutrinos are shown in Figure 1.2 and Figure 1.3 respectively, with their corresponding reactions in Equation 1.11 and Equation 1.12. The most general form of the differential neutrino-nucleon cross section for a CC interaction, involving an incoming neutrino with initial four momentum k_1, scattering with a target nucleon with four-momentum p, resulting in an outgoing lepton with four-momentum k_2, and a virtual gauge boson with four-momentum transfer q=$k_1 - k_2$, can be expressed as:

$$\frac{d^2\sigma}{dx,dy} = \frac{G_F^2 m_N E_\nu}{\pi}\left(\frac{{M_W^2}^2}{Q^2 + {M_W^2}^2}\right)^2 \left[q(x,Q^2) + (1-y)^2\bar{q}(x,Q^2)\right] \quad (1.10)$$

where, G_F represents the Fermi constant, m_N is the nucleon mass, E_ν is the energy of the incoming neutrino, and M_W represents the W-boson mass. The invariant momentum transfer of the scattering process is $Q^2 = -q^2$. **The Bjorken scaling variable**,

$$x = \frac{Q^2}{p.q} \tag{1.13}$$

represents the fraction of the nucleon's momentum carried by the scattered quark, while **the inelasticity variable**,

$$y = \frac{p.q}{p.k_1} = \frac{E_{hadron}}{E_\nu} \tag{1.14}$$

measures the amount of energy transferred to the hadronic system X. The parton distribution functions (PDFs), $q(x, Q^2)$ and $\bar{q}(x, Q^2)$, represent the probability density of a quark or antiquark, respectively, to have a momentum fraction x of the nucleon at the energy scale Q^2 of the interaction.

Charged Current Interaction
(see feynman diagram Figure 1.2)

$$\overset{(-)}{\nu}_l + N \rightarrow \ell^\pm + X \tag{1.11}$$

Neutral Current Interaction
(see feynman diagram Figure 1.3)

$$\overset{(-)}{\nu}_l + N \rightarrow \overset{(-)}{\nu}_l + X \tag{1.12}$$

Here, N is a nucleon, $\overset{(-)}{\nu}_l$ is the $\nu/\bar{\nu}$ of flavour l and X is hadronic particle shower.

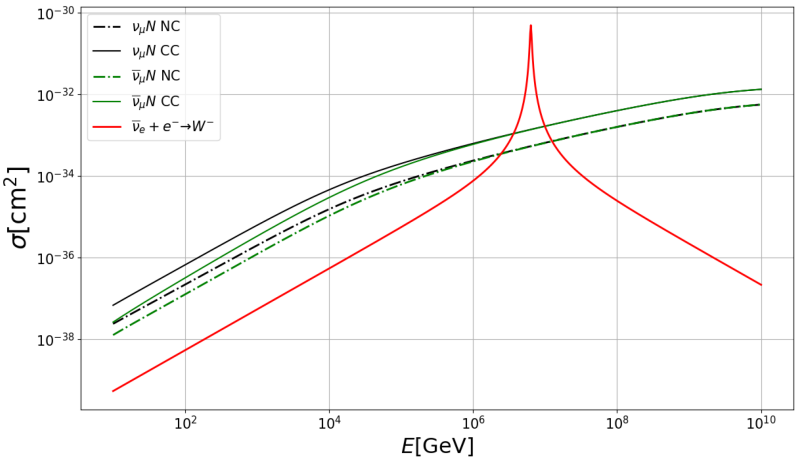

Figure 1.4: The deep inelastic scattering cross-sections for neutrino and antineutrinos are shown for both CC and NC interactions on an isoscalar target. Glashow resonance peak of $\bar{\nu_e}$ interacting with e is also visible at 6.3 PeV. Figure taken from [25]

A key feature of all structure functions is that they become nearly independent of Q^2 in the limit $Q^2 \rightarrow \infty$, meaning cross-section starts to scale linearly with neutrino energy E_ν for up-to $\sim$ 1 PeV as shown in Figure 1.4. This property, known as Bjorken scaling, was crucial in developing the parton model for deep inelastic scattering [26]. The Figure 1.4 illustrates the contributions of CC and NC interactions for both neutrinos and antineutrinos separately. It is evident that the CC cross-section is generally larger than the NC cross-section due to the stronger coupling of the W-boson compared to the Z-boson. At higher energies (> few PeVs), the propagation term from the interaction vertex is no longer dominated by the W-Z boson mass. As a result, the cross-section no longer grows linearly with neutrino energy. Moreover, the $(1-y)^2$ (see second term in bracket of Equation 1.10) suppression that typically allows distinction between neutrino and anti-neutrino interactions is much less pronounced, making the two cross-sections nearly identical [27].

[26]: Bjorken (1969), *Asymptotic Sum Rules at Infinite Momentum*

[27]: Gandhi et al. (1998), *Neutrino interactions at ultrahigh energies*

The calculation of neutrino DIS in the energy range of interest for IceCube has been carried out by Cooper-Sarkar, Mertsch, and Sarkar (CSMS) in 2011

and is the standard that will be used throughout this work to produce neutrino simulation (see Section 4.1) and also to include inelasticity parameter in the forward folding fit (see Section 5.2.1) [28]. However, updated cross-section calculations now exists, that takes into account final state radiations (FSR) [29] and uses updated parton distribution functions [30]. In particular, corrections in visible energy of Glashow events due to FSR were taken into account by introducing a correction in simulation event weight (see Section 4.4.3 for details). In the last decade, several studies have used different event samples at higher energies to measure the total‡ DIS cross-section in the multi-TeV energy range at IceCube [31, 32].

[28]: Cooper-Sarkar et al. (2011), *The high energy neutrino cross-section in the Standard Model and its uncertainty*

[31]: Aartsen et al. (2017), *Measurement of the multi-TeV neutrino cross section with IceCube using Earth absorption*

[32]: Abbasi et al. (2021), *Measurement of the high-energy all-flavor neutrino-nucleon cross section with IceCube*

Glashow Resonance

Neutrinos typically interact with atomic electrons in a detector medium less frequently than with nucleons due to the smaller mass of the electron [21]. However, an exception occurs during the resonant enhancement of the $\bar{\nu}_e e^-$ scattering cross- section, known as **the Glashow resonance**. This happens when the center-of-mass energy matches the mass of the W-boson. The resonance occurs at an antineutrino energy of $E_{\bar{\nu}} = \frac{M_W^2}{2m_e} \approx 6.3$ PeV, where m_e is the electron mass (see Figure 1.4). Produced W boson, deacays into hadrons/lepton creating a particle shower at around 6 PeV energy. Sheldon Glashow first proposed this phenomenon in 1960 as a method to detect the W-boson [33]. Due to experimental limitations, such high-energy events were not observed for many years. However, the IceCube Neutrino Observatory recently reported detecting a Glashow resonance event, providing the first confirmation of this process [34].

[21]: Formaggio et al. (2012), *From eV to EeV: Neutrino Cross Sections Across Energy Scales*

[33]: Glashow (1960), *Resonant Scattering of Antineutrinos*

[34]: Aartsen et al. (2021), *Detection of a particle shower at the Glashow resonance with IceCube*

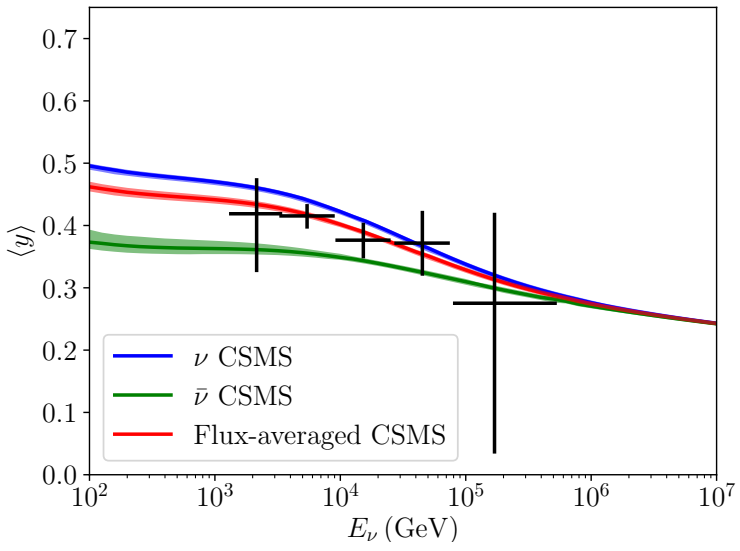

Figure 1.5: The measured mean inelasticity, with error bars indicating 68% confidence intervals. Predictions from the CSMS model are indicated in blue for ν and green for $\bar{\nu}$, with theoretical uncertainties shown by the colored bands, along with atmospheric flux-averaged inelasticity in red. Figure taken from [35].

Inelasticty

Inelasticity, denoted by y as described in Equation 1.14, represents the fraction of the incoming neutrino's energy that is transferred to the

‡ total cross-sections are inclusive of CC and NC interactions.

hadronic system during deep inelastic scattering (DIS). In neutrino-nucleon DIS, a higher inelasticity corresponds to a larger energy transfer, leading to greater energy deposition in the detector through hadronic showers. Inelasticity can be determined from the kinematics of both the outgoing lepton and the hadronic system. Such a technique was expxloited in an IceCube analysis, to measure inelasticity in TeV range, by using ν_μ-CC events where both interaction vertex (hadronic cascade) and outgoing lepton (*muon track* [2]) are within the detector [35]. The distinction in inelasticity distribution between ν and $\bar{\nu}$ (see Figure 1.5) allows for differentiation between neutrinos and antineutrinos in an event sample. Understanding such an energy dependent inelasticity distribution is crucial for analyzing high-energy neutrino interactions, such as those explored in this thesis, where both hadronic and leptonic energy signatures are used to reconstruct neutrino properties.

2: depending on energy, entire track may or may not be contained within the detector volume, as muon usually deposits some energy along its path and can travel larger distance, possibly leaving the detector, see Section3.3.1 for details

[35]: Aartsen et al. (2019), *Measurements using the inelasticity distribution of multi-TeV neutrino interactions in IceCube*

1.2 Beyond Standard Model Neutrinos

While the minimum extension used in 1.1.1 provides a framework for describing neutrino oscillations, it also predicts the existence of right-handed neutrinos (or left-handed anti-neutrinos) that do not participate in weak interactions. These non-interacting neutrinos are known as ***sterile neutrinos***. Unlike the three active flavors, sterile neutrinos do not contribute to weak interaction processes like Z^0 boson decay. Experimental measurements of the Z^0 decay width constrain the number of light, active neutrino species (those lighter than the Z^0 boson) to 3 [11].

[11]: Schael et al. (2006), *Precision electroweak measurements on the Z resonance*

Although the three-flavor model is consistent with many observations, anomalies have been observed in several experiments. Radiochemical neutrino experiments [36], as well as experiments using neutrinos from particle accelerators [37, 38] and anti-neutrinos from nuclear reactors [39], have reported discrepancies that could be explained by the existence of sterile neutrinos. The simplest theoretical extension to account for these anomalies is the so-called 3+1 model, where one additional sterile neutrino is added to the three active neutrinos. In this model, the PMNS mixing matrix (which describes the mixing between neutrino flavors) is expanded from a 3×3 matrix to a 4×4 matrix [40]. This expanded matrix introduces three new mixing angles (θ_{14}, θ_{24}, θ_{34}) and additional CP-violating phases. These additional parameters allow for the mixing of sterile neutrinos with the active ones, potentially explaining the observed experimental anomalies, though further investigation is required to confirm their existence.

[36]: Elliott et al. (2024), *The gallium anomaly*

[37]: Aguilar et al. (2001), *Evidence for neutrino oscillations from the observation of $\bar{\nu}_e$ appearance in a $\bar{\nu}_\mu$ beam*

[38]: Aguilar-Arevalo et al. (2013), *Improved Search for $\bar{\nu}_\mu \to \bar{\nu}_e$ Oscillations in the MiniBooNE Experiment*

[39]: Mention et al. (2011), *The Reactor Antineutrino Anomaly*

[40]: Abazajian et al. (2012), *Light Sterile Neutrinos: A White Paper*

Cosmological evidence also provides hints for the existence of sterile neutrinos [41]. The presence of sterile neutrinos could have observable consequences on the evolution of the early universe and on large-scale structure formation. Observations of the cosmic microwave background (CMB) and precise measurements by missions such as WMAP indicate that the number of relativistic species during the early universe, typically expressed as the effective number of neutrino species N_{eff}, is slightly higher than the expected value of 3 for the three active neutrinos [42]. This could suggest the presence of additional light particles, such as sterile neutrinos, that contributed to the radiation density in the early universe. Although, another measurement by planck survey is in close

[41]: Abazajian (2017), *Sterile neutrinos in cosmology*

[42]: Komatsu et al. (2011), *SEVEN-YEARWILKINSON MICROWAVE ANISOTROPY PROBE(WMAP) OBSERVATIONS: COSMOLOGICAL INTERPRETATION*

agreement with $N_{\text{eff}} = 3$ [43], making the puzzle of such neutrino species even more intriguing. Moreover, sterile neutrinos could contribute to the dark matter problem [44]. While they are unlikely to account for all dark matter, keV-mass sterile neutrinos are a candidate for *warm dark matter*, a type of dark matter that could impact the formation of structure in the universe on small scales. These cosmological observations, when combined with the experimental anomalies in neutrino oscillation data, make sterile neutrinos an intriguing possibility for both particle physics and cosmology. However, further precision measurements, both in the laboratory and from astrophysical observations, are needed to confirm their existence and determine their exact role in the universe.

In addition to Sterile neutrinos, other exotic phenomena, which are not included in standard model can affect neutrino interaction cross-sections or other fundamental properties assumeed in SM. Such scenarios include interaction of neutrinos with dark matter [45], CPT violation [46] etc. A number of analysis have been made in IceCube to look for sterile neutrinos [47], other exotic neutral leptons [48] and also to look for dark matter signatures [49] have been made. Although, as it will be discussed in the next chapter, for the analysis presneted in this thesis, as none of these scenraios, when probed to measure flavour fraction of astrophysical neutrinos on earth allows for non-zero tau neutrino fraction [50], hence they are not discussed further in detail, and for the remainder of this thesis, 3 flavour of neutrinos shall be assumed.

[43]: Aghanim et al. (2020), *Planck 2018 results. VI. Cosmological parameters*

[44]: Drewes et al. (2017), *A White Paper on keV Sterile Neutrino Dark Matter*

[45]: Salas et al. (2016), *Neutrino propagation in the galactic dark matter halo*

[46]: Hooper et al. (2005), *Lorentz and CPT invariance violation in high-energy neutrinos*

[47]: Trettin (2024), *Search for eV-scale sterile neutrinos with IceCube DeepCore*

[48]: Fischer (2024), *First Search for Heavy Neutral Leptons with IceCube DeepCore*

[49]: Abbasi et al. (2023), *Search for neutrino lines from dark matter annihilation and decay with IceCube*

[50]: Rasmussen et al. (2017), *Astrophysical neutrinos flavored with beyond the Standard Model physics*

Neutrinos in High Energy Universe

2

2.1 Cosmic Rays

2.1.1 Sources

2.1.2 Air Showers

2.2 Cosmic Neutrinos

2.2.1 Sources and Production Mechanisms

2.2.2 Diffuse Fluxes

2.2.3 Flavour Composition

Neutrinos in IceCube 3

The theoretical discussions from the previous chapters showed how neutrinos are essential for comprehending the origin of cosmic rays, as they serve as clear evidence of particle acceleration and hadronic interactions. However, detecting astrophysical neutrinos is highly challenging due to their small interaction cross-sections and the low fluxes expected from astrophysical objects at Earth. In short, a large detection volume is necessary. In this chapter, the entire process of neutrino detection will be described from the secondary particles produced in neutrino interactions to the propagation of their Cherenkov light in ice to the recording of this light with IceCube's optical sensors.

3.1 IceCube Neutrino Observatory

As described in 1.1.2,the detection of high-energy neutrinos requires a large detector due to their small interaction cross-section. When these neutrinos interact, the secondaries produce Cherenkov photons (see 3.3.2), therefore, the detector must be transparent to these photons. Such a large detector volume can be acquired by using natural resources such as large bodies of water or ice; by deploying photosensors underneath to create a sufficiently sized detector.

This concept was first introduced in 1960 [51]. The groundwork for implementing such a detector began with water-based experiments like DUMAND [52], which was planned to be deployed in the sea near the main island of Hawaii and another detector with a similar design Lake Baikal [53]. First ever large-scale neutrino telescope built was predecessor of IceCube experiment called AMANDA [54] at the geographic South Pole. A few hundred optical modules were dropped under the ice sheet of this dry continent between the depth of 1.5 to 2 km. Needless to say, the IceCube detector, the largest neutrino telescope in the world today, benefitted greatly in terms of design and performance from all the research and development work that was done with AMANDA. There also exists a large volume water-based neutrino telescope in the Northern Hemisphere called ANTARES[55], and its successor KM3NeT[56], located in the Mediterranean Sea.

The following subsections will discuss various detector and hardware components of the IceCube detector. Additionally, the last section will cover the optical properties of the South Pole ice, as these properties strongly affect the analysis observable and therefore influence the flavor measurements presented in this thesis.

[51]: Markov (1960), *On high energy neutrino physics*

[52]: Babson et al. (1990), *Cosmic-ray muons in the deep ocean*

[53]: Belolaptikov et al. (1997), *The Baikal underwater neutrino telescope: Design, performance, and first results*

[54]: Andres et al. (2000), *The AMANDA neutrino telescope: principle of operation and first results*

[55]: Ageron et al. (2011), *ANTARES: The first undersea neutrino telescope*

[56]: Margiotta (2014), *The KM3NeT deep-sea neutrino telescope*

3.1.1 Detector

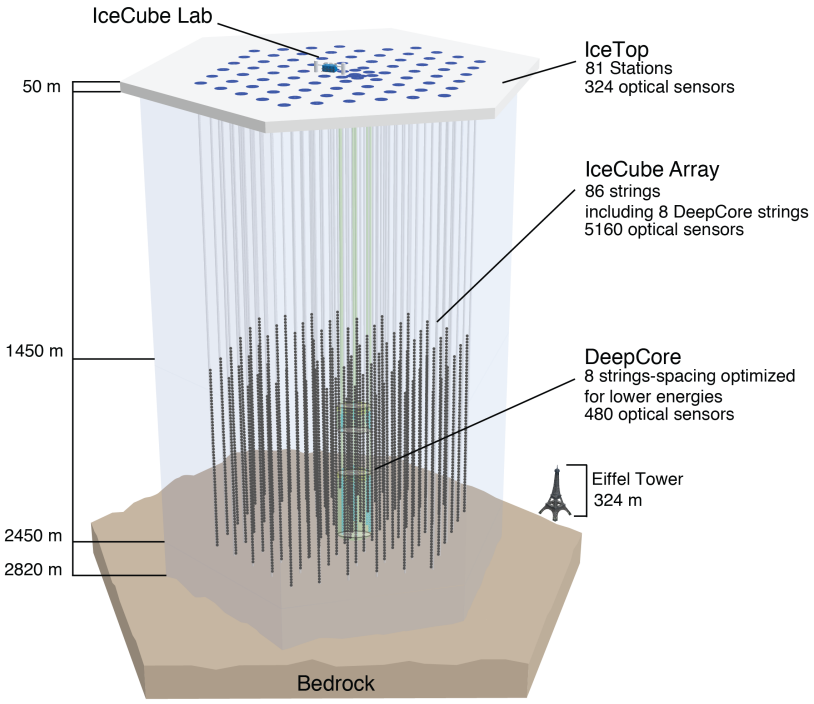

Figure 3.1: A schematic overview of the IceCube detector and its components [57]

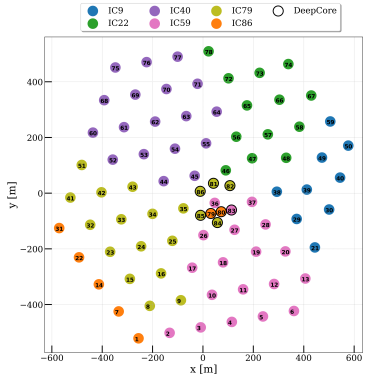

Figure 3.2: Top view of the location of each *in-ice* strings of IceCube. Colour represents set of strings deployed in each seasons as described in Table 3.1. Note: IceTop Stations are not shown here.

[57]: Aartsen et al. (2017), *The IceCube Neutrino Observatory: instrumentation and online systems*

***string* in IceCube**
An arrangement of DOMs attached on a twisted copper wire cable makes the so-called *string* in IceCube.

[58]: Abbasi et al. (2012), *The design and performance of IceCube DeepCore*

[59]: Aartsen et al. (2019), *Measurement of atmospheric tau neutrino appearance with IceCube DeepCore*

[60]: Abbasi et al. (2022), *Search for GeV-scale dark matter annihilation in the Sun with IceCube DeepCore*

[61]: Abbasi et al. (2013), *IceTop: The surface component of IceCube*

The IceCube Neutrino Observatory is located at Amundsen-Scott South Pole Station at the geographic South Pole. It comprises a cubic kilometer of instrumented ice, equipped with 5,160 digital optical modules reffered as *DOMs* from here-on (see 3.1.2), buried deep in the ice and 81 IceTop Stations on the surface of the ice, making itself the largest Neutrino Observatory in the world [57]. A schematic of the detector layout is shown in Figure 3.1. Four main components of the detector are *in-ice array,DeepCore (inner extension of in-ice array),IceTop and IceCube Lab.*

The Main *in-ice* array consists of 78 strings, each consisting of 60 DOMs, spaced vertically at a distance of 17 m between the depth of 1450 m to 2450 m under the ice sheet of Antarctica. Horizontal spacing between each of these strings is 125 m.

DeepCore comprises inner 8 strings (see Figure 3.2) of the main*in-ice* array, placed more closely together with horizontal string distance of 70 m and vertical DOM distance of 7 m [58] between 1750 m to 2450 m depth. There's a region between depth of 1850 m to 2100 m, with no DOMs attached to the string as this region is the so-called *dust layer* (see section 3.2), where optical scattering and absorprion is quite high and thus is not efficient to make reliable physics measurements. The Photomultipliers used in DOMs attached on these 7 strings also have higher Quantum Efficiency, which reduces the energy threshold to 10 GeV. Although, IceCube's main goal is to detect astrophysical neutrinos, current topics of research spans much broader range (e.g fundamental properties of the neutrinos, such as oscillations [59], Physics beyond Standard Model searches such as Dark Matter [60] etc).

IceTop is the surface detector array of the IceCube detector, primarily designed to detect Cosmic-ray airshowers and to be used as a veto layer for downgoing muons produced in these airshowers [61]. It

Season	Configuration	Strings	IceTop Stations
2004-05	IC1	1	4
2005-06	IC9	9	16
2006-07	IC22	22	26
2007-08	IC40	40	40
2008-09	IC59	59	59
2009-10	IC79	79	73
2010-11	IC86	86	81

Table 3.1: IceCube detector components deployed in each season (cumulative). Each configuration is represented as *ICXX* where *IC* stands for IceCube and *XX* stands for number of total *in-ice* strings at the end of that season

consists of 81 *stations* each having 2 tanks filled with clear ice (162 tanks in total). Each of these 162 tanks have 2 DOMs, similar to the ones deployed in *in-ice* array, which makes it easier for both arrays to have a similar trigger and data acquistion system.

***IceCube Lab*(ICL)** serves as the central operations' hub for the experiment, providing a crucial support for data acquisition and filtering. All the string cables connected to the aforementioned detcetor components are routed up to the ICL, from where triggered data is sent back to the northern hemispher via a satellite. Various other operations such as mainting the detector operations etc are also maintained from this building.

For the work presented in this thesis, neither *deepcore* nor *IceTop* data is used.

The construction of the detector started taking place in 2005 and lasted for 7 Antarctic summer seasons till 2011 December. In each season, parts of the current day Hexagonal detector were deployed, as shown in Figure 3.2 and numbers detailed in Table 3.1. A hot water drill was used to unfreeze the ice upto 2.5 km depth and 60 cm diameter into which these strings were then deployed (see Figure 3.3). The geometry of the detcetor, i.e The *xy*-coordinates of the string were calculated from the drill tower position, surveyed during the deployment. Assuming the string was vertical, these coordinates were applied at all depths, with deviations of less than 1 m (later validated using the flasher data, see 3.1.3). Depths of the lowest DOM were determined from pressure readings, corrected for water compressibility and ambient air pressure, with vertical DOM spacings measured via laser ranger. All depths were converted to z-coordinates in the IceCube coordinate system .

IceCube coordinates system

The IceCube coordinate system's origin is at 46500'E, 52200'N, 883.9 m elevation, which is quite close to centre of the *in-ice* array. The y-axis points Grid North (toward Greenwich, UK), the x-axis points Grid East (90 degrees clockwise from North), and the z-axis points "up", forming a right-handed coordinate system.

Maybe draw a small schematic of coordinate system here next to the side note?

3.1.2 The Digital Optical Module (DOM)

The Digital Optical Module (DOM) is a crucial component of the IceCube Neutrino Observatory, functioning as the heart of the detector. Each DOM is responsible for collecting the faint light signals produced by neutrino interactions in the Antarctic ice, amplifying these signals, and transmitting the data to the IceCube Lab [57]. From there, the data is relayed to the Northern Hemisphere via a satellite for further analysis.

Inside each DOM, a 10-inch Photo Multiplier Tube (PMT) is positioned at the bottom, accompanied by essential circuitry for power conversion, data acquisition, calibration, control, and data transfer. Individual components of a DOM are as shown in Figure 3.4, functions of each of which is explained briefly below.

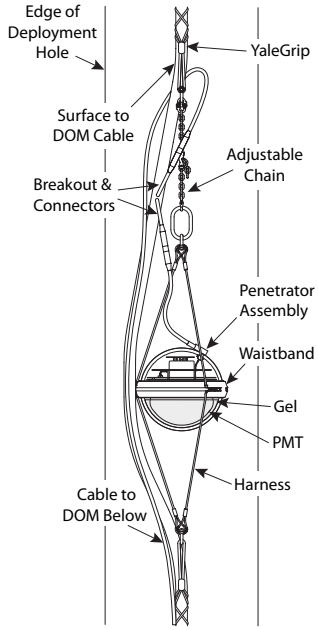

Figure 3.3: A schematic of DOM Cable-Assembly being deployed in a water hole, created by hot water drill [57].

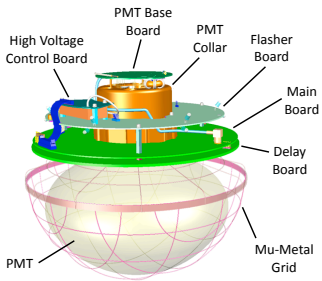

Figure 3.4: A schematic of the DOM, showing its main components [57].

Glass Vessel Properties : The glass vessel of the DOM is engineered to withstand the extreme pressures found in the deep Antarctic ice. This includes the constant long-term pressure of about 250 bar and the temporary pressure spikes of up to 690 bar experienced during the refreezing process after deployment using a hot water drill. The vessel is composed of two 0.5-inch thick hollow glass hemispheres, which are joined together with optical glue. This design not only provides a robust and hermetic seal to protect the internal electronics but also maintains the optical clarity necessary for the PMT to function effectively. The glass material is chosen for its strength, transparency, and resistance to the harsh conditions in the ice.

PMT : The PMT within the DOM is a 10-inch diameter tube that utilizes a box-and-line dynode chain with 10 stages to amplify the faint light signals detected in the ice. The PMTs used in standard in-ice DOMs have a quantum efficiency peaking at 25% whereas, DeepCore DOMs, designed to detect lower energy neutrinos, feature PMTs with a higher peak quantum efficiency of 34% near the 390 nm wavelength. These PMTs are operated at a gain of 10^7.

Gel : A high strength, silicon gel is used between the photocathode area and the glass vessel to provide optical coupling and strong mechanical support to the DOM system. This gel has a high optical clarity, with 97% transmission at 400 nm. It shows no signs of deterioration even after a decade, ensuring reliable performance.

Magnetic Shield : The ambient magnetic field at the South Pole, measuring around 550 milligauss (mG), angled 17 degrees from vertical, can significantly affect the performance of the PMT. This includes reducing collection efficiency by 5-10% and causing gain variations of up to 20%, depending on the PMT's azimuthal orientation. To mitigate these effects, a mu-metal cage is installed around the PMT bulb, extending up to its neck. This cage is constructed from a mesh of 1 mm diameter wires with a spacing of 66 mm. Although this mesh blocks about 4% of the incident light, it substantially reduces the adverse impacts of the magnetic field, ensuring more consistent and reliable performance of the PMT.

PMT Base and High Voltage Boards : The high voltage board includes a Digital to Analog Converter (DAC) and an Analog to Digital Converter (ADC) for precise control and monitoring of the voltages supplied to the PMT. The high voltage generator on this board provides the necessary power, which is then regulated and distributed by the voltage divider circuits on the PMT base board. These circuits are specifically designed for low power consumption, ensuring efficient and stable operation of the PMT.

Main Board : The main board serves as the central processing unit (CPU) of the DOM, managing and coordinating all other electronic components. It digitizes the waveforms detected by the PMT, providing a digital representation of the light signals for further analysis. The main board also temporarily stores data, calibrates the internal clock, and exchanges local coincidence information with neighboring DOMs (see 3.1.3). It communicates directly with the Data Acquisition (DAQ) system, ensuring the seamless transfer of data to the IceCube Lab. Additionally, the main board hosts an adjustable low-intensity optical source, which is used to calibrate

the PMT's gain and timing, ensuring consistent and accurate performance.

Flasher Board : Flasher board contains 12 LEDs each having specified output wavelength of 405 ± 5nm, which generates lights *in situ* to make various caliberation related measurements. In addition, this board can verify timing responses (useful for many, including analysis presented in this thesis, reconstruction processes). Additionaly, to measure *the optical properties* of the South Pole Ice (see section 3.2) and locations of the DOMs in ice.

3.1.3 Trigger and Data Acquisition

Ever Since the initial deployment of the first string, the detector has been consistently gathering data, maintaining an average uptime of nearly 99% [62]. *The photocathode* of the PMT of a DOM, *captures* a photon which then generates *photoelectrons* which are accelerated through the series of 10 dynodes to generate measurable *photocurrent*. This current is integrated over a time to obtain collected charge in units of *photoelectrons or PEs*, through which *photovoltage* is produced at the mainboard, over time, known as *waveform*. These waveforms are then digitized to acquire and relay the data to the Northern Hemisphere.

[62]: Abbasi et al. (2009), *The IceCube data acquisition system: Signal capture, digitization, and timestamping*

Depending on how many photons hit the PMT, these waveforms can have different amplitudes ranging from 1mV upto the linearity limit of the PMT (2 V) in time range of 12-1500 ns. The In Order to access this rather broad dynamic range, the digitiser used, Analog Transient Waveform Digitiser (ATWD) have three channels to amplify the waveform by factor of 0.25, 2 and 16. Moreover, 2 sets of ATWD are used that can operate alternatively in order to reduce the deadtime. ATWD can digitize voltage withinn duration of 427 ns, a window sufficient to reconstruct light produced within 10s of m around a given DOM. Naturally, some photons produced in energetic interactions may travel larger distances, producing faint but detectable waveforms. To amplify and digitize these waveforms, a fast Analog to Digital Converter (fADC) is also used, together ATWD+fADC is reffered as a *DOMLaunch*.

The aforementioned digitization only happens if the voltage threshold of the onboard discriminator is met, which is kept at voltage equivalent to a PE of 0.25, or in other words, a DOM is *hit*. If at least two neighbouring DOMs, on the same string produces individual *hits* within 1 μs called *Hard Local Coincidence(HLC)*, the full *DOMLaunch* is transmitted to the surface. Otherwise, only the timestamp and minimal amplitude/charge information is sent known as *Soft Local Coincidence(SLC)*. The HLC condition helps reduce false triggers from PMT dark noise, which is independent across DOMs. *The Data Acquisition System (DAQ)* processes further uses these HLC hits to look for temporal coincidences. Most commonly used trigger in IceCube is the so-called *The Single Multiplicity Trigger (SMT-8)*, that requires eight or more HLC hits within 5 μs timewindow. If and when SMT8 trigger conditions are met, all launches (HLC and SLC) are combined into what is called an *event*.

Various algorithms are used to make an estimate of event properties such as direction, deposited energy, morphology etc. The South Pole has limited computational resources, so only simple first guess algorithms

can be used there called *online filters*. Processed data is transmitted to the Northern Hemisphere. After this, more sophisticated reconstruction algorithms are applied to reduce and tailor the data as per Physics analysis goal.

cite simulation/reco chapter here

3.2 Optical Properties of the South Pole ice

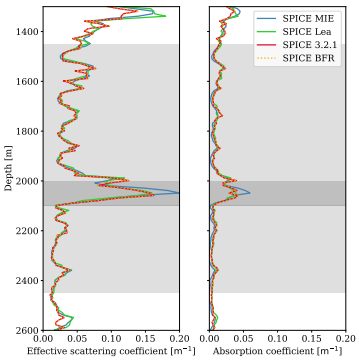

Figure 3.5: Values of effective scattering (left) and absorption (right) coefficents of 400nm photons in South Pole Ice as a function of depth, for four icemodels described in the text. Light grey area shows in-ice array and dark grey region shows the high absorption and scattering region called *the dust layer*.

The ice at the South Pole is a crucial part of the IceCube detector. It acts as both the detection target and the medium through which light propagates. Unlike the DOM hardware, which has been extensively studied in the laboratory, the glacial ice can only be measured in its actual environment, making it more challenging to describe. Understanding and calibrating this medium well is essential for accurate physics measurements as photons produced from particle interactions can get absorbed or scattered from their path, making the inference of the particle interaction points challanging.

In context of Neutrino Detection, The ice at the deep South Pole was initially measured using pulsed in situ light sources (LEDs) at different wavelengths, embedded in the AMANDA array below 1000 m depth[63]. Later, during the construction of IceCube, direct measurements of dust concentration in the glacial ice were obtained using a dust logger deployed into some drill holes [64]. Additionally, the LEDs on the Flasher Board of DOMs are still actively used to calibrate the detector and understand the ice properties [65].

The scattering length (l_s) is the average distance a photon will travel before scattering off of its orignal directory. In practice, only the effective scattering length ($l_{eff} = \frac{l_s}{1-\langle\cos\theta\rangle}$) can be measured, where $\langle\cos\theta\rangle$ is the average deflection angle at each scatter. **The absorption length (l_a)** is the distance after which a photon's survival probability decreases to 1/e, indicating how far the information from an event can travel. In the case of absorption, the photon is lost, while for scattering, its direction changes, affecting both the energy and direction reconstruction of the event. Scattering and absorption parameters in *ice models* are averaged over 10-meter-thick layers of ice and are calculated for a wavelength of 400 nm [65]. Light scattering below a depth of about ~1300 m is mainly due to residual air bubbles. As depth increases, dust becomes the main source of scattering, with concentration varying due to climate and volcanic activity. At around 2000 meters, scattering and absorption significantly increase due to high dust concentration, possibly from a major volcanic eruption in the past, known in IceCube as **the dust layer** [66] (see Figure 3.5). This layer is either ommitted or treated more carefully in most analyses as information carried by photons coming and going throught this layer is difficult to traceback due to higher scattering coeeficient.

The data from the dust logger also revealed that the ice layers are not perfectly horizontal; they are tilted due to the uneven surface of the bedrock [64], the so-called **ice tilt**. Initially, the effect was symmetrically parameterized along an axis (reffered to as *the tilt axis*) that is approximately perpendicular to the glacial flow and also dependent on depth (same as the layers used to characterise absorption and scatetring lengths described before)[65]. As a result, the scattering and absorption coefficients became dependent on the full three-dimensional position in the

[63]: Ackermann et al. (2006), *Optical properties of deep glacial ice at the South Pole*

[64]: Aartsen et al. (2013), *South Pole Glacial Climate Reconstruction from Multi-Borehole Laser Particulate Stratigraphy*

[65]: Aartsen et al. (2013), *Measurement of South Pole ice transparency with the IceCube LED calibration system*

[66]: Woschnagg et al. (2000), *Age vs depth of glacial ice at South Pole*

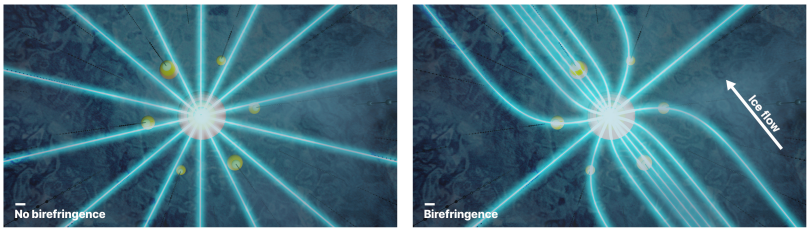

Figure 3.6: The visualisation of deflection due to birefringence. Without it (left panel), light streams out radially from an isotropic source. With this effect however (right panel), rays get deflected towards the flow axis, appearing as though photons are scattered "more" along this axis. The IceCube array around the light source can be seen as well. (Figure taken from [67])

ice rather than just the depth. A recently developed fully volumetric tilt model now includes a newly discovered tilt component along the flow [68].

[68]: Chirkin et al. (2023), *An improved mapping of ice layer undulations for the IceCube Neutrino Observatory*

Another unique property that the South Pole ice exhibits is optical **anisotropy**, a phenomenon affecting photon propagation depending on their direction relative to the "axis of anisotropy," which coincides within $\sim 1^\circ$ with the direction of the ice flow [65]. This effect was initially implemented as a modification to the scattering function, the only remaining Mie scattering parameter [69], thereby changing the scattering length [70, 71]. However, recent detailed studies suggest that this behavior results from diffusion within the polycrystalline ice microstructure, a previously unknown optical effect, now known as Birefringence [67, 72]. This effect causes the ice crystals to slowly but continuously deflect towards the normal vector of the girdle plane of the crystal orientation fabric (the ice flow axis), as can be seen in Figure 3.6.

[69]: Hahn (2004), *Light Scattering Theory*
[70]: Chirkin et al. (2013), *Evidence of optical anisotropy of the South Pole ice*
[71]: Usner (2018), *Search for Astrophysical Tau-Neutrinos in Six Years of High-Energy Starting Events in the IceCube Detector*
[67]: Abbasi et al. (2024), *In situ estimation of ice crystal properties at the South Pole using LED calibration data from the IceCube Neutrino Observatory*
[72]: Chirkin et al. (2019), *Light diffusion in birefringent polycrystals and the IceCube ice anisotropy*

In the context of the IceCube Detector, South Pole ice can be divided into two types: bulk ice and hole ice. Bulk ice is the undisturbed part of the ice, consisting of sheets that have formed over hundreds of thousands of years, properties of which are described above. **Hole ice**, on the other hand, is the refrozen column of ice that was melted during the deployment of the DOMs [73]. This effect generally affects the forward acceptance of the IceCube DOMs. If not taken care of, it can lead to errors in directional information, therby affecting measurements involving zenith angle reconstructions of the incoming neutrino. Over the years, many efforts have been made to understand various optical properties of the South Pole ice, by fitting the LED data in terms of absorption and scattering lengths of a cherenkov photon in ice, the so-called ***South Pole ICE model (SPICE model)***. These icemodels are used in both simulation and reconstruction of the events, where particles produced in neutrino interactions are propagated (see 3.3.1) based scattering and absorption lengths described by the model. While the base model for the scattering of the photons in-ice is Mie Scattering theory [69] (SPICE MIE), with more dust loggers data, evolved more complex models to include, aniostropy (SPICELea), addition of tilt (SPICELea, SPICE 3.2.1), birefringence to explain anisotropy (SPICEBfr) and the latest, SPICE FTP, which includes a 2D tilt corretion in addition to birefringence. Figure 3.5 shows absorption and scattering coefficients for different ice models at various depths in the detector. The corresponding scattering and absorption lengths are simply the inverse of the coefficients. It can be seen that the ice below the depth of ~ 1400 m is so clear that light can travel for hundreds of meters before being absorbed. However, the light diffuses quickly, making a point-like source appear nearly isotropic at a distance of around 100 m. Effect of different icemodel corrections (specifically that of anisotropy related corrections) becomes quite relevant to reconstruct tau-neutrino events in

[73]: Abbasi et al. (2021), *A calibration study of local ice and optical sensor properties in IceCube*

IceCube, which is heart of the analysis presented in this thesis.

3.3 Detection of Neutrinos in IceCube

As described in 1.1.2, regardless of the type of neutrino interaction (NC or CC), a variety of secondary particles are generated. In the case of a CC interaction, an accompanying charged lepton absorbs some energy, which can then undergo further decay or interact within the ice volume, leading to the production of more particles. Moreover, secondary particles, regardless of the interaction type, may also include hadrons, which are not always charged. This can, in turn, reduce the amount of *visible* light in the detector. In this section, propagation of these leptons and hadrons in ice shall be explained in brief, followed by Cherenkov effect, a phenomenon by which IceCube DOMs observes these photons from the neutrino interactions. Lastly, various morphologies of these interactions will be discussed in the context of IceCube and similar detectors.

3.3.1 Particle propgation in-ice

When a charged particle moves through a medium like ice, it loses energy due to interactions with the medium's particles. This energy loss is characterized by the quantity $\frac{dE}{dx}$, where dE represents the energy lost and dx the area of the medium traversed, typically measured in $\mathrm{g/cm^2}$. Four primary processes contribute to the energy loss profile of a particle in such a medium: continuous ionization losses and radiative losses due to bremsstrahlung, pair production, and photonuclear interactions. *Ionization* occurs when the particle collides with shell electrons of the atoms in the medium, causing a continuous energy loss that scales logarithmically with the particle's energy [20]. Additionally, if the particle is unstable, it may decay. In the context of IceCube, secondary leptons travel at nearly the speed of light, simplifying β to approximately 1. Thus, the decay length can be rewritten as $\lambda_{\mathrm{dec}} = \frac{E\tau}{mc}$, where E is the lepton's energy and m its mass. The decay length indicates the distance at which the lepton's survival probability drops to $\frac{1}{e} \approx 36.8\%$, following the exponential decay law $p(L) = \exp(-L/\lambda_{\mathrm{dec}})$.

[20]: Navas et al. (2024), *Review of Particle Physics*

Radiative losses, such as *bremsstrahlung*, occur when the charged particle is deflected through Coulomb scattering off a target atom, while *pair production* involves the creation of an electron-positron pair by an emitted photon. *Photonuclear interactions* occur when a photon emitted by the particle disintegrates an atomic nucleus. These radiative losses are stochastic and scale roughly linearly with the particle's energy, with the radiation length X_0 defining the distance over which the particle's energy decreases to $\frac{1}{e}$ of its initial value [20]. The overall energy loss can be expressed as,

$$-\frac{dE}{dx} = a(E) + b(E)E \tag{3.1}$$

where $a(E)$ represents ionization losses and $b(E)$ encompasses all radiative losses.

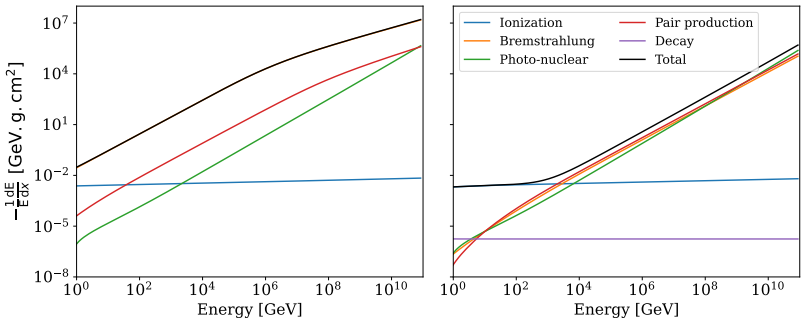

Figure 3.7: The average energy loss rate per energy, for electrons (left) and muons (right) in ice showing the contributions from ionization, bremsstrahlung, photonuclear interactions, and pair production. Note that decay is only shown for Muons as electrons are stable particles that do not decay. Figure reproduced from [75]

Leptons

To determine a neutrino's flavor, it's important to understand the energy losses of the charged lepton created in a CC-interaction. The radiation length varies depending on the lepton's mass, influencing emitted radiation and aiding in lepton identification. For leptons with $\beta\gamma \gg 1$, this ionization loss can be approximated as constant, with a value of $\langle \frac{dE}{dx} \rangle_{\text{ion}} \approx 2\,\text{MeV}/(\text{g}/\text{cm}^2)$ [74]. In ice, this corresponds to a continuous energy loss of approximately 180 MeV per meter. However, at energies exceeding *critical energy* (E_c), radiative losses become dominant, and ionization losses become negligible, as shown in the Figure 3.7 [75].

[74]: Perkins (2003), *Particle astrophysics*

[75]: Chirkin et al. (2004), *Propagating leptons through matter with Muon Monte Carlo (MMC)*

For **electrons**, we mainly consider radiative losses (mainly bremsstrahlung see Figure 3.7) as they are stable and do not decay. Photons from bremsstrahlung then create additional e^+e^- pairs which can create more photons and so on, resulting in a cascade of particles until the energies of electrons and positrons fall below the critical level. This behavior can be described by a gamma distribution, regardless of what the initiating particle is (e^+ e^-or γ) [20]. The rate of energy loss over distance can be calculated using the equation:

$$\frac{dE}{dt} = E_0 b \left(\frac{(bt)^{a-1} e^{-bt}}{\Gamma(a)} \right) \tag{3.2}$$

Where t represents the distance along the cascade in units of radiation length, and E_0 is the initial energy of the injected particle and a and b are dimensionless shower parameters. For an electromagnetic cascade induced by an electron, the parameters are $a = 2.02 + 0.63 \log(E_0/\text{GeV})$ and $b = 0.63$ (determined using `GEANT4` simulations [76]). The distance to the shower maximum, t_{max}, which is given as $t_{\text{max}} = \frac{a-1}{b}$ characterizes the size of electromagnetic cascades, indicating that they grow logarithmically in size with energy and have a characteristic size of several meters. This justifies the common approximation that light is emitted from a single point, a useful assumption for simulation and event reconstruction purposes.

[76]: Radel et al. (2013), *Calculation of the Cherenkov light yield from electromagnetic cascades in ice with Geant4*

reference reco chapter here

At very high energies (> 10 PeV), *the Landau-Pomeranchuk-Migdal (LPM) effect* becomes significant, causing suppression of bremsstrahlung and pair production cross sections [77–79]. This suppression occurs due to destructive interference between multiple scattering centers, leading to elongated and irregular shower profiles.

[77]: Landau et al. (1953), *Limits of applicability of the theory of bremsstrahlung electrons and pair production at high-energies*
[78]: Landau et al. (1953), *Electron cascade process at very high-energies*
[79]: Migdal (1956), *Bremsstrahlung and Pair Production in Condensed Media at High Energies*

Muons experience similar ionization and radiative losses as described in **??**, but due to their larger mass, the radiation length ($\text{X}_0 \sim 15\text{km}$) is

much longer than that of an electron (($X_0 \sim 36$cm)) of the same energy. This results in a higher critical energy (E_c) of 1 TeV in ice, allowing muons to penetrate more deeply than electrons (E_c = 79 MeV) [75], as can be seen in the right panel of Figure 3.7. The average energy loss rate can be approximately parameterized using 3.1, with $a = 0.00268\text{GeV cm}^2/\text{g}$ and $b = 0.47 \times 10^{-5}\,\text{cm}^2/\text{g}$ in ice [20], allowing the calculation of the average range of a 1 TeV muon, which is 2 km in ice [1].

1: If one neglects these radiative losses, due to its longer lifetime ($\tau_\mu = 2.2 \times 10^{-5}$) and small mass ($m_\mu = 105.67$), the same energy muon will travel ~ 6000km distance

The **tau** lepton has an even larger radiation length than a muon, $X_0 \sim 4754$ km, but its decay length is much shorter, $L_\tau(E_\tau = 1\,\text{TeV}) = 4.9\text{c}m$ [20]. Thus, most taus created in IceCube will decay very promptly. τ^- can decay mainly via the following three modes (with the branching rations specified next to each):

$$\begin{aligned} \tau^- &\rightarrow \nu_\tau + \text{Hadrons} \quad (64.79\%) \\ \tau^- &\rightarrow \mu^- + \bar{\nu}_\mu + \nu_\tau \quad (17.39\%) \\ \tau^- &\rightarrow e^- + \bar{\nu}_e + \nu_\tau \quad (17.82\%) \end{aligned} \tag{3.3}$$

where the most commonly produced hadrons are pions and kaons [20]. Similar decay modes are observed for τ^+ too, by keeping in mind Lepton number conservation. Since each mode produces at least one neutrino, part of the tau lepton's energy is not "visible"[2]. In addition, the large radiation length will create much less light during propagation through the ice than a muon of the same energy. As will become clear in the next chapter, a 1 TeV tau cannot be distinguished from an electron due to its short decay length and the large sensor spacing of IceCube. Taus from ν_τ charged-current interactions are polarized [80], and due to the small decay length and large radiation length, the decay products' energy spectrum gets affected. This becomes important in the analysis presented in this thesis, where one of the observables is an estimate of deposited energy in the detector.

2: Although these neutrinos can regenerate to interact or decay further, the probability of both neutrinos interacting within the 1 km^3 volume is rare

[80]: Argüelles et al. (2022), *Tau depolarization at very high energies for neutrino telescopes*

Hadrons

Hadrons are produced in all flavour NC interactions, or when a tau lepton decays (see 3.3). Hadronic cascades are more complex than electromagnetic cascades because they involve a wider variety of secondary particles and have larger uncertainties in the relevant cross-sections. Unlike electromagnetic cascades that consist solely of electrons, positrons, and photons, hadronic cascades involve numerous neutral particles that do not emit "*visible*" light in the detector, resulting in a lower light yield (see 3.3.2). Additionally, the production threshold for hadrons is higher compared to that for electrons, positrons, and photons [75]. Despite these differences, a significant portion of the cascade's total energy can still be carried by electrons, positrons, and photons, which are produced by electromagnetic sub-cascades initiated by the decay of neutral pions ($\pi^0 \rightarrow \gamma\gamma$).

[75]: Chirkin et al. (2004), *Propagating leptons through matter with Muon Monte Carlo (MMC)*

The longitudinal profile of hadronic showers can be parameterized using 3.2, although the specific values for the shower parameters are $a = 1.81 + 0.39\log(E_0/\text{GeV})$ and $b = 0.34$ (assuming cascade is induced by a charged pion). It is important to note that the electromagnetic radiation length used in these equations applies to both types of cascades; however, it does not account for the generally larger nuclear interaction length

characteristic of hadronic showers, adding another layer of complexity and resulting in greater fluctuations in the overall development of the particle cascade. This makes modeling hadronic cascades more challenging compared to their electromagnetic counterparts.

3.3.2 Cherenkov effect

When a charged particle moves through a medium at speed exceeding the phase velocity of light in that medium, it emits *Cherenkov radiation* [81], much like the shock wave generated by a supersonic jet. This radiation is emitted in a cone at an angle $\theta_C = \cos^{-1}\left(\frac{1}{\beta n}\right)$ relative to the particle's direction of travel, where n is the refractive index of the medium and $\beta = \frac{v}{c}$ represents the ratio of the particle's velocity to the speed of light in a vacuum (see Figure 3.8). In ice, with a refractive index of $n = 1.31$ at a wavelength of 400 nm, which corresponds to the peak sensitivity of IceCube's optical modules (see, 3.1.2), the emission threshold for Cherenkov radiation is $\beta_{\text{Ch}} \gtrsim 0.76$. This corresponds to a minimum energy of 0.28 MeV for electrons and 58.09 MeV for muons, both of which are below IceCube's detection threshold of around 200 GeV. For high-energy particles in IceCube, where $\beta \simeq 1$, the Cherenkov cone's opening angle is $\theta_{\text{Ch}} \simeq 40.2°$ at the peak sensitivity wavelength. The number of Cherenkov photons emitted within a waveband $d\lambda$ by a particle with charge ze within the propagation length dx is given by the Frank-Tamm formula [82]:

$$\frac{d^2N}{dxd\lambda} = \frac{2\pi\alpha z^2}{\lambda^2}\left(1 - \frac{1}{\beta^2 n(\lambda)^2}\right) \tag{3.4}$$

where, α is fine structure constant [20]. Using this formula, one can calculate that for a high-energy particle with $\beta \simeq 1$ passing through ice, approximately 250 photons/cm are emitted in the wavelength range of 300 nm to 500 nm, which is within IceCube's optimal detection range [76].

Neutrino interactions in IceCube are detected indirectly through Cherenkov radiation from secondary charged particles (leptons, hadrons and electromagnetic showers, see 3.3.1) , reffered to as *visible light* in IceCube. At energies above 1 TeV, the Cherenkov light from a muon itself becomes negligible, and detection primarily depends on light emitted by secondary particle showers along the muon's path.

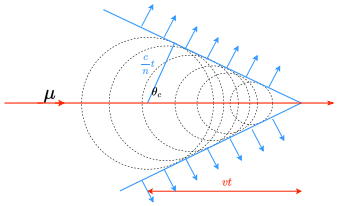

Figure 3.8: The sketch shows the Cherenkov effect for a muon traveling through a dielectric medium with a velocity $v = \beta c$ (in red). The medium has a refractive index n, and the phase velocity of light $v_{\text{phase}} = \frac{c}{n}$ (in blue). The circles in the sketch represent wavefronts with equal phase shifts and illustrate isotropic and coherent emission (blue arrows) at an angle θ_c , for $v > v_{\text{phase}}$.

[81]: Cherenkov (1937), *Visible radiation produced by electrons moving in a medium with velocities exceeding that of light*

[82]: Frank et al. (1937), *Coherent visible radiation of fast electrons passing through matter*

[20]: Navas et al. (2024), *Review of Particle Physics*

[76]: Radel et al. (2013), *Calculation of the Cherenkov light yield from electromagnetic cascades in ice with Geant4*

3.3.3 Event Signatures

The previous sections described the detector and its various components, along with the interactions and passage of neutrinos and the secondary particles they produce. In IceCube, events are visualized with the detector shown as an array of strings, with each colored sphere representing a triggered DOM. The sphere's size scales with the detected cherenkov light amount (charge accumulated), and its color indicates the arrival time. Section 1.1.2, discussed how all-flavor neutral current (NC) interactions result in the transfer of a fraction of the neutrino's energy to the nucleus, initiating a hadronic shower. On the other hand,

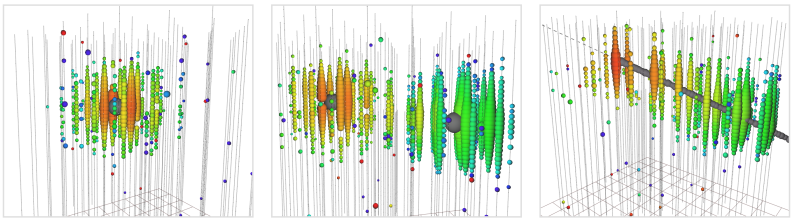

Figure 3.9: Simulated event signatures of single cascade (left), double cascade (middle), and track (right). Sizes of the spheres represent the amount of detected light, and colors show the photon arrival times. Single cascades are caused by electromagnetic and hadronic showers, double cascades by the production and decay of a tau lepton, and tracks by muons traversing the detector.

charged current (CC) interactions are accompanied by a charged lepton, whose propagation patterns were detailed in 3.3.1. The involvement of specific neutrino flavors in CC events leads to a distinct energy deposition patterns (*morphology*), which can be used to identify the neutrino flavor. Additionally, when a neutrino interaction occurs within the volume of the detector, it is classified as a *starting* event, and if the energy deposition is entirely within the detector volume, it is termed a *contained* event. Hadrons and electrons produce showers, which are known in IceCube as **cascades**. Due to the low radiation lengths of electrons and the short shower maximum caused by various secondary particles, cascades are contained within a few meters. This causes Cherenkov light emission to appear as a point-like source relative to the kilometer-scale detector. However, due to a higher scattering coefficient 3.2 the light pattern appears almost spherical for cascades see Figure 3.9, due to which, the angular information is lost (or becomes less reliable) upon reaching the DOMs, leading to a poor angular resolution. In electromagnetic cascades, most of the interaction energy is contained within the cascade, making ν_e - CC events excellent candidates for energy estimation [83]. **Tracks** are observed when highly energetic muons traverse the detector, most commonly from atmospheric muons produced by cosmic-ray-induced air showers. Tracks are also caused by CC interactions of $\nu_\mu(\bar{\nu}_\mu)$, which produce a hadronic cascade and a μ^- (μ^+). When the neutrino interaction vertex is outside the detector volume, atmospheric muons and neutrino-induced muons are indistinguishable unless their energy and direction are considered, leading to *a through-going track*. When the vertex is inside the detector volume, both the hadronic cascade and the emerging muon track are visible, resulting in *a starting track*, which can only be caused by neutrino interactions. Although muons exhibit stochastic energy loss and are likely to exit the detector, resulting in poor energy resolution, the light deposition along an extended path (see Figure 3.9) provides good angular resolution (less than 1 degree), making tracks ideal for identifying high-energy astrophysical sources [83].

[83]: Aartsen et al. (2014), *Energy Reconstruction Methods in the IceCube Neutrino Telescope*

is there any nu sources paper that can be cited for this claim?

Tau neutrinos in IceCube exhibits variety of signatures, thanks to different tau decay modes (3.3). This leads to various event morphologies [84] based on factors like position of both, the neutrino interaction and tau decay verteces, decay channel and the decay length, as shown in Figure 3.10. The tau decay length (L_τ) is connected to Energy of tau lepton (E_τ) via $L_\tau \simeq \frac{50\text{m}}{1\text{PeV}} E_\tau$. ν_τ CC events typically produce two energy depositions: an initial interaction cascade followed by a tau decay product, which can be a track or cascade, depending on the decay channel. The muonic decay channel results in a dim tau track followed by a brighter muon track.*

[84]: Cowen (2007), *Tau neutrinos in IceCube*

* The stochasticity of muon energy losses and the low branching ratio of the muonic decay channel (17.4%) make it challenging to search for this signature. Therefore, this decay channel is excluded from the analysis presented in this thesis.

The other decay channels, involving hadrons or electrons, produce a cascade, leading to the so-called **double bang** events [85]. Around 59% of tau-neutrino interactions are double bang events.†

These double bang events are further classified based on whether both the interaction vertex and tau decay vertex are within the detector volume (see Figure 3.10). At lower energies (below (∼ 100) TeV), the separation between the two cascades is small, making them difficult to resolve. In some cases, if the event occurs close to a string or Digital Optical Module (DOM), two distinct time-connected pulses can be observed, known as the **double pulse** technique. However, identifying tau neutrino events in IceCube is challenging due to background muons and the difficulty in reconstructing such events. Recent developments using CNN classifiers have identified seven astrophysical tau neutrino candidates [86]. Lastly, if both of these caascades are contained in the active volume, and they are far enough to be reconstructed reliably, the morphology is called **double cascade**. This method has low and high tau energy threshold, since below certain energy (∼ 100 TeV) the decay length is quite short, making them indistinugishable from a usual cascade event, and energies above 10 PeV, (where theoretically the length should be large enough to separate the two cascades) one of the cascades will always be outside the detector volume. In such case, a larger detector volume, such as in IceCube Gen2, could extend the energy range for identifiable double cascade events (see Chapter 7).

The analysis performed in this thesis aims to measure neutrino flavour composiition where three of the morphologies explained above, starting tracks, double cascades and cascades (from hereon reffered to as single cascades, to differentiate from double) are used to identify flavour of the neutrino. Double cascades are not only challanging due to their tricky geometry but also because of involvement of both electromagnetic and hadronic particle showers involved. Lastly, as was discussed in **??**the medium (ice) itself has many characteristic properties that affects the reconstruction of these events drastically. Details of sampling these high energy starting events and reconstructing them in to these three morphologies will be explained in the next chapter.

[85]: Learned et al. (1995), *Detecting tau-neutrino oscillations at PeV energies*

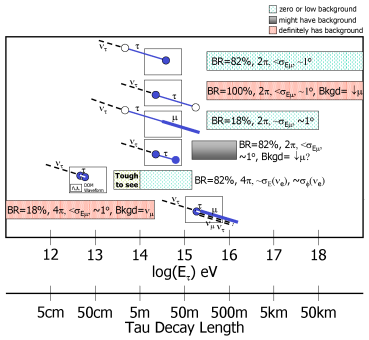

Figure 3.10: Various morphologis of ν_τ cc events in IceCube, as a function of E_τ and L_τ. Circle represent a cascade, dotted line represents primary ν_τ, thin line, Tau lepton track and thick line represent muon track.(Figure taken from [84])

[86]: Abbasi et al. (2024), *Observation of Seven Astrophysical Tau Neutrino Candidates with IceCube*

† The muonic decay of the tau has a branching ratio of around 17%, while all other decay channels of the tau produce another cascade with an inclusive branching ratio of approximately 83%. When multiplied by the fraction of the charged-current cross-section over the total cross-section [20], about 59% of all tau-neutrino interactions are double bang events.

Event Sample,(Re)construction and Particle Identification

4

4.1 Monte Carlo Simulation

4.1.1 Icecube simulation chain

4.1.2 SnowStorm Simulation

4.2 High Energy Starting Event (HESE) sample

4.3 Maximum Likelihood Event Reconstruction

4.4 Particle Identification of High Energy Neutrinos

4.4.1 Reclassification of PeV Double Cascades

4.4.2 Tau Polarisation

4.4.3 Glashow Cross-Section correction

4.5 Influence of South Pole Ice properties on Double Cascades Reconstruction

Flavour Composition Analysis | 5

Using the on the event sample (HESE) introduced in the previous chapter, where each event is reconstructed into one of three distinct morphologies (Single Cascades, Tracks and Double Cascades), a flavour measurement of the high energy diffuse neutrino spectrum can be performed. This chapter focuses on the methods and various components of this flavour measurement.

The chapter begins by detailing these statistical techniques, with a focus on forward folding likelihood fits, which plays a crucial role in distinguishing signal from background and identifying flavour contributions. In addition, different components and parameters introduced (or modified) in this iteration of the analysis are explained subsequently. Following this, the software used to perform the fit is discussed in detail. Finally, the chapter evaluates the sensitivity of the analysis, providing estimates of detection limits and the potential to constrain key physical parameters within the context of neutrino flavour identification.

5.1 Analysis Method

This analysis utilizes a binned maximum likelihood estimation (MLE) approach to perform statistical inferences on observed data. Binning the data offers computational efficiency by reducing the dimensionality of the problem, allowing for quicker calculations of likelihoods over a range of model parameters. Each analysis bin contains data points that represent a specific range of measured quantities, such as energy or angular distributions.

To incorporate the complexities of detector response and model uncertainties, the concept of forward folding is employed. Forward folding integrates theoretical model predictions with the response of the detector, producing expected distributions that can be directly compared to the binned observed data. This method allows for the inclusion of different flux models, systematic uncertainties, and detector efficiencies, all folded into the predicted likelihood. As a result, this approach enables robust and precise inference of underlying physical parameters, particularly in the context of high-energy astrophysics, where signal and background differentiation is challenging.

5.1.1 Binned Maximum-likelihood Fits

When fitting a data sample with a large size (large N), it is common practice to bin the data in order to enhance the computational efficiency of the likelihood function calculation. This binning procedure groups the data into discrete intervals, or *bins*, based on one or more *observables*, such as energy or zenith. This simplification is not harmful as long as the variation of the probability density function (PDF), $f(x|\theta)$, within each bin is insignificant compared to its variation across all the bins. In

other words, the binning should not discard crucial information about the parameter vector θ that governs the underlying physical model. If binning is applied appropriately, the process retains the ability to accurately infer the parameters of interest while significantly speeding up the computational process, particularly in high-dimensional analyses where unbinned likelihood fits may be computationally prohibitive.

The binned likelihood method works by comparing the number of observed events in each bin to the expected number of events, which are typically predicted through Monte Carlo simulations. In the analysis, these Monte Carlo templates are created for various theoretical flux components, such as astrophysical, atmospheric etc. for both signals or background. Each template provides a predicted event distribution based on specific values of the *signal* parameters θ along with *nuisance* parameters, ξ, which describe the physical processes being studied. These templates are then forward folded, meaning they incorporate the effects of the detector response, before being compared to the observed data. By adjusting the model parameters, the predicted event counts in each bin can be varied to find the *best fit* to the data. The number of observed events n, in each bin i (n_i), is assumed to follow a Poisson distribution [87]. The expected number of events in bin i, $\mu_i(\theta, \xi)$, represents the sum of contributions from all signal and background components. The Poisson likelihood for a given bin is defined as:

[87]: Behnke et al. (2013), *Parameter Estimation*

$$P(n_i|\mu_i(\theta,\xi)) = \frac{\mu_i(\theta,\xi)^{n_i} e^{-\mu_i(\theta,\xi)}}{n_i!} \tag{5.1}$$

where $\mu_i(\theta, \xi)$ is the expected number of events in bin i and n_i is the observed number. The total likelihood for the entire dataset is then the product of the likelihoods for all bins:

$$\mathcal{L}(n|\mu_i(\theta,\xi)) = \prod_{i=1}^{N} P(n_i|\mu_i(\theta,\xi)) \tag{5.2}$$

Incorporating systematic uncertainties into the likelihood function is crucial for obtaining realistic results, as these uncertainties often arise from imperfect detector calibration or background estimations. Such systematic uncertainties are modeled as nuisance parameters in the likelihood fit. These parameters are typically constrained by prior knowledge and treated as additional variables in the fitting process. For each of the k nuisance parameters, ξ_j, a Gaussian prior is introduced, penalizing deviations from the central value $\bar{\xi}_j$ by an amount proportional to the known uncertainty σ_{ξ_j}, changing the likeli:

$$\mathcal{L}(n|\mu_i(\theta,\xi)) = \prod_{i=1}^{N} P(n_i|\mu_i(\theta,\xi)) \prod_{j=1}^{k} \exp\left(-\frac{1}{2}\left(\frac{\xi_j - \bar{\xi}_j}{\sigma_{\xi_j}}\right)^2\right) \tag{5.3}$$

By maximizing this likelihood, the best-fit parameters θ can be found. In practice, the fit is performed by minimizing $-\ln\mathcal{L}$, as it simplifies the computation (see 5.4).

$$\ln(\mathscr{L}(n|\mu_i(\theta,\xi))) = \sum_{i=1}^{N}[n_i\ln(\mu_i) - \ln(n_i!) - \mu_i] - \sum_{j=1}^{k}\frac{1}{2}\left(\frac{\xi_j - \bar{\xi}_j}{\sigma_{\xi_j}}\right)^2 \tag{5.4}$$

This modified likelihood is often referred to as the **profile likelihood**, as it profiles over the nuisance parameters by marginalizing or constraining them using prior information.

Once the likelihood function is constructed, the next step is hypothesis testing. A specific model hypothesis can be tested by using a likelihood ratio test. The likelihood ratio compares two hypotheses: the test model (with parameters θ_t) and the best-fit model (with parameters $\hat{\theta}$):

$$-2\Delta\ln\mathscr{L} = -2\ln\left(\frac{\mathscr{L}(n|\mu(\theta_t,\xi_t))}{\mathscr{L}(n|\mu(\hat{\theta},\hat{\xi}))}\right) \tag{5.5}$$

The factor -2 is included for convenience, as it allows the test statistic to follow a χ^2-distribution, according to Wilks' theorem [88]. This enables the calculation of confidence levels (CL) of the parameter of interest without the need for computationally expensive Monte Carlo simulations. However, Wilks' theorem is only valid when the dataset is large and the model parameters are unbounded. If either condition is not met, the test statistic may deviate from a χ^2-distribution, necessitating the use of Monte Carlo pseudo-experiments to determine the confidence intervals via the so-called *Feldman Cousins* method [89], with an extension to incorporate nuisance parameters [90, 91].

[88]: Wilks (1938), *The Large-Sample Distribution of the Likelihood Ratio for Testing Composite Hypotheses*

[89]: Feldman et al. (1998), *Unified approach to the classical statistical analysis of small signals*

[90]: Sen et al. (2009), *On the unified method with nuisance parameters*

[91]: Cowan et al. (2011), *Asymptotic formulae for likelihood-based tests of new physics*

The test statistic derived from the likelihood ratio can be used to construct confidence regions for the parameters of interest. For instance, in one-dimensional parameter scans, the confidence interval is obtained by comparing the test statistic to the cumulative distribution of a χ^2-distribution with one degree of freedom. When scanning over two or more parameters, a multi-dimensional profile likelihood scan is required, which significantly increases the computational complexity. In some cases, the Asimov dataset [91]—a single dataset representing the median outcome of many pseudo experiments—can be used to estimate the median sensitivity of the analysis. This method provides an efficient way to estimate confidence intervals and test the sensitivity of the analysis without the need for exhaustive Monte Carlo trials. Asimov dataset and Wilks' theorem are both used to derive sensitivity presented in 5.3. It is important to point out that the primary parameter of interest in this analysis is the astrophysical neutrino flavour fractions, which are constrained to be non-negative ($\phi_{\nu_\tau} \geq 0$) and limited by the small number of observed double cascade events. As a result, the applicability of Wilks' theorem is evaluated as needed.

5.1.2 SAY Likelihood

The likelihood construction described in section 5.1.1 relies on the Poisson likelihood, which assumes that the expectations for each bin, μ_i, are

known exactly. This assumption holds when the Monte Carlo simulations used in generating the expected distributions have large statistics. However, MC simulations inherently come with their own uncertainties due to finite statistics, particularly in bins with lower event counts.

In binned forward-folding fits, statistical inferences are made by comparing observed data counts in each bin to the expected counts derived from the simulations. As outlined in Equation 5.1, the Poisson likelihood assumes that μ_i, the expected value per bin, is well-determined. However, this is often not the case in analyses like ours, where overall event rates are low, and individual bin expectations may fluctuate significantly due to limited MC statistics. This mismatch can lead to deviations between the observed data and MC predictions if these fluctuations in μ_i are not correctly accounted for.

To address this issue, an extended form of the Poisson likelihood ($\mathcal{L}_{\text{eff}}$), or the so-called **SAY likelihood**, is used in this analysis [92]. This likelihood incorporates the uncertainty from the limited MC statistics and provides more appropriate coverage of the expected μ_i values. Specifically, the distribution of MC event weights in each bin is corrected using a scaled Poisson distribution, which introduces an additional uncertainty term, σ_j^2, for each bin. This term depends on the weights w_i^j of the MC events in the j-th bin and is defined as:

[92]: Argüelles et al. (2019), *A binned likelihood for stochastic models*

$$\sigma_j^2 = \sum_i (w_i^j)^2 \tag{5.6}$$

This uncertainty term, σ_j^2, is larger in bins with low statistics, and smaller in bins with higher statistics, ensuring that fluctuations in low-stat bins are adequately covered. This formalism results in more conservative limits, with generally wider contours for the final result, as the additional statistical uncertainty is incorporated into the fit. One limitation of this approach is that the Asimov dataset [91], described in the previous section, is not applicable with the SAY likelihood. This is because the σ_j term can significantly alter μ_i in each bin, making it impossible to recover the injected model parameters. As a result, deviations from injected values may appear, especially in cases like the `MuonGun`, discussed in the next section. Alternatively, the standard Poisson likelihood can be used, though the resulting limits may be less conservative than the reality accounted for by the SAY likelihood.

[91]: Cowan et al. (2011), *Asymptotic formulae for likelihood-based tests of new physics*

5.2 Components of the fit

The choice of the likelihood function and its subsequent requirement was outlined in the previous section. In this section, the focus shall be on the actual construction of the likelihood and the essential components involved. The construction proceeds as follows:

1. The parameters to be measured, known as *signal parameters* (denoted by θ), along with all *nuisance parameters* (ξ), which may originate from detector systematics or background modeling (such as atmospheric spectra), are identified and bounded where necessary.

2. These parameters are applied in the form of the neutrino *flux*, assigning each Monte Carlo event a specific *weight* based on the individual fluxes.
3. A set of observables that are most sensitive to the signal parameters, such as astrophysical neutrino fluxes, is selected and appropriately binned for analysis.
4. The experiment is performed, and the observed data events n are sorted into the predefined bins of the analysis histograms. A fit is conducted by varying each of the parameters (and, consequently, the fluxes) until the observed data events are optimally described.

This is why a penalty term is introduced in the likelihood. A Gaussian prior ensures that the parameters remain within the 1σ prior region, penalizing the likelihood if the fit favors values outside this range.

5.2.1 Model parameters

All the model parameters used in the fit, along with which fluxes they affect, are listed in Table 5.2. The model parameters consist of either flux components (astrophysical or atmospheric) or detector systematics. Baseline models and their corresponding values, wherever applicable, are specified for each parameter, along with the choice of priors. The astrophysical flux parameters represent the high-energy neutrino contributions from distant sources, while atmospheric flux models account for neutrinos originating from cosmic ray interactions within in atmosphere of Earth. Detector systematics reflect uncertainties in detector performance.

Table 5.1: Parameters used in the likelihood desribed in Equation 5.3. The gaussian priors on the parameters (if applicable) in terms of the mean (μ) and width (σ) are stated on the alongside.

Parameter	Prior (μ, σ)
Astrophysical Flux (Signal) Parameters	
astro. ν_μ normalisation [10^{-18}GeV^{-1}cm^{-2}sr^{-1}s^{-1}](ϕ_{ν_μ})	-
astro. spectral index (γ_{astro})	-
scaling factor to modify total flux norm ($\Phi^{\text{astro}}_{\nu+\bar{\nu}}$) relative to ϕ_{ν_μ} (s_{ν_e} astro. ν_e)	-
astro. ν_τ scaling factor to modify total flux norm ($\Phi^{\text{astro}}_{\nu+\bar{\nu}}$) relative to ϕ_{ν_μ} (s_{ν_τ})	-
Atmospheric Flux Systematics	
Conventional Flux normalisation (Φ_{conv})	(1.0,0.2)
Prompt Flux Normalisation (Φ_{prompt})	-
Interpolation between Cosmic Ray Models (ξ_{CR})	(0,1)
Cosmic Ray Spectral Index Shift ($\Delta\gamma_{\text{CR}}$)	(0,0.05)
Barr-parameter modifying the pion-contribution (H_{Barr})	(0,0.15)
Barr-parameter modifying the kaon-contribution (W_{Barr})	(0,0.40)
Barr-parameter modifying the pion-contribution (Y_{Barr})	(0,0.30)
Barr-parameter modifying the pion-contribution (Z_{Barr})	(0,0.12)
Muon Flux Normalisation (Φ_{muongun})	(1,0.5)
Scale factor for Neutrino Nucleon Inelasticity weight (I_{scale})	(1,0.1)
Detector Systematics	
Optical Efficiency of DOMs (η_{domeff})	(1.0,0.1)
Ice Absorption Scaling (η_{abs})	(1.0,0.05)
Ice Scattering Scaling (η_{scat})	(1.0,0.05)
Parametrization for refrozen icecolumn ($\eta_{\text{h.ice}-\text{p0}}$)	(-0.27,0.5)
Parametrization for refrozen icecolumn ($\eta_{\text{h.ice}-\text{p1}}$)	(-0.042,0.05)
Ice Anisotropy Scaling (η_{aniso})	-

The flux of astrophysical neutrinos is modeled as a single power law of the form

$$\Phi^{\text{astro}}_{\nu+\bar{\nu}} = \Phi^{\text{astro}}_{0} \times (1 + s_{\nu_e} + s_{\nu_\tau}) \times \left(\frac{E_\nu}{100\,\text{TeV}}\right)^{-\gamma_{\text{astro}}} \tag{5.7}$$

where γ_{astro} is the spectral index, E_ν is the neutrino energy, and $\Phi^{\text{astro}}_{\nu+\bar{\nu}}$ is the all-flavor (including particle and anti-particle) normalization. Two scaling factors, s_{ν_e} and s_{ν_τ}, modify the flux of electron and tau neutrinos relative to the muon neutrino flux Φ_0. These scaling factors help determine the flavour ratio $\nu_e : \nu_\mu : \nu_\tau$ as:

$$f_e = \frac{s_{\nu_e}}{(1+s_{\nu_e}+s_{\nu_\tau})}, \quad f_\mu = \frac{1}{(1+s_{\nu_e}+s_{\nu_\tau})}, \quad f_\tau = \frac{s_{\nu_\tau}}{(1+s_{\nu_e}+s_{\nu_\tau})} \tag{5.8}$$

The signal parameters for the flavor analysis are these two scaling factors, Φ_0, and γ_{astro}. All other subsequent parameters explained are the nuisance parameters. In Eq. 5.13, it is assumed that each flavor has an identical spectral shape (γ_{astro}). This assumption is justified because the HESE sample used in this analysis is small and has limited power to constrain individual spectra for each flavor. For the sensitivity study described in **??**, the benchmark spectral parameter values are taken from the previous iteration of this analysis [93], with $\gamma_{\text{astro}} = 2.87$ and $\Phi_0 = 2.12 \times 10^{-18} \text{GeV}^{-1}\,\text{cm}^{-2}\,\text{sr}^{-1}\,\text{s}^{-1}$ assuming an equipartition of flavor ratios (i.e., $\nu_e : \nu_\mu : \nu_\tau = 1 : 1 : 1$).

[93]: Abbasi et al. (2021), *IceCube high-energy starting event sample: Description and flux characterization with 7.5 years of data*

Atmospheric flux components are constrained by priors because they are more accurately measured with other IceCube data samples. The high-energy starting event selection is very efficient in reducing atmospheric muons due to the veto requirement and the down-going atmospheric neutrinos from the same cosmic-ray-induced air shower, thanks to the self-veto effect.

Depending on the parent hadron type, the atmospheric neutrino flux is divided into two components: **Conventional neutrino flux** (produced via decay of charged pions and kaons) and **Prompt Neutrino Flux** (produced via decay of charmed mesons). The various models of atmospheric neutrino fluxes are detailed in 2.1.2. The atmospheric neutrino contribution is modeled using the Matrix Cascade Equation Solver (MCEq) [94]. The baseline primary cosmic-ray model for this calculation is H4a [95], combined with a hadronic interaction model `SIBYLL2.3c` [96], introducing conventional (Φ_{conv}) and prompt (Φ_{prompt}) flux normalizations to account for background contributions from these fluxes. Additionally, they are folded with the generalized self-veto probability, as described in 4.2, to account for the reduced rate of atmospheric neutrinos accompanying vetoed muons from the same cosmic-ray-induced air shower. Other nuisance parameters modifying the shape of these spectra include ξ_{CR}, which interpolates between two primary cosmic-ray models H4a and GST (see section 2.1.2), an approach similar to [97]. The cosmic-ray model uncertainty is critical in this analysis, as it is the largest source of uncertainty in the overall atmospheric background. Furthermore, $\Delta\gamma_{\text{CR}}$ accounts for corrections in the spectral index of the primary cosmic-ray spectrum, following [98]. Uncertainties in the hadronic interaction models, due to various π and K production cross-sections in different energy phases, introduce energy-dependent variations in atmospheric flux expectations [99]. These nuisance parameters, referred to as *Barr*

[94]: Fedynitch et al. (2015), *Calculation of conventional and prompt lepton fluxes at very high energy*

[95]: Gaisser (2012), *Spectrum of cosmic-ray nucleons, kaon production, and the atmospheric muon charge ratio*

[96]: Riehn et al. (2018), *The hadronic interaction model SIBYLL 2.3c and Feynman scaling*

[97]: Abbasi et al. (2022), *Improved Characterization of the Astrophysical Muon–neutrino Flux with 9.5 Years of IceCube Data*

[98]: Niederhausen (2018), *Measurement of the High Energy Astrophysical Neutrino Flux Using Electron and Tau Neutrinos Observed in Four Years of IceCube Data*

[99]: Barr et al. (2006), *Uncertainties in Atmospheric Neutrino Fluxes*

parameters, are computed as described in [100]. A detailed discussion on implementing these parameters within the software framework can be found in [101].

[100]: Fedynitch et al. (2022), *Data-driven hadronic interaction model for atmospheric lepton flux calculations*

[101]: Naab (2024), *Evidence for a Break in the Diffuse Extragalactic Neutrino Spectrum*

As mentioned, the veto and charge/energy cuts effectively reduce atmospheric neutrinos. However, high-energy single muons can still enter the detector, contaminating the sample. A separate nuisance parameter, Φ_{muongun}, is included in the fit to account for these muons. **The atmospheric Muon Flux** component is constrained by a prior partially derived from experimental data. The spectral shape is determined using a dedicated simulation that produces a flux of single muons reaching the detector (MUONGUN, described in 4.1), weighted assuming the same baseline models used for atmospheric spectra (H4a). A pure-proton composition is chosen for these muons as it contributes the highest energy single muons. The normalization is estimated using the tagging method described in [93]. A prior derived from this study is applied in this analysis. The sensitive energy range of this analysis is high, and the sample is specifically designed to minimize background contamination from atmospheric neutrinos and muons (see Section 4.2). The available MUONGUN Monte Carlo was generated for various other IceCube analyses, that targeted lower energies as well, where background contributions are significantly higher. Most Monte Carlo events do not pass the strict cuts of this analysis, with no events at all in the cascade and double cascade bins (see Figure 5.4 and Figure 5.6). Consequently, the statistical uncertainty on this component is high, requiring a Kernel Density Estimate (KDE) template for smoothing.

The remaining nuisance parameters are those arising from the imperfect knowledge of the detector components, such as the Digital Optical Modules (DOMs, see section **??**), and the detection medium, which includes both the bulk ice and hole ice models (see section 3.2), known from here-on as **Detector Systematics**. These detector systematics introduce uncertainties that can affect both the threshold and the shape of observable distributions, thereby altering the expected event rates from different flux components. Unlike previous iterations of this analysis [71, 102], which relied on discrete Monte Carlo sets with different values for systematics that significantly impacted the analysis observables, the current approach uses the SnowStorm simulation technique (see section **??**). The SnowStorm method [103] captures the full range of detector systematic variations in a single Monte Carlo dataset, avoiding the need for generating multiple datasets. It uses a first-order Taylor expansion of the observables, such as event counts in each bin, with respect to the detector systematics. The resulting gradient, called *the nuisance gradient* ($\vec{G}$), allows for efficient computation of observable values as these systematic parameters vary. The expectation value of per bin event count μ, for nuisance parameter variations $\vec{\eta}$ is given as,

[71]: Usner (2018), *Search for Astrophysical Tau-Neutrinos in Six Years of High-Energy Starting Events in the IceCube Detector*

[102]: Stachurska (2020), *Astrophysical Tau Neutrinos in IceCube*

[103]: Aartsen et al. (2019), *Efficient propagation of systematic uncertainties from calibration to analysis with the SnowStorm method in IceCube*

$$\mu(\vec{\eta}) = \mu_{\text{baseline}} + \vec{\eta}.\vec{G} \tag{5.9}$$

where, μ_{baseline} is the expectation value of per bin count at basleine values of all detector systematic parameters (baseline values are the central value at which simulation was generated), when $\vec{\eta} = \vec{0}$. For this approach to be valid, it assumes that systematic effects are small enough to be treated perturbatively, allowing for a linear approximation. By marginalizing

over the full ensemble of systematic variations, the prediction converges to that of the central model, effectively neglecting second-order effects. Because the dataset itself have finite statistics, appropriate uncertainty propagation is applied to the nuisance gradient (see [101] for details of calculations of this gradient, their uncertainties and incorporation within such fits).

[101]: Naab (2024), *Evidence for a Break in the Diffuse Extragalactic Neutrino Spectrum*

For each analysis bin, both the expected number of events and the associated variance are computed. However, two important caveats should be noted with this method. First, the gradients are calculated based on a specific flux assumption[1] and are not recalculated at every minimization step. This significantly reduces the computational time of the minimization process but may introduce inaccuracies if the assumed fluxes deviate significantly from the true values in nature, which could substantially alter the resulting gradients. A potential solution is to compute the gradients over a range of flux assumptions to check for significant deviations in the results. The second caveat arises because the expected event counts per bin, calculated using the gradients as shown in Equation 5.9, are applied as an *additive* correction to the overall flux expectation. Since the gradient is a vector, it can also take negative values. For softer spectra and the limited statistics of the HESE sample, this can result in negative bin counts when the expected values approach zero. This presents a problem for the likelihood fit used in the analysis, as the logarithm of a negative number cannot be computed (which the fitter will attempt to do at some point; see Equation 5.4). To avoid this numerical issue, the expectation value calculated via the gradients is clipped at $\mu = 0 + \epsilon$. This ad hoc correction is justified because, although μ_{baseline} may be zero in these bins, there remains significant statistical uncertainty, which typically dominates over the systematic variations.

1: For the analysis presented in this thesis, the gradients are computed using the best-fit values from the HESE-7.5 year analysis [93], with $\gamma_{\text{astro}} = 2.87$, the per-flavour flux normalization $\Phi^{\text{astro}}_{\nu+\bar{\nu}} = 2.12$, and an equipartition among all three flavour fluxes.

The aforementioned gradient, can be constructed using all or part of detector systematics simulated within the snowstrom ensemble. For the analysis presented in this thesis, it is constructed using 6 parameters, listed in the Table 5.2.

The DOM Efficiency (η_{domeff}) accounts for factors like the quantum efficiency of the PMT and shadowing by attached cables, reducing the efficiency by 1%. The overall uncertainty is estimated at ±10%. This impacts the reconstructed energy, as lower efficiency underestimates the photon light yield. This effect is relevant in the analysis, as it shifts the energy distribution across bins and the energy thresholds in particular.

Absorption (η_{abs}) and Scattering (η_{scat}) Scaling accounts for variations in scattering and absorprion coefficients of ice mapped across depth grid of the south pole ice. The baseline model for this mapping is SPICE-3.2.1, with priors set to a 5% width around the central value, based on the uncertainty derived from calibration data obtained using flasher LEDs.. An increase in scattering coefficients extends the photon scattering path, increasing the chance of absorption before detection. Variations in ice scattering and absorption mainly affect energy reconstruction and may introduce minor directional bias, with the energy shift being the primary concern in this analysis.

hole ice parameters ($\eta_{\text{h.ice}-\text{p0}}$ and $\eta_{\text{h.ice}-\text{p1}}$) accounts for the differences in optical properties between the refrozen ice in the DOM deploy-

ment columns and the surrounding bulk ice. Uncertainties and priors are based on a recent study that analyzed flasher data [104].

Ice anistropy discussed in detail in sections 3.2 and 4.5 affects the double cascade reconstruction greatly. For the icemodel used in simulation, this parameter is modelled as a modulation of the nominal scattering coefficient, analogous to thay used in [105].

[104]: Eller et al. (2023), *A model independent parametrization of the optical properties of the refrozen IceCube drill holes*

[105]: Abbasi et al. (2022), *Detection of astrophysical tau neutrino candidates in IceCube*

Lastly, an additional nuisance parameter, affecting all the neutrino fluxes (Astrophysical and atmospheric) is used that modifies overall normalisation of these fluxes, **Neutrino-Nucleon Inelasticity Scaling (I_{scale})**. This parameter is introduced to account for inelasticity which is a measure of the fraction of the neutrino's energy that is transferred to the hadronic system in an inelastic neutrino nucleon scattering process, mathematically given as,

$$y = \frac{E_{\text{hadron}}}{E_\nu} \tag{5.10}$$

Mean inelasticity $\langle y \rangle$ is the average value of the inelasticity y over many scattering events. It provides a statistical measure of the average fraction of the neutrino's energy that is transferred to the hadronic system. This becomes particularly relevant for the starting tracks as, $\langle y \rangle$ is energy dependednt and hence amount of energy transferred to the muon after ν_μ CC interaction, will therefore be different for different energies of Neutrino (and hence different events). For this analysis, a scaling factor is introduced, which is based on formulation provided in [35], that allows to vary Normalisation N of the inelasticity distribution,

[35]: Aartsen et al. (2019), *Measurements using the inelasticity distribution of multi-TeV neutrino interactions in IceCube*

$$\frac{dp}{dy} = N\left(1 + \epsilon(1-y)^2\right) y^{\lambda-1} \tag{5.11}$$

where N is the normalisation given as,

$$N = \frac{\lambda(\lambda+1)(\lambda+2)}{2\epsilon + (\lambda+1)(\lambda+2)} \tag{5.12}$$

The theoretical prediction of $\langle y \rangle$ from the CSMS tables [28] is calculated for the mean inelasticity distribution for a given event. By fixing $\langle y \rangle$, λ 5.12 is the fitted to apply a reweighting factor to *scale* the inelasticity (I_{scale}). Variations are permitted within 10% of their default value. The parameter is applied to all neutrino fluxes as it can affect any fluxes where a neutrino interacts via Deep Inelastic Scattering.

[28]: Cooper-Sarkar et al. (2011), *The high energy neutrino cross-section in the Standard Model and its uncertainty*

5.2.2 Analysis Observables and their Distributions

In forward folding fits, selecting appropriate observables is crucial for distinguishing between the signal and background hypotheses. The analysis uses all the HESE events above 60 TeV, further divided in 3 sub-samples of *Single Cascades, Tracks and Double Cascades*. These 3 sub-samples are binned in 2-dimensional monte carlo templates of appropriate observables, such that bakground and signal templates are clearly distingishabe. For example, when measuring the spectrum of astrophysical neutrinos, the background consists of neutrinos from other sources, primarily atmospheric fluxes. Key observables that allow for effective differentiation between astrophysical and atmospheric neutrinos include the total deposited energy (E_{tot}) and the zenith angle (θ_{zenith}) of

the interacting neutrino. The motivation for focusing on these variables stems from their distinct behavior in atmospheric and astrophysical neutrino spectra (see Section 2.1.2). In particular, down-going atmospheric neutrinos are efficiently suppressed due to the self-veto effect, while up-going atmospheric neutrinos, which cannot be reduced by this veto, become an irreducible background.

The astrophysical spectrum that is assumed for all the monte carlo templates and sensitivity is using a single-power law based on best-fit values of HESE-7.5 years spectrum measurements [93], given as,

$$\frac{d\Phi^{\text{astro}}_{\nu+\bar{\nu}}}{dE} = 6.98.10^{-18}\left(\frac{E_\nu}{100\,\text{TeV}}\right)^{-2.87} \quad (5.13)$$

In units of $\text{GeV}^{-1}\,\text{cm}^{-2}\,\text{s}^{-1}\,\text{sr}^{-1}$, with flavour composition of $\nu_e : \nu_\mu : \nu_\tau = 1 : 1 : 1$
The prompt component is missing from all templates as best-fit value of Φ_{prompt} of prompt flux normalization was 0.

For the analysis presented in this thesis, the primary goal is to measure the flavor composition of astrophysical neutrinos. A key component of this analysis, as highlighted in Section 4.4, is the identification and classification of ν_τ-induced double cascade events. NOte that the PID assigned is not used as a proxy to tag flavour on an individual event bases, but through statistical analyses of the overall data set, by using Monte Carlo templates. Double cascades are a signature of ν_τ interactions, and their identification relies heavily on the observables E_{tot} and the reconstructed double cascade length (L_{dc}), which provide the most discriminatory power for separating the flavors of astrophysical neutrinos, see Figure 5.1. All double cascade events are binned into a two-dimensional Monte Carlo template, with one axis representing the reconstructed tau decay length (L_{dc}) and the other representing the reconstructed total deposited energy (E_{Tot}). The L_{dc} is divided into 10 bins ranging from 10 m to 1000 m, while E_{Tot} is divided into 13 bins spanning 60 TeV to 12.6 PeV, both using logarithmic spacing, as shown in Figure 5.1. It is important to note that adding a third dimension, such as energy asymmetry, offers significant discriminatory power by reducing the low-length single cascade background, enhancing the sensitivity to measure the flavor ratio [106]. However, a detailed study revealed that the limited Monte Carlo statistics and small sample size of the HESE data resulted in many empty bins, which posed challenges for forward-folding fits. As a result, the third dimension was ultimately excluded from the analysis.

[106]: Lad et al. (2023), *Summary of IceCube tau neutrino searches and flavor composition measurements of the diffuse astrophysical neutrino flux*

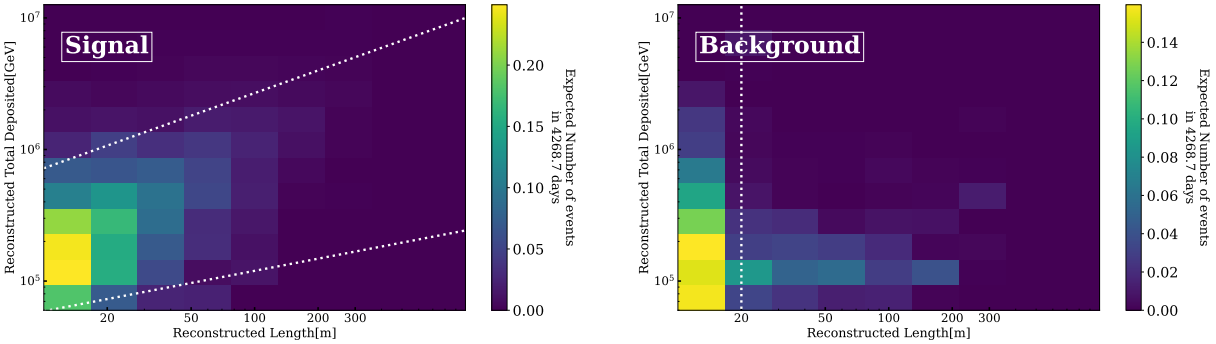

Figure 5.1: 2D Monte Carlo templates, constructed using reconstructed total energy (E_{Tot}) and double cascade length (L_{dc}) for events classified as **double cascades**. The signal (left), representing ν_τ-induced double cascades, shows a clear correlation between L_{dc} and E_{tot}, with 68% of events within the indicated signal region (dotted white line). In contrast, the background (right), consisting of ν_μ and ν_e events, lacks this correlation and clusters at low L_{dc}, 68% of all the background events lying below the indicated white dotted verticle line.

Under the double cascade hypothesis, true single cascades are typically reconstructed with a small L_{dc} but with most of their energy concentrated in the first cascade (with the energy asymmetry $E_A \rightarrow 1$). Hence, misclassified single cascades tend to cluster around low L_{dc} and low E_{Tot}, with the distribution of L_{dc} falling off rapidly, as indicated by the verticle line, on right panel of Figure 5.1. In cases where a track is reconstructed under the double cascade hypothesis, the largest energy depositions are interpreted as the cascade vertices, leading to an arbitrary L_{dc} value.

These tracks, when misclassified as double cascades, typically exhibit low E_{Tot}, consistent with the falling astrophysical spectrum. This is too visible in right panel of Figure 5.1.

True double cascades from ν_τ-CC interactions, on the other hand, exhibit a strong correlation between L_{dc} and E_{Tot}, see. This correlation between L_{dc} and E_{Tot} is primarily used to determine the compatibility of an event with a ν_τ interaction as opposed to another flavor. The Monte Carlo distributions (PDFs) of ν_τ-induced double cascades clearly show this correlation (see left panel of Figure 5.1, indicating 68% region of all classified true double cascade events).

For single cascades and tracks, the observables E_{Tot} (21 bins from 60TeV to 12.6 PeV in log space) and $\cos(\theta_z)$ (10 bins from -1 to 1 in cosine space) are commonly used, as they offer the most significant discrimination between astrophysical and atmospheric neutrinos, as shown in Figure 5.2 for cascades and Figure 5.3 for tracks. In both Figures, the supression of atmospheric neutrinos (right panel) ($\cos(\theta_z)$>0.25, the so-called *down-going region* for in IceCube) is clearly visible due to self-veto effects, whereas astrophysical template (left panel) shows no such pattern, indicating neutrinos from all directions are accepted.

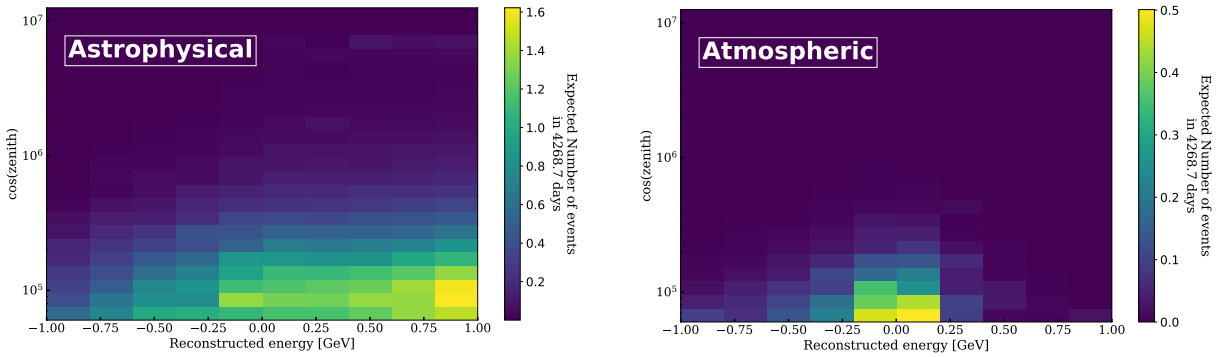

Figure 5.2: 2D Monte Carlo templates, constructed using reconstructed total energy (E_{Tot}) and reconstructed zenith ($\cos(\theta_z)$) for events classified as **single cascades**. The signal (left), representing *Astrophysical neutrinos* of the sample and the background (right), representing *Atmospheric neutrinos*, including conventional, prompt and single muon fluxes.

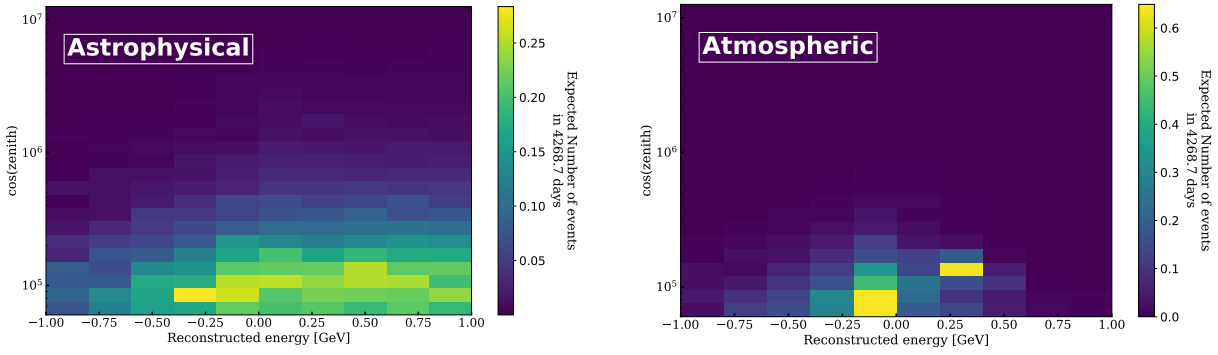

Figure 5.3: 2D Monte Carlo templates, constructed using reconstructed total energy (E_{Tot}) and reconstructed zenith ($\cos(\theta_z)$) for events classified as **tracks**. The signal (left), representing *Astrophysical neutrinos* of the sample and the background (right), representing *Atmospheric neutrinos*, including conventional, prompt and single muon fluxes.

This becomes more evident in one dimensional distribution for both of these subsamples (Figure 5.4 for cascades and Figure 5.5 for tracks), where total expectation is broken down in individual flux contributions (as desribed in 5.2.1). In case of Energy distribution of single cascades

(right panel of Figure 5.4), except for lower energy bins (up to ~ 110 TeV), astrophysical single cascade events dominates. Glashow peak due to $\bar{\nu}_e$ is clearly visible too. Note the missong muon component, due to lack of enough MUONGUN simulation, as described in 5.2.1. For Tracks (Figure 5.5), although there is a similar supression due to self veto effects, but the constribution of single muons, simulated using MUONGUN events, is clearly visible, dominating in the same down-going region. As described before, the template is noisey due to large monte carlo uncertainties. In general, tracks sample shows larger contribution due to atmospheric fluxes compared to single cascades[2]. Similar 1 dimensional distributions of L_{dc} and E_{Tot} are shown for completeness, but as described before, double cascades do not show any striking differences going from astrophysical to atmopsheric fluxes as background is due to ν_e and ν_μ events.

2: recall that single cascades also show contributions from all flavour Neutral Current (NC) interactions

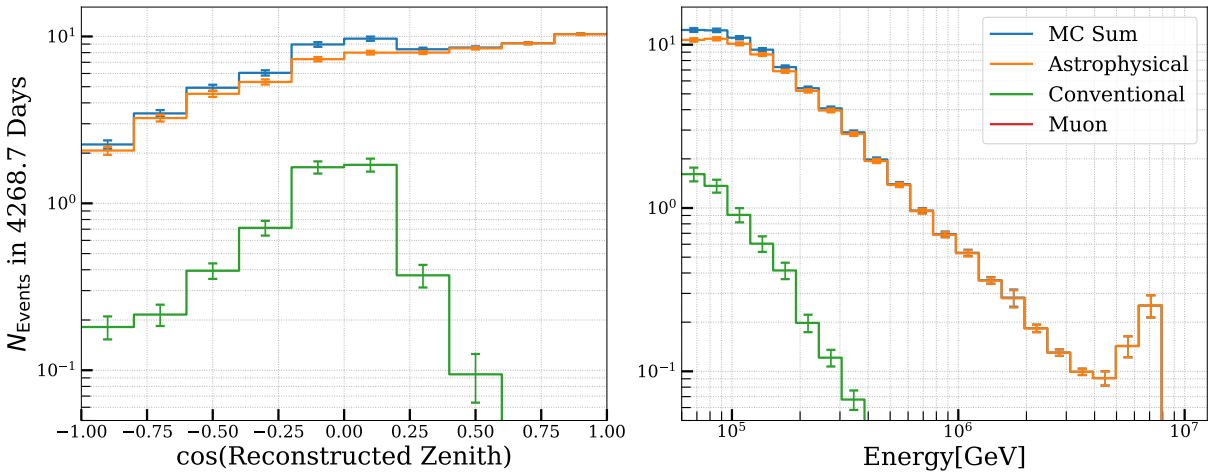

Figure 5.4: One dimensional observable distribution, for HESE Single Cascades showing expected number of events as a function of reconstructed energy (right) and reconstructed zenith (left), broken down into different flux components. Only statistical errors are shown.

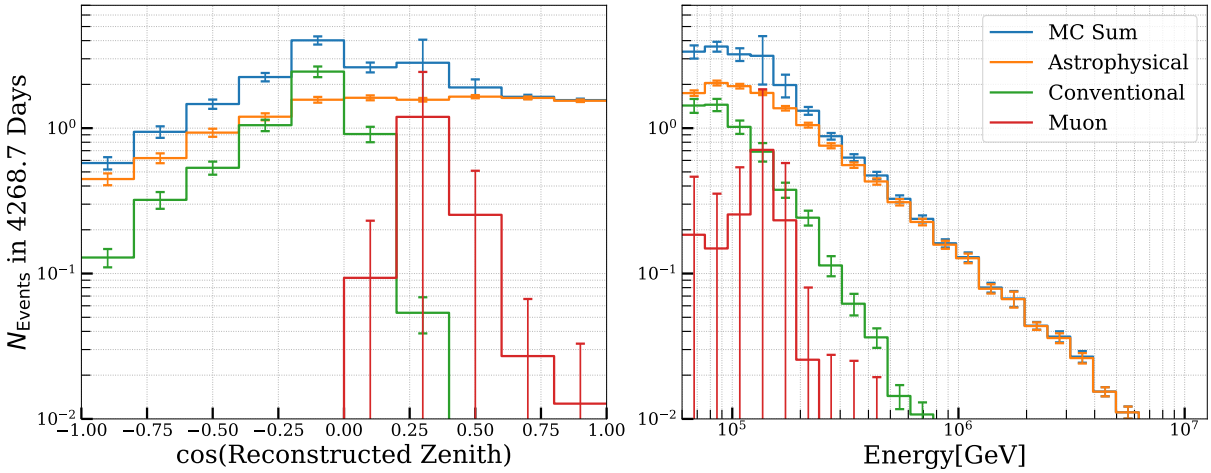

Figure 5.5: One dimensional observable distribution, for HESE Tracks showing expected number of events as a function of reconstructed energy (right) and reconstructed zenith (left), broken down into different flux components. Only statistical errors are shown.

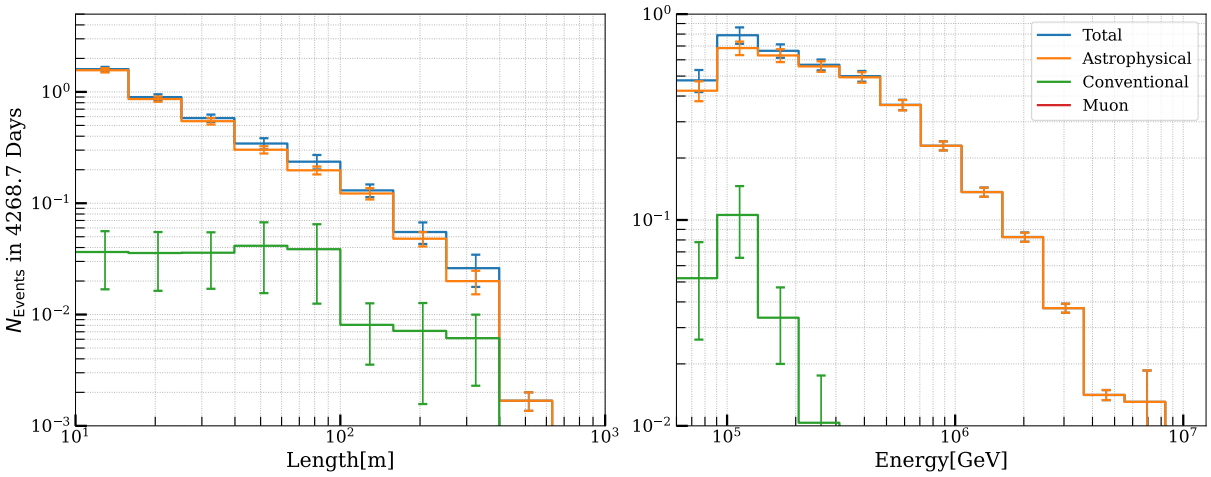

Figure 5.6: One dimensional observable distribution, for HESE DOuble Cascades showing expected number of events as a function of reconstructed energy (right) and reconstructed tau decay length (left), broken down into different flux components. Only statistical errors are shown.

5.3 Analysis Sensitivity

All fits and related calculations are carried out using a software toolkit called **`NNMFit`**. Developed within the IceCube collaboration, `NNMFit` has been applied in many other IceCube analyses. Essentially, the toolkit handles the statistical modeling required for forward-folding fits using high-energy neutrino data with binned likelihoods. It supports Monte Carlo event weighting, testing various flux models using signal and nuisance parameters, applying systematic detector uncertainties, and performing fits to data. The toolkit also enables joint fitting across different event selections. The `aesara` backend allows fast and efficient forward folding of Monte Carlo samples, even for large datasets, and offers automated differentiation that greatly assists in optimizing likelihood functions. More details on this toolkit are found in [101].

[101]: Naab (2024), *Evidence for a Break in the Diffuse Extragalactic Neutrino Spectrum*

any other thesis/paper/links required??

Using all the ingredients in the form of fluxes constructed from signal and nuisance parameters, and following the described method, the flavor composition parameter space is scanned to obtain a two-dimensional confidence region for the flavor composition, as shown in Figure 5.7. To derive these limits, an Asimov dataset is constructed (see Section 5.1), assuming the benchmark astrophysical neutrino spectrum given in 5.13. All other nuisance parameters are fixed at their baseline values listed in Table 5.2. The astrophysical neutrino flavor composition is constrained by evaluating the likelihood ratio in a profile likelihood scan, with confidence regions estimated using Wilks's theorem. The expected number of events over 12 years of HESE data, assuming the spectrum in 5.13, is broken down by flux components and shown in Monte Carlo templates in Table **??**. The fitting procedure bins all HESE events above 60 TeV in reconstructed energy and further categorizes them into three subsamples based on morphology: single cascades, tracks, and double cascades. Each sample is fit using 2D Monte Carlo templates, with the appropriate analysis variables shown in Figure 5.2, Figure 5.3, and Figure 5.1.

The sensitivity results in Figure 5.7 reveal that none of the standard source scenarios discussed in 2.2.3 can be rejected with high significance.

Table 5.2: The expected number of events from different flux components for the ~ 12 years of HESE sample, broken down for each individual fluxes, for single cascades, double cascades, and tracks categories. Only Monte Carlo uncertainties are included. The astrophysical spectrum assumed follows Equation **??**

	Single Cascades	Double Cascades	Tracks
Astrophysical	67 ± 1	4 ± 0.2	13 ± 0.5
Conventional	5 ± 0.7	0.2 ± 0.1	5 ± 0.6
Atm. Muons	-	-	2 ± 3
MC Sum	72 ± 2	4 ± 0.3	20 ± 3

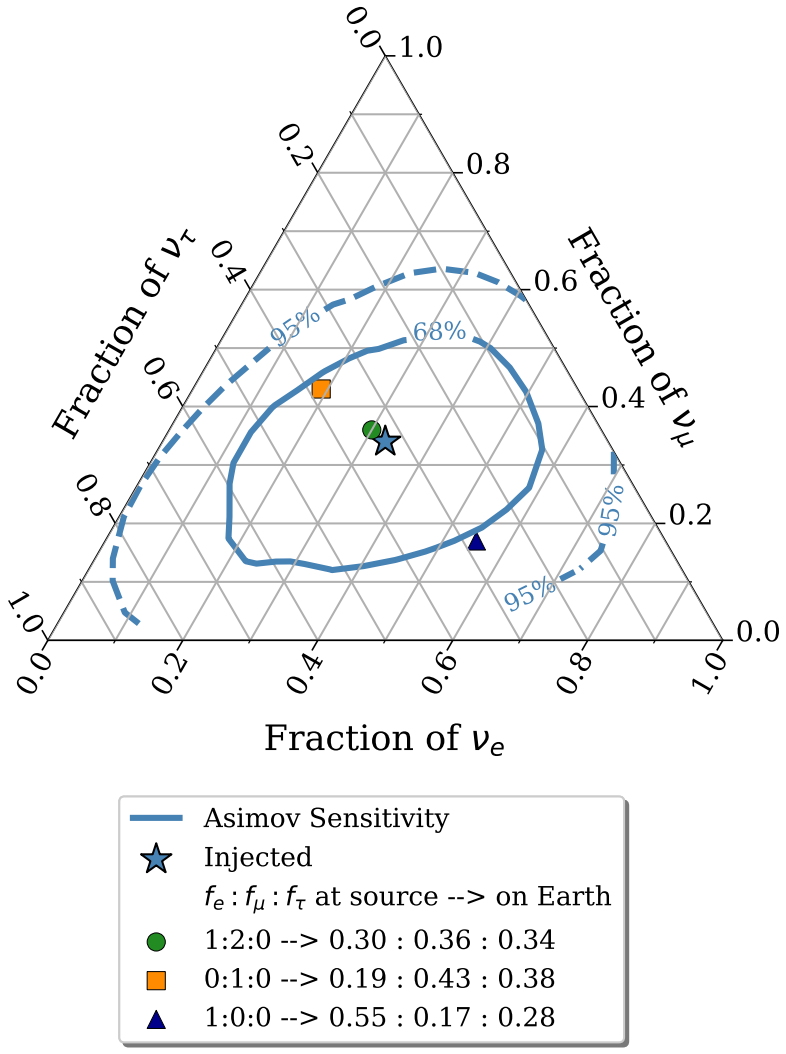

Figure 5.7: Sensitivity of the analysis presented in this thesis to measure the the flavor composition using ~ 12 years of IceCube HESE data assuming single power law given in Equation 5.13, with flavour composition of $\nu_e : \nu_\mu : \nu_\tau = 1 : 1 : 1$. Contours show the 1σ (solid) and 2σ (dashed) confidence intervals assuming Wilks' theorem.

For instance, the neutron beam scenario (represented by the dark blue triangle) is barely excluded at the ~ 1σ level. It is important to recall that the sensitivity of this analysis to the astrophysical tau-neutrino flux depends strongly on the assumed spectral shape of the neutrino flux. This sensitivity arises from the energy-dependent identification efficiency of tau-neutrino interactions. At higher energies, more energy is transferred to the secondary tau, increasing its decay length and enhancing identification efficiency. A softer spectrum, however, leads to more tau-neutrino interactions at lower energies, where they are harder to identify. Additionally, the sudden disappearance of line segments in the 95% confidence contours, particularly in regions where the ν_μ fraction approaches zero, is a result of the flavor fit parameterization (see Equation 5.8). By construction, this fraction cannot be zero, meaning that

this phase space is inaccessible to the fit.

While earlier versions of this analysis explored alternative flux models (or example, a broken power law introduces a break in the conventional single power law, resulting in different spectral indices on either side of the break energy), this was not done here. The decision was based from recent findings from another IceCube analysis that combined two other event samples (Tracks and Cascades), revealing features in the extragalactic astrophysical neutrino spectrum targetting much larger range of Neutrino energies ($\sim$ 10 TeV to $\sim$ 10 PeV) [107]. That study provided evidence of a spectral break at around 24 TeV with more than 4σ significance. The spectrum showed hardness below this break, followed by softening at higher energies, consistent with the softer spectral measurement from HESE-7.5, which targets the higher-energy range. Importantly, this high-statistics analysis, which extends well beyond the energy range of the current analysis, found no significant structures at HESE energies. Furthermore, an independent study using a different event sample [108] reported similar spectral features and closely aligned best-fit values, solidifying the argument even more.

[107]: Naab et al. (2023), *Measurement of the astrophysical diffuse neutrino flux in a combined fit of IceCube's high energy neutrino data*

[108]: Basu et al. (2023), *From PeV to TeV: Astrophysical Neutrinos with Contained Vertices in 10 years of IceCube Data*

Results 6

The 7.5 years of HESE data (2010-2017) was previously used to measure the composition of astrophysical neutrino flavors [105] (in particular to search for ν_τ events) and energy spectrum [93]. This dataset included 102 events, (of which 60 events were above 60 TeV), that passed the HESE selection criteria, as outlined in section 4.2. Two events were identified as Double Cascade candidates using the particle identifier described in section 4.4.

For this iteration, the analysis has undergone significant changes compared to previous versions while maintaining consistent selection criteria and particle identification methods. The most notable difference lies in the ice model, specifically its properties and influence on the reconstruction of tau decay length, detailed in section 3.2. The SPICE-Bfr may have impacts on the overall energy estimates, as the number of photons collected in a given time window have significantly changed in this model of ice depending on the alignment of DOMs with respect to the iceflow axis [67]. Furthermore, the treatment of detector systematics has evolved, utilizing the SnowStorm method (see section 4.1.2) instead of discrete Monte Carlo simulation sets used previously. The update also includes revised reconstruction tables [109] for the maximum likelihood reconstruction method described in section 4.3. Additionally, various corrections have been applied to monte carlo simulations, encompassing reweighting to incorporate corrections due to tau polarization and initial state radiation corrections to the Glashow cross-sections (see section 4.4). Lastly, some of the nuisance parameters and analysis software are also different (see section 5.2). As a first step, the 7.5 years of HESE data were re-unblinded due to these changes.

This chapter presents flavor measurements made using 12 years (11.69 to be exact) of HESE data. It begins by discussing the re-unblinding of 7.5 years of data, followed by results from the 12-year fit, including Data-Monte Carlo agreement and detailed post-unblinding checks. Finally, the flavor measurement results are presented and interpreted in the last sectinons.

[105]: Abbasi et al. (2022), *Detection of astrophysical tau neutrino candidates in IceCube*

[93]: Abbasi et al. (2021), *IceCube high-energy starting event sample: Description and flux characterization with 7.5 years of data*

[67]: Abbasi et al. (2024), *In situ estimation of ice crystal properties at the South Pole using LED calibration data from the IceCube Neutrino Observatory*

[109]: Yuan (2023), *Detecting neutrinos in IceCube with Cherenkov light in the South Pole ice*

6.1 (Re)Unblinding of 7.5 years of HESE Data

The re-unblinding of the HESE-7.5 data provided new insights, revealing that 64 events met the HESE selection criteria, each with a deposited energy exceeding 60 TeV. It included 6 Double Cascade events*, which is a significant increase from the previous analysis that identified only two Double Cascade events. Notably, 4 of the additional events had initially been classified as single cascades. The reclassification was largely driven by the application of the energy asymmetry cut, which proved to be a crucial factor in differentiating between single and double cascades (see

* Unless explicitly specified, all mentioned classifications are by using SPICEBfr, the default icemodel of the analysis presented in this thesis. At some places in this section, specific comparisons are shown using SPICE-3.2.1

section 4.4). A key difference in this re-unblinding was the icemodel used for reconstruction, as mentioned before. Hence, the data was processed using both SPICE-3.2.1 (used in previous iteration) and SPICE-Bfr to make direct comparisons with the previous results. Using SPICE-3.2.1, reunblinded data contained total of 62 HESE events above 60 TeV deposited energy, of which 7 events were classified as Double Cascades. Moreover, of these 6 and 7 observed Double Cascades, using different ice models, only 3 are common, landing 7 new candidate events. Despite the changes in the total number of classified events, the two common Double Cascade events identified in both iterations exhibited nearly identical reconstructed properties, as outlined in Table 6.1 (for SPICE-3.2.1).

should there be a similar table for bfr??

Table 6.1: Comparison of Reconstructed quantities of events classified as Double Cascades upon re-unbling 7.5 years of HESE data using **SPICE-3.2.1 icemodel** with previous results (grey cells). Shown in the table are (from left), MJD (Modified Julian Date), reconstructed length, reconstructed Energy of first (E_1) and second (E_2) cascades, Energy asymmetry (E_A), Energy Confinement (E_C) and classified morphology (as per previous anlaysis) of the event. The two common events, 57134 (*Double Double*) and 56265 (*Big Bird*) have nearly identical reconstructed quantities. The most striking differences here are specifically reconstructed length and the fact that E_1 and E_2 seem to be almost flipped for some events, even though reconstructed directions (zenith and azimuth, not shown in the table) remains almost idnetical. The change in E_1 and E_2 changes the E_A, which is the discrimation cut between single and double cascades.

MJD	Length		E_1		E_2		E_A		E_C		morphology
57677	27 m	37 m	3.1 TeV	128 TeV	148 TeV	4 TeV	-0.96	0.94	1	0.99	Single
57134	16 m	17 m	18 TeV	8.7 TeV	92 TeV	79 TeV	-0.89	-0.80	0.99	0.99	Double
56763	10.2 m	84 m	63 TeV	107 TeV	87 TeV	17 TeV	-0.16	0.72	0.99	0.99	Single
55477	14 m	279 m	70 TeV	184 TeV	84 TeV	67 TeV	-0.09	0.46	0.99	0.98	Single
55800	12 m	20 m	105 TeV	133 TeV	89 TeV	38 TeV	0.08	0.55	1	0.99	Single
56221	12 m	12 m	209 TeV	102 TeV	132 TeV	237 TeV	0.22	-0.4	0.99	0.97	Track
56265	17 m	16 m	0.8 PeV	1.2 PeV	1 PeV	0.6 PeV	-0.08	0.29	0.99	1	Double

No matter what icemodel is used, in reunblinding an excess of double cascade events was observed, suggesting the presence of unnoticed changes not already accounted for. Careful search of each step in the particle identification process revealed a significant change in the reconstruction method from the previous iteration. Notably, this change involved the incorporation of high quantum efficiency Digital Optical Modules (DOMs) from DeepCore. In earlier analyses, these DOMs had been excluded from the reconstruction of high-energy neutrino events, in millipede-based reconstructions outlined in 4.3. The rationale for their exclusion stemmed from the smaller statistical uncertainties of digitized waveforms, in compared to the systematic uncertainties. These systematic uncertainties, which were not well-characterized for individual DOMs, could not be factored into the table-based likelihood fitting method. Nonetheless, due to advancements in simulation, including enhanced reconstruction tables and detector simulations, the analysis presented in this thesis included the DeepCore DOMs, hence the next step was to explore why Monte Carlo predictions had underestimated the number of Double Cascade events.

Figure 6.1 shows the distribution of classified Double Cascade, both with and without the inclusion of DeepCore DOMs. The monte carlo simulations predicts only $\sim$ 2 Double Cascade events, yet the data revealed 6 (7) Double Cascade events using SPICE-Bfr (SPICE-3.2.1) when DeepCore DOMs were included and only 3 (4) when they were excluded. It remains clear that no matter what icemodel is used, the distribution of reconstructed energy and overall expectation remains same irrespective of whether DeepCore DOMs are included or not. This discrepancy pointed

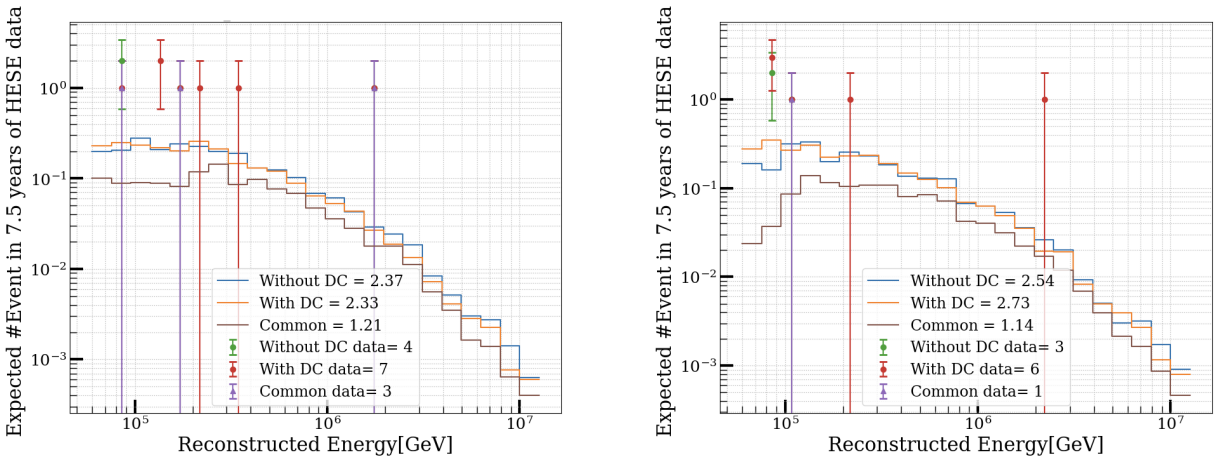

Figure 6.1: Distribution of number of expected classified as double cascacdes in 7.5 years of HESE data usign SPICE-3.2.1 (left) and SPICE-Bfr(right) icemodel with (*With DC*) and without (*Without DC*) DeepCore DOMs, along with data events for the respective configurations.

to potential issues in either the simulation or reconstruction processes involving DeepCore DOMs, indicating that further investigation at the monte carlo level is necessary. Such investigations requires efforts that were beyond the timeline of this thesis work and considering the historical exclusion of DeepCore DOMs (as well as other "bad" DOMs like bright or saturated modules) from reconstruction chains in previous iterations of HESE analyses, this analysis ultimately decided not to include DeepCore DOMs in the full sample unblinding. Ultimately, the re-unblinding of the HESE-7.5 data resulted in 62 events with deposited energies above 60 TeV. Of these, 45 were classified as single cascades, 3 as Double Cascades, and 14 as track events. A detailed comparison between these reunblinded results and previous results, including classified morphologies (with different iterations of icemodels and DeepCore inclusion/exclusion) is shown in Table 6.2.

In one of the appendix, a short discussion about SPE charge distribution checks done with jvs shall be included

Table 6.2: Event classification of 7.5 years of HESE data (Previous) compared with reunblinded sample outcome (all events have Reconstructed total energy > 60 TeV). The comparison is shown for all 2 different icemodels, each of which further broken down into with and without the deepcore doms. The final outcome of this reunblinding, in order to move forward with the full sample is the last column (without DeepCore using SPICEBfr).

Morphology	Previous	Reunblinded			
		SPICE-3.2.1		SPICE-Bfr	
		DeepCore	No DeepCore	DeepCore	No DeepCore
Cascades	41	41	44	42	45
Double Cascades	2	7	4	6	3
Tracks	17	14	14	16	14
Total	60	62	62	64	62

6.2 Unblinding of 12 years of HESE data

The High-Energy Starting Events (HESE) sample, covering approximately 12 years of IceCube detector live time (4268.7 days) from 2010 to August 2022, was unblinded in January 2024 for the analysis outlined in Section 4.3. This sample includes 167 events that passed the HESE selection criteria, which involved the veto and total charge conditions as detailed

in Section 4.2. Of these, 3 were coincident events that had previously been removed by manual inspection, but were retained this time since the current Monte Carlo simulations now account for such coincidences. Despite this, the energy threshold of 60 TeV effectively filtered them out, resulting in a final sample of 97 events above the 60 TeV deposited energy threshold. Using the ternary topology identification method from this thesis, 64 events were classified as single cascades, 5 as double cascades, and 28 as tracks.

6.2.1 Fit results

Blind Fit results

In IceCube, all the analysis are done in a blind fashion, meaning reconstruction and other fit details are applied to simulation to produce expectations in form of Monte Carlo PDFs and later data is fit to this expectation to make the desired measurement. Details of such a fit are given in 5.1. For such fits, before looking at the full data results, sometimes a middle step is considered where only nuisance parameters are revealed first (and/or only background region is looked at) to see any striking disagreement between the data and monte carlo or unexplainable behaviour of any nuisance parameters (e.g. if they are hitting the fit range boundary etc). Stopping criterions are set-up beforehand in case this step shows any troublesome results. For HESE sample, since overall expectation is quite low, looking at a subsample would certainly be unyielding. Thus, blindfit for this analysis included observing the nuisance parameters behaviour and goodness of the fit. The stopping criterions included, minimum p-value of 5% for the goodness of fit test (see 5.1 for details) and applying priors on systematics in case they hit the boundary. These priors are derived from the so far gathered best knowledge of the ice and detector, and were tested by running pseudo trials (see 5.2.2) to test their effects on signal distributions. As a post-unblinding check, they are to be removed to see if any significant changes are observed in signal parameters.

The bestfir values of nuisance parameters are summarized in Table 6.3 along with their gaussian priors. Initially, the holeice parameters, $\eta_{\text{h.ice-p0}}$ and $\eta_{\text{h.ice-p1}}$ were hitting the boundary, but upon applying the tested priors this effect was resolved. As a post unblinding check, these priors were removed to check any changes in signal parameters, no such significant changes were observed. The likelihood includes a penalty term (see 5.1) which was checked for the 2D scan of flavour ratio triangle to see the effect of pulls due to this prior.

perhaps the triangle plot showing llh penalty due to these priors can be shown here? or should this discussion have its separate appendix?

Most of the nuisance parameters are primarily fitted to their priors with minimal deviations from the modeled uncertainties. The detector systematics are set away from default values, although they still remain within one standard deviation of the applied prior width. This can be explained as follows: The method used to apply systematic uncertainties, known as the "gradient method" (see 5.2.1), in the fit assumes linearity whether moving away from or towards the central value. In an ideal scenario, the range within which the parameter is allowed to vary (and the simulation range) should be narrow enough that the central value can always be recovered. However, these parameters are considered only as

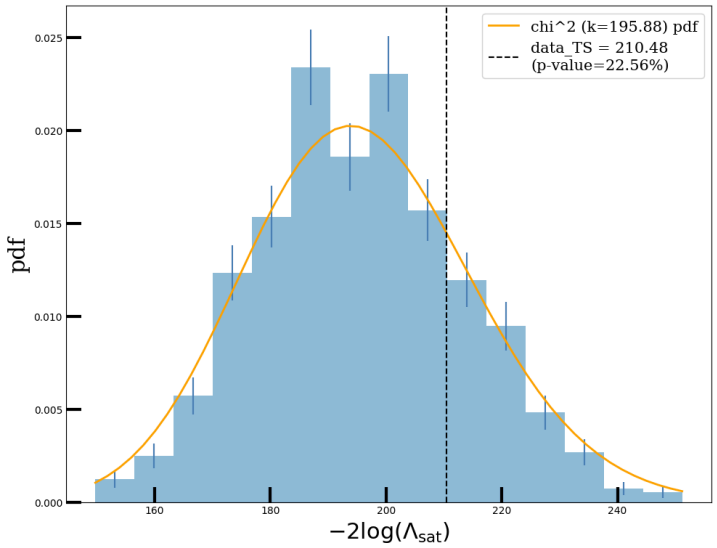

Figure 6.2: Distribution of the test statistics for 1000 pseudotrials injected at best-fit (signal parameters kept blind). Vertical line shows TS of data, which matches quite well with degrees of freedom derived by fitting a χ^2 to the distribution.

nuisance in the fit, and they are not meant to be measured. Furthermore, the detector is not so precisely calibrated as to know the true value of these parameters. Therefore, in practice, the range is kept quite wide. In the analysis presented here, where the overall expectation is low and the data is binned in histograms, such things can happen, causing the nuisance parameters to shift. In order to save computational power, the gradients are calculated once for a given spectrum assumption. If the underlying spectrum of data is far from this assumed spectrum, small changes in these signal parameters can cause larger deviations. Most of these systematics thus ended up having a gaussian prior in the fit, as listed in the Table 6.3.

Lastly, the goodness of the fit (GOF) is tested by using the pseudo data. This data is genereated by injecting the Best Fit Parameter (BFP) values as the true parameters and then fluctuating the expected bin counts to consider MC uncertainty and Poisson fluctuations in the data. A distribution of Test Statistic (TS) values is then observed, which is derived from the ratio of the fitted likelihood to the saturated Poisson likelihood. The saturated likelihood represents the alternative hypothesis, where the data perfectly matches the assumed model. The saturated Poisson likelihood assumes the most ideal scenario, where each analysis bin observes statistically significant data, following a chi-squared distribution with degrees of freedom equal to the difference between the number of analysis bins and the number of free parameters in the fit. However, in reality, not all bins observe data, so some deviations are expected. By comparing the distribution of TS values from these pseudo-data trials to the distribution derived from the real data, a p-value can be calculated. The p-value represents the probability of finding a TS value from the trials that is at least as large as the one from the data fit. Figure 6.2 illustrates this distribution, where the data TS is compared with the distribution of trial TS values. The obtained p-value is 22.56%. Based on this test, it is concluded that the fit result is consistent with the expected outcome from the pseudo-data trials.

Table 6.3: The best-fit parameter values of the nuisance parameters. The uncertainties are calculated at the 68% confidence level through a profile likelihood scan assuming Wilks' theorem, in case of a flat likelihood space, fit boundaries are given as limits. Last column states the gaussian priors on the parameters (if applicable) in terms of the mean (μ) and width (σ). The table is divided in terms of type of the nuisance parameters, above part includes all the parameters that affects the atmosphgeric neutrino components and the lower part consists if parameters stemming through various detector components. For details, see 5.2.1

Parameter		Best-Fit value	Prior (μ, σ)
Φ_{conv}	Conventional Flux normalisation	$0.99^{+0.19}_{-0.2}$	(1.0,0.2)
Φ_{prompt}	Prompt Flux Normalisation	$0.0^{+2.25}_{-0.0}$	-
ξ_{CR}	Interpolation between Cosmic Ray Models	0.042^{+2}_{-1}	(0,1)
$\Delta\gamma_{\text{CR}}$	Cosmic Ray Spectral Index Shift	-0.00^{+1}_{-1}	(0,0.05)
H_{Barr}	Barr-parameter modifying the pion-contribution	$0.0^{+0.5}_{-0.5}$	(0,0.15)
W_{Barr}	Barr-parameter modifying the kaon-contribution	$0.0^{+0.5}_{-0.5}$	(0,0.40)
Y_{Barr}	Barr-parameter modifying the pion-contribution	$0.0^{+0.5}_{-0.5}$	(0,0.30)
Z_{Barr}	Barr-parameter modifying the pion-contribution	$0.0^{+0.5}_{-0.5}$	(0,0.12)
Φ_{muongun}	Muon Flux Normalisation	$1.16^{+0.42}_{-0.43}$	(1,0.5)
I_{scale}	scale factor for Neutrino Nucleon Inelasticity weight	$0.99^{+0.1}_{-0.09}$	(1,0.1)
	Detector Systematics		
η_{domeff}	Optical Efficiency of DOMs	$1.04^{+0.06}_{-0.04}$	(1.0,0.1)
η_{abs}	Ice Absorption Scaling	$0.99^{+0.04}_{-0.04}$	(1.0,0.05)
η_{scat}	Ice Scattering Scaling	$0.98^{+0.04}_{-0.04}$	(1.0,0.05)
$\eta_{\text{h.ice-p0}}$	parametrization for refrozen icecolumn	$-0.27^{+0.28}_{-0.38}$	(-0.27,0.5)
$\eta_{\text{h.ice-p1}}$	parametrization for refrozen icecolumn	$-0.08^{+0.04}_{-0.05}$	(-0.042,0.05)
η_{aniso}	Ice Anisotropy Scaling	$0.99^{+0.54}_{-0.63}$	-

Full fit results

The bestfit values of the signal parameters for the 97 HESE events are summarized in Table 6.4. As explained in 5.2.1, the flavour fractions within `NNMFit` framework are fitted as scaling factors s_{ν_e} and s_{ν_τ}, which modifies the flux of electron and tau neutrinos relative to the muon neutrino flux. Which is why, the signal parameters listed in Table 6.4 needs to be converted to their corresponding flavour fractions (), giving us measured flavoured composition of astrophysical neutrinos as, $\nu_e : \nu_\mu : \nu_\tau = 0.19 : 0.43 : 0.38$. Since the measurement is done for the entire spectrum, this value that of best-fit flavour composition which is expected on earth in case neutrinos at high energy sources are produced with muon damped scenario, hints that diffuse neutrino spectrum at high energies (sensitivity range of this analysis is 100TeV-10PeV) may be dominated by sources with such production mechanisms. Nevertheless, the limits derived (see 6.3) cannot reject either of these scenarios with reasonable significance.

reference fraction conversion formula here

The best-fit value of astrophysical index (γ_{astro}), assuming a single power law is $2.84^{+0.19}_{-0.18}$. This value is in well agreement with the previous results [93]. As for the normalization, as per the formulation of the flavour fit within the `NNMFit` the best-fit value shown in the table is astrophysical ν_μ normalization, which when converted using appropriate transformations

[93]: Abbasi et al. (2021), *IceCube high-energy starting event sample: Description and flux characterization with 7.5 years of data*

Table 6.4: The best-fit parameter values for the signal parameters for a single power-law model at 100 TeV muon neutrino energy for both particle and antiparticle. The uncertainties are calculated at the 68% confidence level through a profile likelihood scan assuming Wilks' theorem.

Parameter		Best-Fit value
ϕ_{ν_μ}	astro. ν_μ normalisation [10^{-18}GeV^{-1}cm^{-2}sr^{-1}s^{-1}]	$2.53^{+1.78}_{-1.49}$
γ_{astro}	astro. spectral index	$2.84^{+0.19}_{-0.18}$
s_{ν_e}	astro. ν_e scaling factor to modify total flux norm ($\Phi^{\text{astro}}_{\nu+\bar{\nu}}$) relative to ϕ_{ν_μ}	$0.45^{+0.68}_{-0.40}$
s_{ν_τ}	astro. ν_τ scaling factor to modify total flux norm ($\Phi^{\text{astro}}_{\nu+\bar{\nu}}$) relative to ϕ_{ν_μ}	$0.896^{+1.34}_{-0.89}$

gives the total flux normalization (for all flavours) $\Phi^{\text{astro}}_{\nu+\bar{\nu}} = 5.94^{+5.64}_{-4.28}$. The larger uncertainity on normalization is expected for such a fit where each flavour components are allowed to be free, that in turn have larger uncertainty on them (see Table 6.4).

check this number again!!

Lastly, the table in Table 6.5 provides the breakdown of expected events classified into specific morphologies and their individual components. Additionally, the comparison includes the expectation based on a $\nu_e : \nu_\mu : \nu_\tau = 1 : 1 : 1$ flavor ratio, which was determined by running the fit with fixed flavor ratios. It is important to note that the expectation aligns more closely with the data when the flavor ratios are independently fitted.

Table 6.5: The expected number of HESE events, classified into three morphologies, assuming a fixed flavour ratio of 1:1:1 and at the best-fit flavour ratio. The total expected event counts are further broken down into each of the flux components, Astrophysical (Astro), Conventional (Conv), Atmospheric Muons (Muon). Prompt component is not shown here as best-fit value of the prompt norm (Φ_{prompt}) is 0.

Reconstructed Morphology	$\nu_e : \nu_\mu : \nu_\tau = 1 : 1 : 1$(fixed)				$\nu_e : \nu_\mu : \nu_\tau = 0.19 : 0.43 : 0.38$ (free)				Data
	Astro	Conv	Muon	Total	Astro	Conv	Muon	Total	
Cascades	58 ± 2	6.8 ± 0.9	-	65 ± 2.7	57 ± 2	6 ± 0.79	-	63.4 ± 2.4	**64**
Tracks	11.8 ± 0.7	6.3 ± 1	2 ± 3	20 ± 3.6	16 ± 0.8	5.7 ± 0.9	1.84 ± 2.7	23.4 ± 3.4	**28**
Double Cascades	3.2 ± 0.3	0.4 ± 0.2	-	3.5 ± 0.5	3.8 ± 0.3	0.3 ± 0.2	-	4.1 ± 0.4	**5**

6.2.2 Data/Monte Carlo Agreement

Even with a reasonably good fit, any significant mismodeling can only be discerned through a comparison with the Monte Carlo expectations. Nonetheless, the subsequent figures demonstrate the distributions of the analysis observables for all three morphologies, for HESE events with deposited energies above 60 TeV. These plots are generated using the best-fit values described in Table 6.4 and Table 6.3. Each figure displays individual components as well as the sum of all components under the label **MC sum**. Additionally, to highlight any noteworthy features, a ratio plot is included for each distribution, illustrating the ratio of data events to each bin of the MC sum. Although there are observed slight fluctuations, the presence of considerable statistical uncertainties makes it challenging to pinpoint any specific spectral features.

Figure 6.3 and Figure 6.4 shows the distribution of reconstructed energy (left) and cosine of reconstructed zenith (right) for events classified as single cascades and tracks resepctively in the 12 years of HESE data. The zenith plot clearly illustrates the all-sky selection feature of the HESE

sample by overall being flat throughout the zenith distribution. It also highlights the decrease of the conventional component in the downgoing region (cos(zenith>0.25)), indicating the self-veto effect. Additionally, the muongun component is exclusively visible in the track histogram due to fact that the ternary classifier predominantly classifies muons as tracks. However, it's important to note that the expectation exhibits substantial statistical uncertainties due to the lack of sufficient `muongun` monte carlo. To mitigate the impact of the noisy distribution caused by extensive Monte Carlo uncertainties, a kernel density estimation (KDE) is employed to smoothen out the fluctuations present. While both morphology distributions reveal some minor structures, they do not demonstrate any statistically significant characteristics.

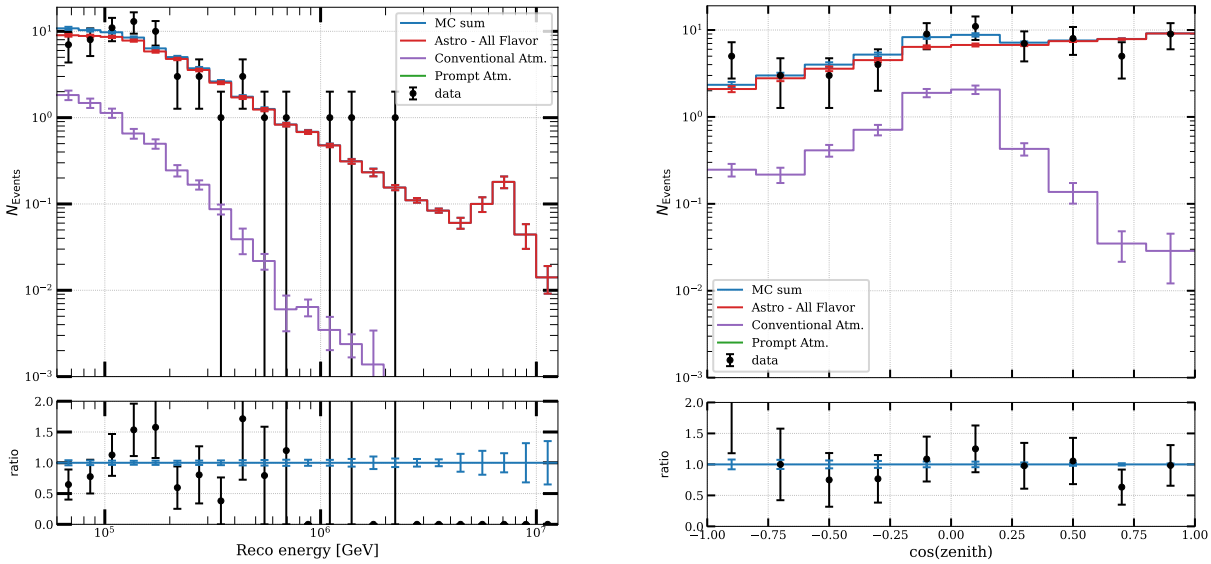

Figure 6.3: Observable distributions of the total deposited energy (left) and the zenith angle (right) for events classified as **single cascades** along with data point positions. Individual components of the fits are produced using bestfit values given in Table 6.4 and Table 6.3 and MC sum is sum of all of these components. Prompt component is missing on account of bestfit value of 0 for the Φ_{prompt}.

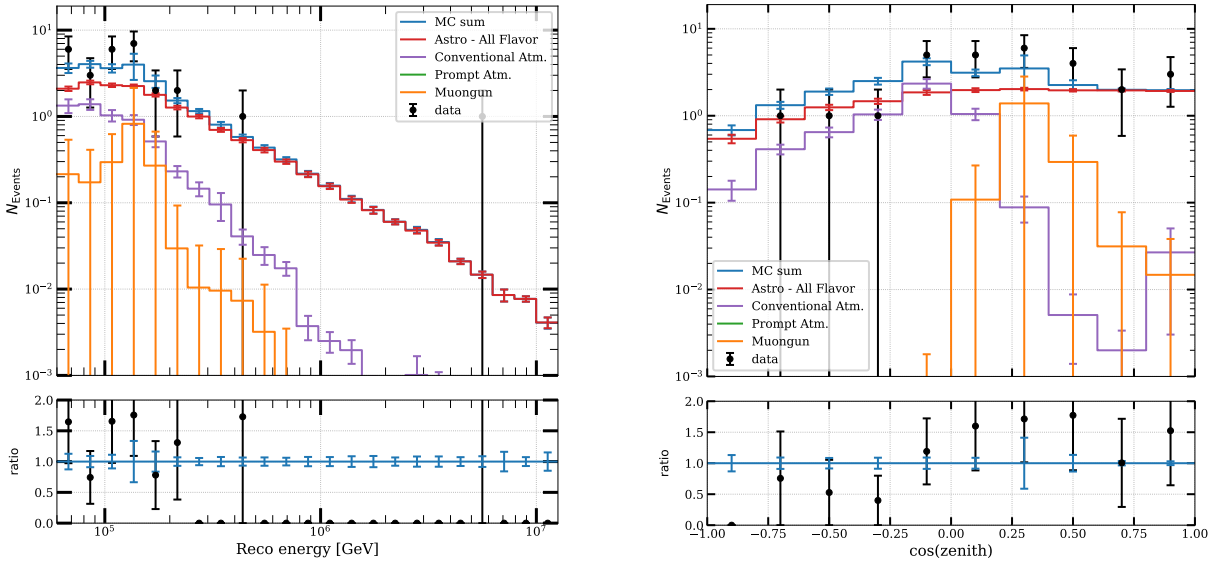

Figure 6.4: Observable distributions of the total deposited energy (left) and the zenith angle (right) for events classified as **tracks** along with data point positions. Individual components of the fits are produced using bestfit values given in Table 6.4 and Table 6.3 and MC sum is sum of all of these components. Prompt component is missing on account of bestfit value of 0 for the Φ_{prompt}.

Figure 6.5 illustrates the distribution of reconstructed energy (left) and reconstructed length (right) for events classified as double cascades in the 12 years of HESE data. In the second energy bin, there is an overfluctuation, but it's challenging to incorporate this as a feature due to the large uncertainties in both the monte carlo and data. An interesting feature of the fit can be seen in the conventional component distribution. The application of gradient correction as an additive factor per component indicates that systematics are trying to adjust this component to account for the excess of double cascades at low energy and high length. This suggests that due to fewer statistics compared to tracks, there is more variability in this parameter across the double cascade bins. Another noteworthy observation is that one event, although close to 100 TeV, has a large length, suggesting that it is a misclassified track. This particular event demonstrates Energy Confinement near the edge (0.97), a cut that is supposed to differentiate between a double cascade and a track, but not quite above the threshold to be a track (0.99). And hence, the event passed all the cuts and ended up being classified as a double cascade. This becomes more evident in 2D distribution of energy and length in Figure 6.6, where this event clearly ends up in a background dominated region of the PDF (see 4.4 for signal and background pdfs of double cascades).

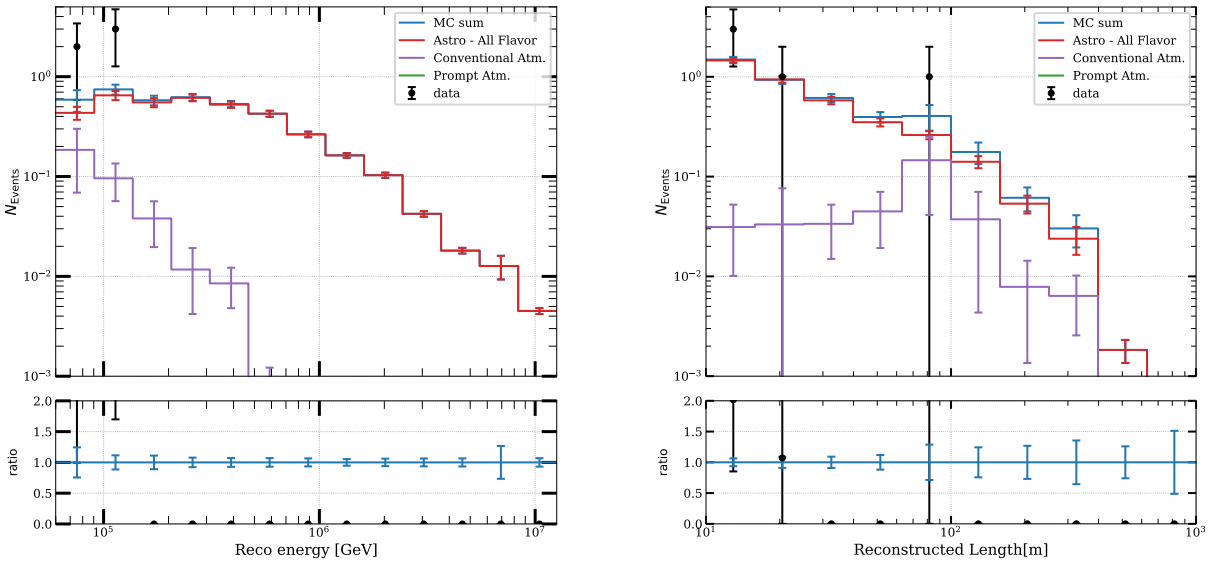

Figure 6.5: Observable distributions of the total deposited energy (left) and the reconstructed length (right) for events classified as **double cascades** along with data point positions. Individual components of the fits are produced using bestfit values given in Table 6.4 and Table 6.3 and MC sum is sum of all of these components. Prompt component is missing on account of bestfit value of 0 for the Φ_{prompt}.

The figure Figure 6.6 illustrates a two-dimensional PID pdf of reconstructed double cascade events, based on the best-fit values described in the tables. The vertical lines demonstrate how quickly the single-cascade background decreases with length. For instance, 68% of misclassified single cascades have reconstructed double-cascade lengths of less than ~ 14 m, 90% have lengths below ~ 20 m, and only 1% have lengths exceeding ~ 25 m. Two of the data events are outside the 68% region, but one of these events is still within the signal region indicated by white lines. The event with a reconstructed length of approximately 95 m but less than 80 TeV energy is clearly in the background region. Another important observation from this figure is the lack of smoothness expected from

PDFs when performing forward folding fits. The gradients are applied as an additive correction per bin, to allow detector systematic variations in the fit. This in turn can significantly change the per bin expectations, making the distributions more fluctuating.

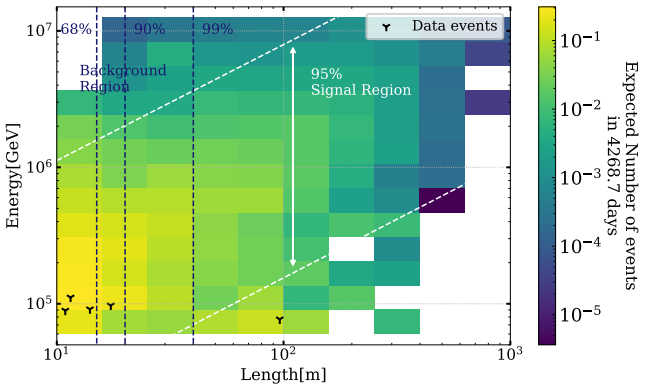

Figure 6.6: Two-dimensional distribution of reconstructed energy vs reconstructed double cascade length of the monte carlo events classified as double cascades. Monte carlo sum is produced using all the bestfit parameters from the Table 6.4 and Table 6.3. Position of the data events are marked with ϒ . Signal (white) and Background (dark blue) dominated regions are marked with their respective percentiles.

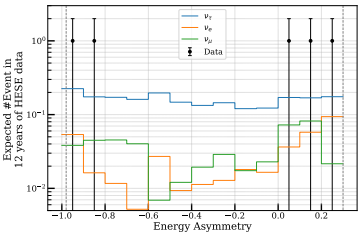

Figure 6.7: Distribution of reconstructed energy asymmetry, defined as $E_A = \frac{E_1 - E_2}{E_1 + E_2}$, (where E_1 and E_2 are energies of first and second cascades, respectively) at best-fit, along with data events. Distribution is shown for all flavours separately, to emphasis domination of ν_τ double cascades in the signal region (verticla grey lines).

Figure 6.7 presents the distribution of the reconstructed energy asymmetry for simulated events in the double-cascade sample, using the best-fit astrophysical and atmospheric spectra. The two vertical lines represent the selection cuts applied to choose the double cascade events, as described in section 4.3. Although two of the 5 events are near the cut edge, they all still fall comfortably within the signal-dominated region of the sample.

6.3 Flavour Composition of Diffuse Astrophysical Neutrinos

The flavor composition of astrophysical neutrinos is measured using 97 high-energy starting event (HESE) events, which are divided among three morphologies. The profile likelihood scans for the flavor scale factors, specifically s_{ν_e} and s_{ν_τ}, are shown in Figure 6.9. The results indicate that the tau scale factor (s_{ν_τ}) is only able to reject the possibility of no ν_τ flux by 1σ ($-2\Delta \log L = 1$), as reflected in the wide contours in the 2D scan shown in Figure 6.8. The 1D scans are used to derive 1σ (68%) confidence regions, shown in Table 6.4. The test statistic $-2\Delta \log L$ compares the global best-fit values of the unconstrained fit to the conditional best-fit values of all remaining model parameters at a fixed scan point. The confidence regions depicted in Figure 6.8 are calculated using Wilk's theorem [88] , as a full Feldman-Cousins construction of the entire flavor composition phase space is computationally demanding (see section 5.1 for details). The agreement of Wilk's theorem is verified by comparing the coverage of the test statistic distribution from Monte Carlo pseudo-experiments to the coverage of a χ^2-distribution. A large fraction of the flavor composition phase space is found to be slightly over-covered, indicating that Wilk's theorem yields a conservative confidence region. Although a part of the 90% confidence region seems to suffer from slight under-coverage, the

[88]: Wilks (1938), *The Large-Sample Distribution of the Likelihood Ratio for Testing Composite Hypotheses*

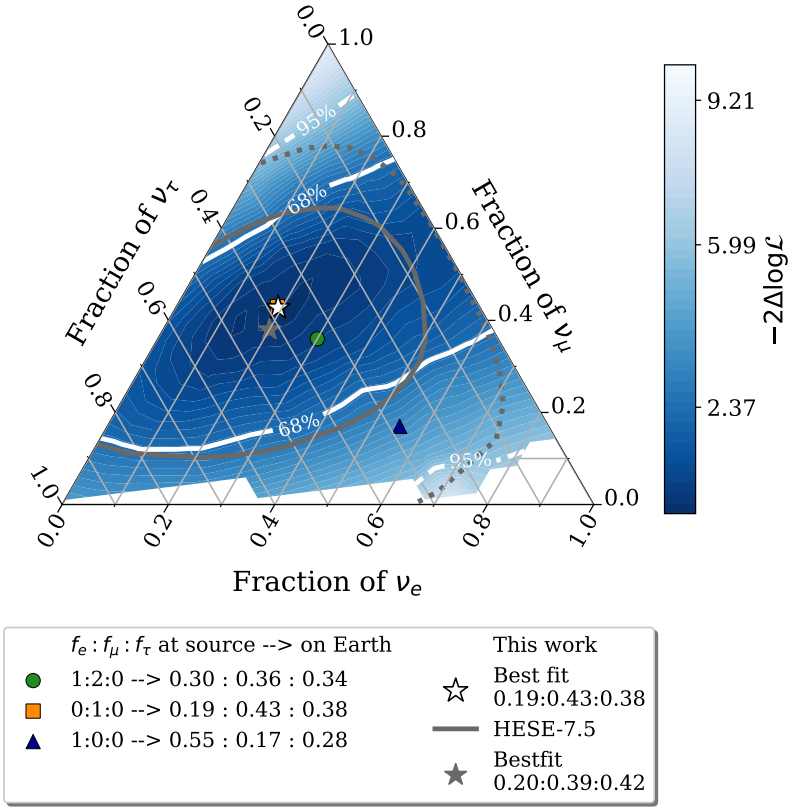

Figure 6.8: A 2 dimensional profile likelihood scan of the astrophysical neutrino flavor composition at Earth using 12 years of HESE data, classified in three event morphologies (see text for details). Each point on the triangle corresponds to a flavor composition of $\nu_e : \nu_\mu : \nu_\tau$ which can be read off the axes along the tick directions specified. The best-fit flavor composition of 0.19 : 0.43 : 0.38 is indicated with a white star. The white solid and dashed lines represent the 68% and 95% confidence regions, respectively, obtained from the χ^2-approximation using Wilk's theorem. Three flavor compositions expected at Earth from different source scenarios are also marked (2.2). The best-fit flavor composition of a previous measurement that used 7.5 years of HESE data is indicated in grey star, with the 68% and 95% confidence regions represented by the grey solid and dotted lines, respectively [105].

χ^2-approximation is deemed sufficient for presenting the measurement result in Figure 6.8.

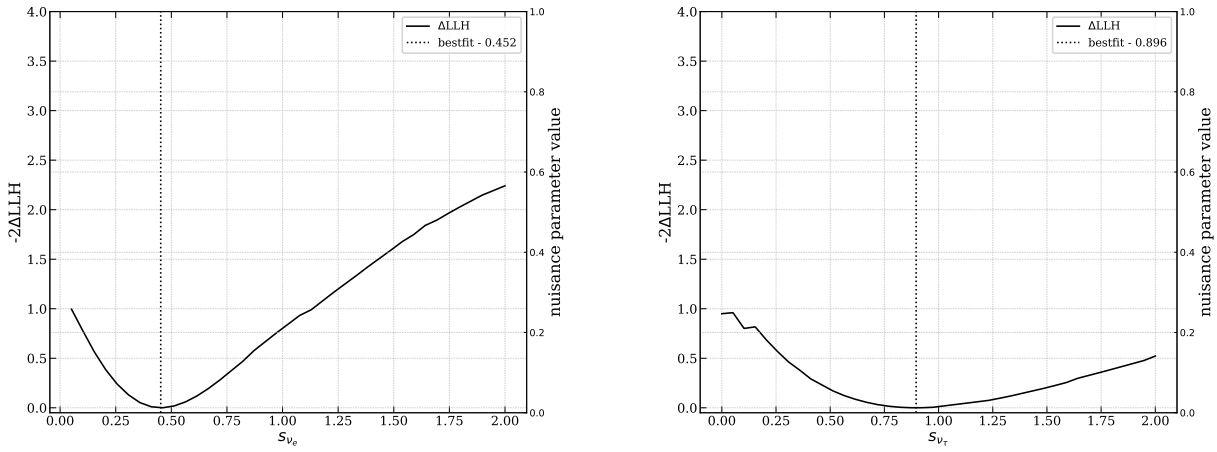

Figure 6.9: 1 dimensional profile likelihood scan of flavour scale factors s_{ν_e} (left) and s_{ν_τ} (right). Solid black line corresponds to the profile likelihood, defined by the likelihood ratio $-2\Delta\log\mathcal{L}$ comparing a fixed value to the best-fit value (denoted by dotted line).

Why are the limits worse than the previous measurements?

The best-fit flavor composition $\nu_e : \nu_\mu : \nu_\tau = 0.19 : 0.43 : 0.38$ aligns well with the previous measurement [105] of $\nu_e : \nu_\mu : \nu_\tau = 0.20 : 0.39 : 0.42$ (grey lines in Figure 6.8). However, with 4 more years of data, which includes more double cascade events, it raises the question of why the limits are not as good. The reason is quite simple, the grey contours are derived using an extended likelihood, based on density

[105]: Abbasi et al. (2022), *Detection of astrophysical tau neutrino candidates in IceCube*

estimates by producing a large number ($\sim 10^6$ events per particle) of resimulations of 2 classified double cascades to assess the **tauness** . A dedicated algorithm (RODEO) was developed and used to compute the density estimate for sparse datasets produced from these resimulations in multiple dimensions (see [102] for details). This updated likelihood can be seen as the unbinned, higher-dimensional version of evaluating the contributions of signal-like and background-like events, which was carried out in a two-dimensional binned way (just as done for the analysis presented in this thesis). Because of this, the limits one should actually compare with the previous measurement should be the one derived using *the non-extended likelihood*, which is the same likelihood and PDF setup used for this iteration of the analysis. Figure 6.10 shows such a comparison. The best-fit flavor composition $\nu_e : \nu_\mu : \nu_\tau = 0.19 : 0.43 : 0.38$ measured using this analysis (black lines) aligns well with the previous measurement of $\nu_e : \nu_\mu : \nu_\tau = 0.29 : 0.43 : 0.28$ (blue lines) using the same likelihood. Although not significantly, the limits derived from this iteration do get better along the ν_μ fraction. Only 68% limits are shown, without the likelihood space to keep the plot easy to read.

[102]: Stachurska (2020), *Astrophysical Tau Neutrinos in IceCube*

tauness

"Tauness" refers to the Bayesian posterior probability that an event is derived from a ν_τ interaction. This can be approximated by analyzing the fraction of events in close proximity to the reconstructed properties of the data events, which are anticipated to result from ν_τ interactions. In essence, tauness provides insight into the probability of each double cascade originating from a ν_τ interaction compared to any other type of interaction.

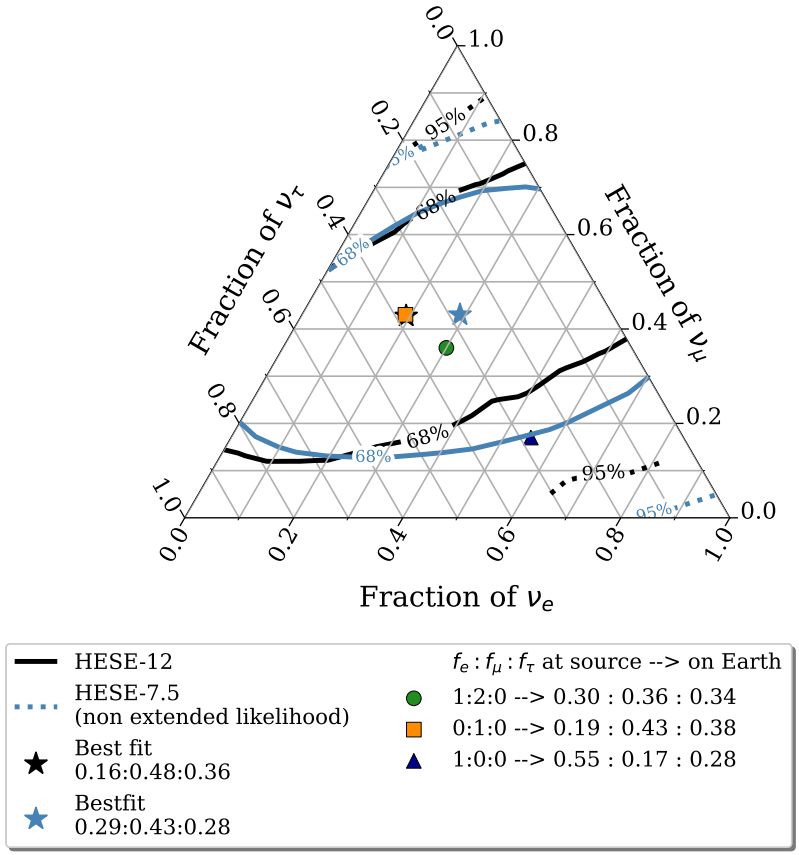

Figure 6.10: The best-fit flavor composition of 0.19 : 0.43 : 0.38 (black), using 12 years of HESE data (this work) compared with the best-fit flavor composition of a previous measurement that used 7.5 years of HESE data [105]. Comparison is shown by usingth esame likelihood formulation (none extended likelihood without resimulations, see text for details). The solid and dashed lines represent the 68% and 95% confidence regions, respectively, obtained from the χ^2-approximation using Wilk's theorem. Three flavor compositions expected at Earth from different source scenarios are also marked (2.2).

Sensitivity at BestFit

Please remember the following text:

The setup and all the relevant updates to the sample and selection chain for the analysis presented in this thesis were done using the best-fit values from the previous analysis. The two signal parameters that affect the flavor measurement, especially the ν_τ fraction and hence the

double cascade events, are the index of the primary neutrino energy spectrum γ_{astro} (assuming a single power law) and the normalization. A harder spectrum (low γ_{astro}) leads to a higher expected flux, resulting in more expected events, while a softer spectrum (high γ_{astro}) leads to a lower flux for samples with a similar effective area. This point was discussed in section 5.3 while discussing the sensitivity of the analysis. The analysis setup and sensitivity were shown using a spectrum with an index of 2.87, which is almost identical to the best-fit value for this analysis (2.84) assuming equal partition of the neutrino flavor ($\nu_e : \nu_\mu : \nu_\tau = 0.33 : 0.33 : 0.33$). Even though the measured flavor ratio is slightly different, the index remains quite close to what the data agrees with, and the estimated sensitivity projected much tighter constraints on 2D flavor measurements, specifically along the ν_τ axis . To understand the lack of improvement to reduce degeneracy along the ν_e/ν_τ axis, the sensitivity of the flavor measurement was first tested at the best fit.

cite sensitivity figure here

The sensitivity of the bestfit analysis is demonstrated in Figure 6.13. It is determined by using an asimov dataset [91] created with the best-fit values of all signal and nuisance parameters from Table 6.4 and Table 6.3. For the sake of simplicity in comparison, a Poisson likelihood was utilized, as SAY likelihood tends to yield more conservative limits (refer to the appendix for some comparisons). The objective here is to examine the most ideal scenario. Moreover, constructing pseudotrials where data is drawn from SAY likelihood is not straightforward, therefore, to maintain consistency in comparisons, all fits depicted in Figure 6.13 are computed using Poisson Likelihood. Consequently, the 68% data limits displayed on the same plot (black line) are narrower compared to those shown in Figure 6.8. Additionally, there is a slight shift in the bestfit point. The key point here is that, given these signal parameters, the analysis is sensitive not only to measure a non-zero ν_τ fraction, but also to reject it with better significance (approximately 3σ as shown in Figure 6.11 - the 1D profile likelihood scan of s_{ν_τ} for the asimov dataset used to derive the 2D limits shown in Figure 6.13). The sensitivity results give rise to three questions:

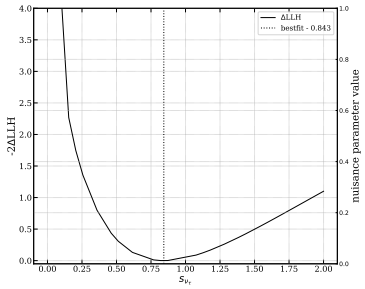

Figure 6.11: 1 dimensional profile likelihood asimov scan of ν_τ scale factor, s_{ν_τ} using **simulation** injected at bestfit point. Solid black line corresponds to the profile likelihood, defined by the likelihood ratio $-2\Delta\log\mathcal{L}$ comparing a fixed value to the best-fit value (denoted by dotted line).

[91]: Cowan et al. (2011), *Asymptotic formulae for likelihood-based tests of new physics*

Are data limits reliable?
The contours shown in Figure 6.8 are based on the assumption that Wilk's theorem holds. This theorem states that the $-2\Delta\log\mathcal{L}$ approximately follows a χ^2-distribution with $k = \text{dof}(\hat{\theta}, \hat{\xi}) - \text{dof}(\theta_t, \xi_t)$, where $\text{dof}(\theta, \xi)$ represents the number of free parameters in the fit. In the case of the flavour fit, there are 2 free parameters - s_{ν_e} and s_{ν_τ}. It is important to note that Wilk's theorem is only valid if the sample size is large and the model parameters are not bounded. However, the HESE sample is relatively small with only a few events passing all selection cuts. Additionally, the available Monte Carlo statistics are not large enough to provide sufficient statistics in every bin of the analysis histograms. Furthermore, the parameters are bounded as the flavour fractions cannot be negative. Therefore, it is essential to verify the validity of Wilk's theorem given these conditions.

Is deriving sensitivity using an asimov dataset a good choice?
The Asimov dataset is a convenient alternative to generating a large number of pseudo trials for testing a specific realization. Computing the test statistic distribution of both conditional and global best-fit values for each point in the triangle is quite expensive. It should not be assumed

that the test statistic value that maximizes the likelihood of the Asimov dataset is always equal to the median of the test statistics derived from the full distribution of various pseudo experiments. Therefore, the next step is to calculate sensitivity using Monte Carlo pseudo experiments.

Is the 2 dimesnional monte carlo PDF ideal for the fit to differentiate between signal and background?

Forward-folding fits, as described in section 5.1, heavily relies on the expected values for each bin of the analysis histograms. It is crucial to choose reliable variables so that the likelihood space looks different for signal and background. For this reason, the analysis variables for double cascade bins are different from those for cascades and tracks. This is because the zenith distribution of astrophysical ν_τ flux shows no significant variation between signal and background. The PDF used in this case was selected due to the correlation of the Tau decay length (L_{dc}) with the energy of the second cascade (E_2) for double cascades resulting from ν_τ-cc interactions, contributing to the population of signal events along this diagonal . The 2D Monte Carlo PDF at best fit, shown in Figure 6.6, contains Monte Carlo events populating the bins along the diagonal. However, the data events are in regions where the background population is expected with nearly equal probability. While drawing data using poisson distribution, fluctuations around the best-fit are considered which in principle should give all possible realisations of the data events ending up in bins with high expectations [1]. Since data events are observed in bins with not so high expectations as well, it may happen that most pseudo trial histograms would end up not replicating data event distributions. Therefore, in addition to the pseudotrials described earlier, the histograms produced for each trial were checked to see how often the events ended up in a region mostly occupied by background-like events.

reference PDFs from the analysis chapter

1: This was also the motivation beg=hind the resimulations that were performed for the previous iteration of the analysis to measure the flavour composition

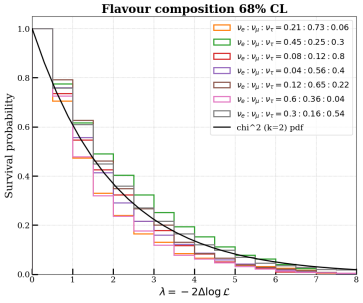

Figure 6.12: Test statistic distribution of the pseudo datasets. All datasets are injected at set of points on 68% contour (solid white line) of Figure 6.8 (also shown in legend). a χ^2-distribution with 2 degrees of freedom is also shown (black line) for refernece.

Both of these tests were conducted and their detailed descriptions are provided in Appendix A. The validity of Wilk's theorem was tested for a few points on the 68% and 95% contours. This was achieved by generating pseudo datasets (500 trials per dataset), each injected with a specific flavor composition (a point on the contour), while keeping the rest of the fit parameters at their best-fit values. Each trial was fitted twice: once by keeping the parameters fixed at the injection point and once with them free. A likelihood ratio test was performed for each trial by taking the ratio of free to fixed likelihood values. The results are represented in a TS distribution shown in Figure A (for points on the 68% line). For comparison, a χ^2-distribution with 2 degrees of freedom is also shown (black line). The TS distribution of some points shows a minor shift from the χ^2 (k=2) case, but nevertheless, shows no significant violation of Wilk's theorem.

The second test was conducted in a similar way, but this time the fixed point for all trials was kept at the data best-fit point. In Figure B, each point denoted with a marker "+" represents the points for which pseudo datasets were generated. Each dataset was generated by injecting the point denoted with "+" and fitted twice: once by keeping s_{ν_e} and s_{ν_τ} fixed at the data best-fit values (from Table 6.4) and once with them free. This was done to test if the true flavor fraction is what the data fit returns and with what confidence the injected point can be rejected. The result is

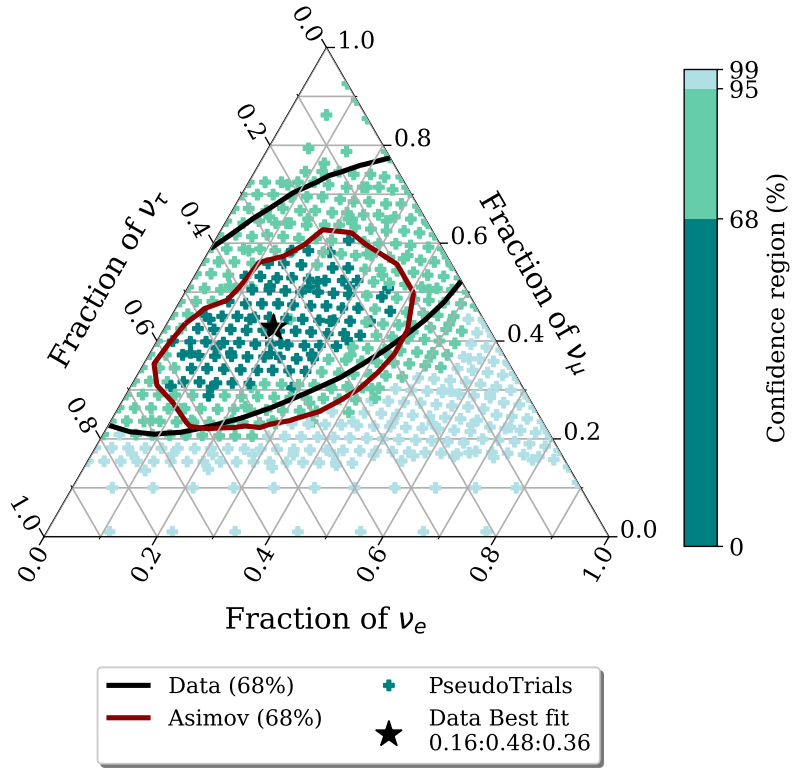

Figure 6.13: Comparison of Measured flavoured ratio (black line) with asimov sensitivity(maroon line) and pseudo trials (marked with '+'). Each + represents a pseudo dataset, drawn from flavour composition of that very point. Colorbar shows confidence intervals of each of these points, to reject the bestfit flavour composition of $\nu_e : \nu_\mu : \nu_\tau = 0.19 : 0.43 : 0.38$. All other parameters of the fit are injected at their bestfit values.

shown in Figure B. The color scheme shows the confidence level each point has to reject the null hypothesis (data best-fit in this case). As can be seen, the pseudo-trial distribution matches quite well with the Asimov sensitivity. In fact, it predicts even tighter constraints compared to the Asimov case, indicating that neither data limits nor Asimov limits are unreliable.

Lastly, the aforementioned third point was checked. Ideally, one would generate pseudo trials until all the Poisson-distributed events fall within the same region of the PDF as shown in Figure 6.6. However, this approach was found to be computationally expensive. For instance, each dataset displayed (around 400) in Figure 6.13 was produced from 500 trials, with each trial fitted twice. On average, each fit took approximately one hour to complete. Therefore, before proceeding, the proportion of PDFs that did not meet the cut criteria was estimated to determine whether using computational resources for further trials was justified. Several tested datasets from different regions of the triangle revealed that, for most datasets, only about 20% of the 500 trials resulted in final histograms with events concentrated in the lower energy bins. There was no feasible way to generate a sufficient number of trials to reduce statistical errors and set definitive limits. As a workaround, only the small proportion of trials that met the necessary criteria were used to generate the TS distributions, allowing an update of the sensitivity shown in Figure 6.13. This updated result is presented in Figure 6.14. As evident from the vanished points, not only were most of the trials excluded, but the confidence intervals also became significantly larger—especially along the ν_τ axis—aligning more closely with the data limits. This concludes why both asimov sensitivity and pseudo trials in Figure 6.13 showed such tight constraints. In an ideal case, one can perform resimulations of

the 5 double cascade events as it was done for the previous iteration, but this would in turn increase computational resources and was beyond the timeline of work presented in this thesis, hence it was not performed.

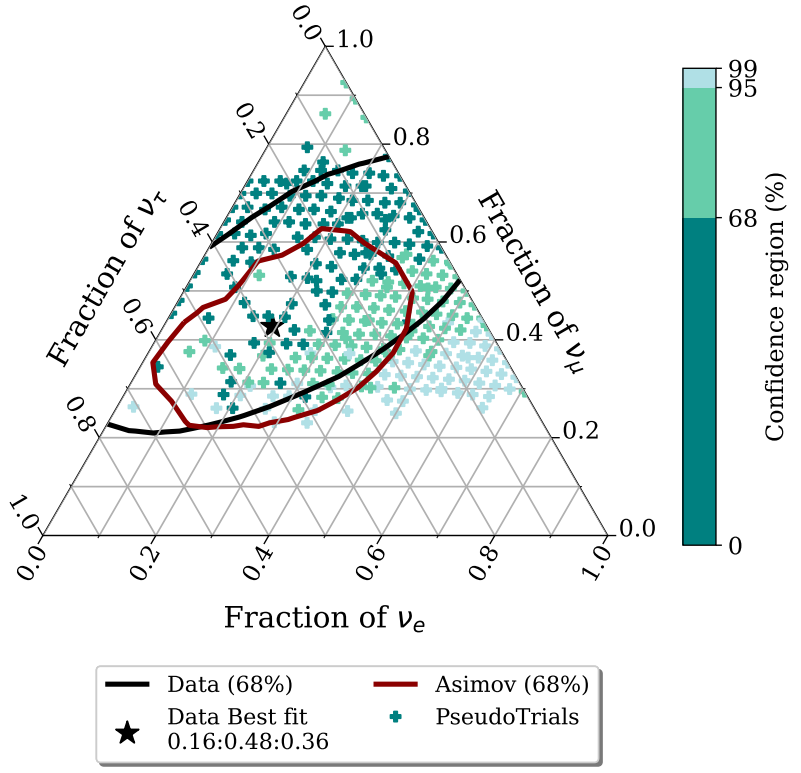

Figure 6.14: Comparison of Measured flavoured ratio (black line) with asimov sensitivity(maroon line) and pseudo trials (marked with '+'). Each + represents a pseudo dataset, drawn from flavour composition of that very point. Colorbar shows confidence intervals of each of these points, to reject the bestfit flavour composition of $\nu_e : \nu_\mu : \nu_\tau = 0.19 : 0.43 : 0.38$. Only trials with final histogram in three lower energy bins are kept in TS distribution. All other parameters of the fit are injected at their bestfit values.

6.4 Discussion

The analysis setup and particle identification methods developed and refined throughout this thesis demonstrate that IceCube is sensitive enough to measure the flavor ratios of the astrophysical neutrino spectrum and set tight constraints. However, more robust techniques, particularly for reconstructing double-cascade events, are needed to produce more reliable Monte Carlo PDFs for these fits. Regarding the measured flavor ratio, as shown in Figure **??**, although the best fit suggests neutrinos are produced by the muon-damped scenario at high-energy sources, no other source scenarios can be excluded with high significance. The neutron beam scenario ($\nu_e : \nu_\mu : \nu_\tau = 1 : 0 : 0$ at the source, evolving to 0.55:0.17:0.28 on Earth) is disfavored by approximately 1σ but remains consistent at 2σ.

A specific measurement of the neutrino energy spectrum was not part of the analysis presented here, as the focus was primarily on flavor measurement, with efforts directed toward improving particle identification. Nonetheless, the HESE sample could also be used to measure, and potentially search for, spectral features. Recent independent studies have discovered a spectral break in the neutrino spectrum at around 30 TeV, softening the spectrum at higher energies, which is within the range of this analysis [107, 110]. This finding offers insight into why

[107]: Naab et al. (2023), *Measurement of the astrophysical diffuse neutrino flux in a combined fit of IceCube's high energy neutrino data*
[110]: Basu et al. (2023), *From PeV to TeV: Astrophysical Neutrinos with Contained Vertices in 10 years of IceCube Data*

previous measurements targeting different energy ranges produced significantly different spectral indices for a single power-law spectrum [93, 97, 111]. Since the HESE sample focuses on high-energy events, where no such spectral features have been observed, and has much lower statistical power than those other samples, no spectral feature searches were attempted during this thesis work.

A less model-dependent approach to describing the astrophysical neutrino flux is the differential unfolding of the energy spectrum. This method divides the flux into energy bins, where each bin is fit independently with a constant $\sim E^{-2}$ spectrum, rather than assuming a continuous power-law across the entire energy range. Ideally, this unfolding would be performed separately for each neutrino flavor to avoid assuming a uniform spectral shape for all flavors. Measuring the flavor composition as a function of energy would also be valuable, as neutrino production processes are energy-dependent. However, due to the limited statistical power of the current dataset, meaningful results could not yet be obtained.

Finally, improvements in reconstruction methods and more data are necessary for future experiments to shed more light on flavor measurements. Double-cascade reconstruction currently has an upper energy limit, as higher-energy events are only partially contained within the detector due to their geometry. In addition, improved detection hardware could provide better information on photon charge and direction, enhancing the overall reconstruction process. These points, along with the potential for a proposed new generation of neutrino detectors, will be discussed in detail in the next chapter.

[93]: Abbasi et al. (2021), *IceCube high-energy starting event sample: Description and flux characterization with 7.5 years of data*
[97]: Abbasi et al. (2022), *Improved Characterization of the Astrophysical Muon–neutrino Flux with 9.5 Years of IceCube Data*
[111]: Aartsen et al. (2020), *Characteristics of the Diffuse Astrophysical Electron and Tau Neutrino Flux with Six Years of IceCube High Energy Cascade Data*

Sensitivity of IceCube-Gen2 to measure flavour composition of Astrophysical Neutrinos

7

This chapter details the sensitivity studies performed for *The IceCube Gen2 detector*. A siginificant portion of this thesis work was dedicated to assess and derive sensitivity to measure the flavour composition of Astrophysical Neutrinos for IceCube Gen2. The detector will be introduced in the following sections, along with the simulations and software framework used to produce the results.

7.1 IceCube Gen2

IceCube-Gen2 is a proposed next generation of neutrino detector, designed to observe the neutrino sky within a wide energy range, from TeV to EeV [112]. Its sensitivity is expected to be at least five times better than IceCube, enabling the observation of individual sources. The instrument layout is designed to detect about ten times more neutrinos annually as compared to IceCube. This increased capability will facilitate in-depth studies of neutrino distribution across the sky, energy spectrum, and flavor composition and beyond standard model physics.

[112]: Aartsen et al. (2021), *IceCube-Gen2: the window to the extreme Universe*

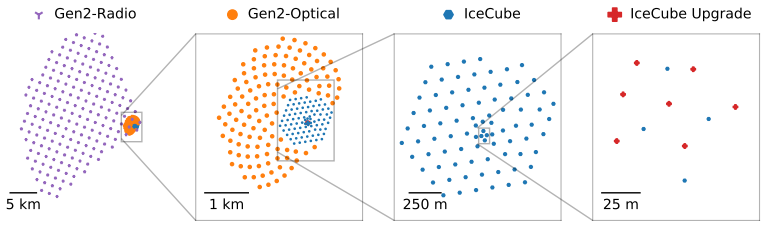

Figure 7.1: Figure depicts the proposed IceCube-Gen2 Neutrino Observatory facility at the South Pole. It includes (from left to right) (i) a radio array with 200 stations, (ii) 120 new in-ice strings, spaced 240 m apart (shown as orange points), as an expansion of (iii) current optical array, (iv) 7 strings of IceCube upgrade, to be deployed soon within currrent in-ice DeepCore volume. Figure taken from [112]

Figure 7.1 illustrates a top view of the IceCube-Gen2 facility, showcasing its various components using optimized technologies for the targeted energy ranges.

The IceCube Upgrade will start deployment this season. Its goal is to lower the detection threshold for neutrinos to 1 GeV (In-line with its predecessor, *DeepCore* in current IceCube)[113]. This improvement will advance oscillation measurements, dark matter searches, and studies of physics beyond the Standard Model. The IceCube Upgrade project will also deploy 693 new types of multi-PMT detector modules, providing an opportunity to test the optical sensor technology for the IceCube-Gen2 observatory.

[113]: Ishihara (2021), *The IceCube Upgrade - Design and Science Goals*

The surface array of IceCube-Gen2 is a unique setup where the surface array measures the electromagnetic shower component and low-energy muons, while the optical array detects TeV and potentially PeV muons from the same air shower [114]. Planned to be used similarly as *IceTop* of IceCube, the stations shall be placed on top of the additional *in-ice* strings of optical array. It can also be used as *surface veto* to reduce the background of atmospheric muons in samples of astrophysical neutrinos from the southern sky.

[114]: IceCube Collaboration et al. (2024), *IceCube-Gen2 Surface Array: Science Case and Plans*

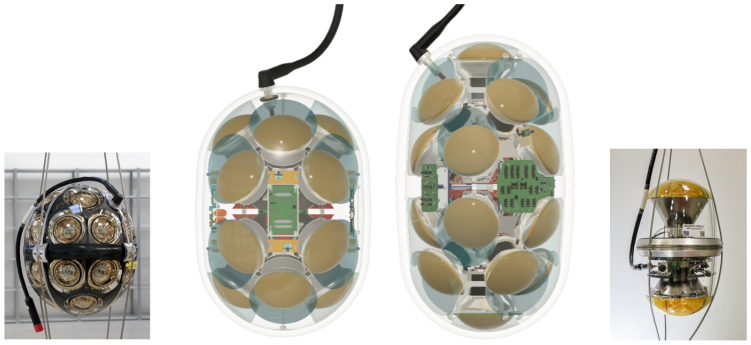

Figure 7.2: The designs of the IceCube-Gen2 optical sensors, DOM-16(second) and DOM-18 (third) with their base designs, to be used in the IceCube Upgrade sensors, are the mDOM on the left and D-Egg on the right [117]

The Radio array aims to discover and characterize high-energy neutrino flux above 10 PeV. It detects nanosecond-scale radio emissions from ultra-high-energy particle showers using the Askaryan effect [115, 116]. This technique is sensitive to energies above PeV and complements the energy range of the optical array by capturing radio emissions from neutral and charged-current interactions, as well as energy losses of secondary leptons.

The optical array The optical array will be expanded with the addition of 120 new strings to the existing IceCube strings. The strings will be arranged in what is referred to as "sunflower geometry," with an average horizontal spacing of 240 meters. The shape of the array and spacing between the strings will be determined through dedicated geometry optimization studies. Each string will contain 80 modules, resulting in a total of 9600 new modules. These modules will be placed between 1325 meters and 2575 meters below the surface, with a vertical spacing of 16 meters. This configuration will create an instrumented geometric volume of 7.9 cubic kilometers. The modules on the string are expected to collect nearly three times the number of photons gathered by an IceCube digital optical module (DOM).

[115]: Askar'yan (1961), *Excess negative charge of an electron-photon shower and its coherent radio emission*
[116]: Meyers et al. (2021), *Radio Detection of EeV Neutrinos in Dielectric Media using the Askaryan Effect* *for Babies*

cite TDR link here? or is whitepaper ok?

For the sensitivity study presented in this thesis, only the optical part of the proposed detector was simulated and used.

7.2 Simulation

To perform this sensitivity study, dedicated simulations were carried out. The study aims not only to assess the sensitivity of IceCube-Gen2 in measuring the flavor composition of astrophysical neutrinos but also to evaluate its capabilities in detecting tau neutrino events, which is a crucial component as described in **??**. The simulations were aligned with the mainline IceCube simulations (detailed in **??**) to enable direct comparisons. However, necessary modifications were made to account for the new-generation optical sensors to be used in IceCube Gen2 and the sparser geometry. The following sections will describe the event samples created using these simulations to conduct the sensitivity analysis.

cite the simulation section here and not the chapter

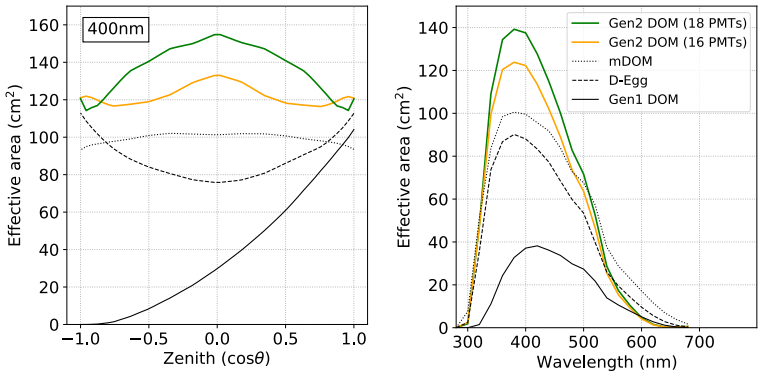

Figure 7.3: The effective area is compared for IceCube-Gen2 DOM candidates, 16, and 18 PMT models, in relation to IceCube-Gen1 DOM (pDOM), D-Egg, and mDOM, as functions of zenith angle (left) and wavelength averaged over solid angle (right). Figure taken from [117]

7.2.1 Isotropic Sensor

The optical sensors to be used in the IceCube-Gen2 project depends a lot on how well the reference optical sensors to be deployed in the IceCube upgrade perform.[117]. The designs have been carefully optimized to balance cost-effectiveness, logistical efficiency, and enhanced performance. Figure 7.2 shows both the 16 and 18 PMT modules, which are being considered to use in IceCube Gen2, along with **mDOM** (*multi PMT Digital Optical Module*) [118, 119] and **D-Egg** (*Dual optical sensors in an Ellipsoid Glass for Gen2*) [120] that are to be deployed in ice for IceCube Upgrade.

[117]: "Abbasi et al. (2023), *The IceCube Gen2 Technical Design Report*

[118]: Classen et al. (2017), *The mDOM - A multi-PMT digital optical module for the IceCube-Gen2 neutrino telescope*

[119]: Classen et al. (2019), *A multi-PMT Optical Module for the IceCube Upgrade*

[120]: Abbasi et al. (2023), *D-Egg: a dual PMT optical module for IceCube*

The maturity of the design, along with extensive in-situ testing using a large number of sensors for the IceCube Upgrade, leads us to consider the mDOM-type sensor as the baseline for evaluating the IceCube Gen2 detector's capabilities in identifying Tau neutrino-induced Double Cascade events. Unlike IceCube's single large 10" PMT, the mDOM consists of 24 smaller 3" PMTs. The key advantages of the mDOM over pDOM [121] are its 2.2 times higher effective photocathode area, omnidirectional sensitivity, and the directional information obtained from the individual "pixels" (the 24 PMTs). Due to the large number of PMTs and their strategic placement within the module sphere, this module offers nearly isotropic angular acceptance, unlike IceCube DOMs with only one downward-facing PMT.

pDOM

pDOM stands for PINGU Digital Optical Module. It was first coined for an R&D upgrade of IceCube DeepCore called **PINGU** (The Precision IceCube Next Generation Upgrade) [121].

[121]: "Aartsen et al. (2014), *Letter of Intent: The Precision IceCube Next Generation Upgrade (PINGU)*

did this project eventually become Upgrade?

The effective area of the optical modules is the equivalent physical cross-section that would detect all the incident photons from a plane perpendicular to a given direction. As illustrated in Figure 7.3 (Left plot) , the mDOM has a nearly linear effective area for collecting photons from all directions, unlike the Gen1 DOMs (pDOMs) which have a downward-facing PMT. As a result, the effective area for pDOMs increases as the arrival direction shifts from 180 degrees ("down-going" in the IceCube coordinate system) to 0 degrees ("up-going" in the IceCube coordinate system).

reproduce this figure, without the right plot

However, current sophisticated methods do not yet provide a full-scale simulation of a multi-PMT module, so a simulated sensor called *iso-pDOM* (isotropic-pDOM) was developed [122]. This sensor can be thought of as a 'spherical PMT' encased in a glass vessel similar to an IceCube DOM but with 2.2 times higher quantum efficiency, capable of capturing photons arriving from all the directions (see Figure 7.4). The sphere was simulated by assuming an upward-facing PMT along with a downward

[122]: Omeliukh (2021), *Optimization of the optical array geometry for IceCube-Gen2*

cite Evangelia's Summer school report?

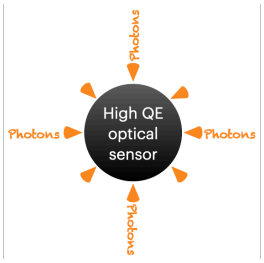

Figure 7.4: Conceptual representation of Simulated sensor with isotropic angular acceptance (iso-pDOM)

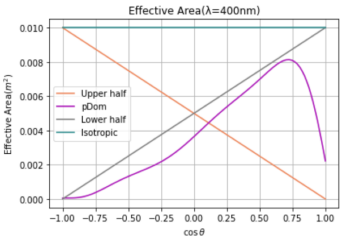

Figure 7.5: Results of simulating a sensor that *mimics* the behaviour of a typical mDOM. The blue line shows changed effective area of the so-called *isopDOM*, achieved by combining acceptance curves of pDOMs having a PMT in "upper" (orange) and "lower" (grey) halves of the DOM respectively

many references from chapter 4 need to be cited correctly in this section

one and combining the results while maintaining the same area under the curves at all wavelengths . The resultant iso-pDOM has an effective area very similar to that of an mDOM.

7.2.2 Event Selection

Monte Carlo events were produced using the so-called isoPDOM for all three flavors of primary neutrinos with energies ranging from 100 TeV to 50 PeV. The simulation chain is identical to that described in **??**. It is important to note that since the IceCube in-ice array is inherently part of the proposed Gen2 detector, all simulated events still include 'hits' from the IC86 configuration. Additionally, during the DetectorSim stage of the simulation chain, where PMT responses, noise, etc., are added, responses are incorporated separately for IceCube DOMs and isoPDOMs. If an event passes all the basic triggers, two separate triggers are stored depending on the event location: IC86 and ICGen2. By default, ICGen2 has a combined response of both detector configurations, while IC86 only contains current IceCube volume events. This feature is crucial as it facilitates direct comparison of events produced with IceCube simulations for IceCube-only analyses.

As discussed in analysis chapter, a fundamental aspect of flavor measurement studies is the ability to identify the flavor of the neutrino involved in an interaction. This identification is possible due to the distinct by-products produced by different neutrino interactions, which result in unique light deposition patterns, or "morphologies" reco chapter. These patterns, illustrated in cite morphology figures, allow us to reconstruct the events by analyzing the morphology of the light deposited in the detector. By doing so, the flavor of the original interacting neutrino can be determined.

To utilize the same particle identifier used in the analysis presented in analysis chapter for this sensitivity study, a dedicated event selection process for high-energy starting events (HESE) was implemented, similar to the approach described in reco chapter. However, since the outer-layer detector veto is specific to the detector geometry and the characteristics of the DOM pulses—which is still under development for the IceCube-Gen2 simulation chain, starting events were selected by examining the interaction vertex of the primary neutrino. This interaction vertex was further refined by considering the deposited charge (measured in single photoelectrons) and calculating the charge-weighted mean positions. This charge information is crucial for applying a HESE-like charge cut. Unlike the 6000 photoelectrons threshold used previously, the threshold for this analysis was set at 2000 photoelectrons. The lower threshold is due to the higher quantum efficiency and isotropic sensitivity of the new sensors, which enhance the detection capability for high-energy events. All the approximations made were in parallel checked for IC86 configuration to reproduce MonteCarlo PDFs within statstical erros to the ones presented in analysis chapter.

Moreover, to appropriately weight the simulated events and account for the probability of an atmospheric neutrino being rejected by an accompanying muon triggering the veto, a dedicated calculation similar to the one used in the HESE-7.5 analysis [93] was used. Additionally,

[93]: Abbasi et al. (2021), *IceCube high-energy starting event sample: Description and flux characterization with 7.5 years of data*

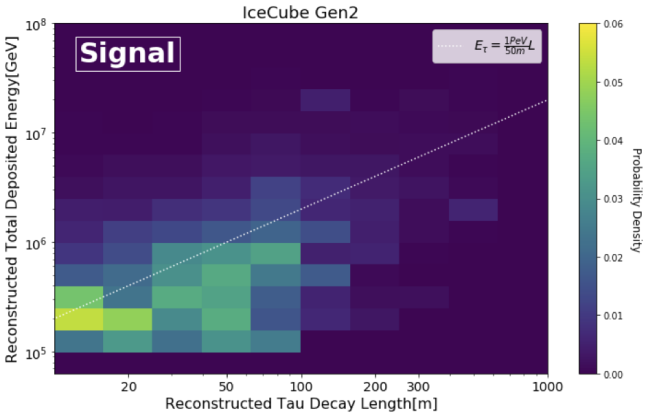

(a) Double Cascades from ν_τ interactions (signal). The signal double cascades show a correlation between (L_{dc}) and (E_{tot}).

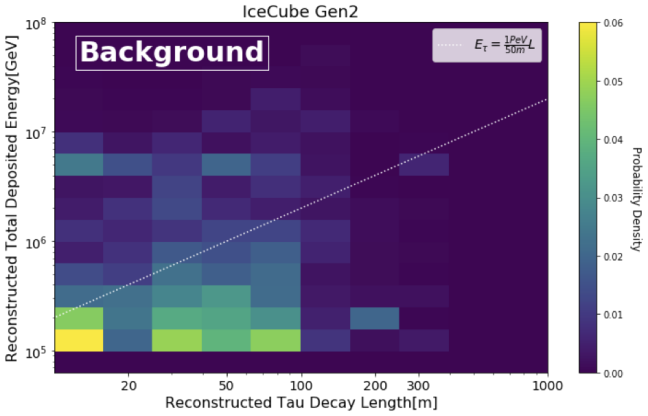

(b) Double Cascades from ν_e and ν_μ interactions (background). The background contributions do not show any correlations, but rather clusters at low L_{dc} and E_{tot}.

Figure 7.6: Total reconstructed energy (E_{tot}) versus reconstructed double cascade length (L_{dc}) for events classified as double cascades.

the reconstructed energy cut, initially set at 60 TeV, was adjusted to 100 TeV. This adjustment was based on the signal-to-background probability density functions (see Figure 7.6a and Figure 7.6b) to ensure a similar signal-to-background ratio (2:1) as achieved in the HESE-7.5 analysis [105] and the HESE-12 analysis (). After applying all the necessary filters, the final sample includes starting events with a reconstructed deposit energy of 100 TeV or more and a charge exceeding 2000 PE. These events originate from interactions of all six types of neutrinos (particle and antiparticle versions of 3 flavors) beginning within the simulated IceCube-Gen2 fiducial volume. They are divided into three categories: Tracks, Single Cascades, and Double Cascades.

[105]: Abbasi et al. (2022), *Detection of astrophysical tau neutrino candidates in IceCube*

cite analysis chapter

7.3 Analysis tool : `toise`

Understanding and enhancing the sensitivity of the detector can result in more precise and dependable performance, thus improving the scientific impact of the experiment. The main goal of the sensitivity studies carried out in this work is to optimize the design of the detector in order to be capable of reconstructing tau neutrino events using existing methods but with a larger detection volume and new generation optical sensors. Additionally, one can also assess the performance of the detector against

[123]: Bustamante et al. (2015), *Theoretically Palatable Flavor Combinations of Astrophysical Neutrinos*

[124]: Coleman et al. (2024), *The flavor composition of ultra-high-energy cosmic neutrinos: measurement forecasts for in-ice radio-based EeV neutrino telescopes*

[125]: Santen et al. (2022), *toise: a framework to describe the performance of high-energy neutrino detectors*

theoretical model [123] by combining both radio and optical arrays of the proposed detector to investigate flavor measurements in the energy ranges from TeV to EeV [124].

It's impractical to run comprehensive simulations for evolving detector designs due to the large amount of computing power required. The `toise` [125] framework was created to estimate sensitivity using a simplified model of the detector response based on targeted Monte Carlo (MC) simulations. This allows for efficient comparisons of different detector designs without repeating the entire simulation process. `toise` was used for a sensitivity study presented in the next section. This section will provide a brief overview of its workflow. In order to distinguish the influence of design choices on detector performance from the intrinsic restrictions imposed by neutrino interaction physics, the event rate calculation in this framework is conducted through two distinct stages: Neutrino Physics and Detection.

In the Physics stage, the neutrino fluxes at the Earth's surface are converted to the detector's area or volume. This involves using a transfer tensor to model the conversion between the initial neutrino flavor states and the observable final states (muons, hadrons, etc.). In addition, various aspects of neutrino interactions, including neutrino-nucleon cross-sections and different interaction types (neutral current or charged current) are also taken into account. The transfer tensor is subsequently combined with the final-state effective area to establish a neutrino effective area. The effective area $A_{\text{eff}}(E, \theta)$ of the detector is calculated by multiplying the geometric area $A_{\text{geo}}(\theta)$ with an energy and zenith-dependent efficiency $\eta(E, \theta)$:

$$A_{\text{eff}}(E, \theta) = A_{\text{geo}}(\theta) \times \eta(E, \theta) \tag{7.1}$$

For the optical array of the proposed IceCube-Gen2, the geometric area is approximately calculated by placing a convex hull around the instrument's geometric boundary. ***The selection efficiency*** $\eta(E, \theta)$ characterizes the detector's triggering efficiency and the probability of an event passing a set of analysis criteria. It is defined as *the ratio of events passing these cuts to the number of events generated*. Depending on the type of sensitivity study being performed—such as expected limits, discovery potential, or flavor measurement—additional parameterizations like energy and angular resolutions and classification efficiency are used. For flavor measurement, ***the classification efficiency*** generates an event classification smearing matrix (Figure **??**) and is defined as *the fraction of topology per energy bin for a given neutrino flavor*. When estimating sensitivities, it is essential to account for backgrounds that may mimic the signal. The framework handles backgrounds by either adding their contributions to the event rate or ignoring regions where they are expected to contribute. For all detectors and science cases, atmospheric neutrino flux is added as a background using the same effective area as for astrophysical neutrinos. Optionally, atmospheric neutrino flux in the downward-going region can be reduced to account for vetoing by accompanying muons from the same air shower.

perhaps a block diagram/-dummy figure to show the whole flow on the side?

more discription will be there in analysis chapter for HESE12, if not, make this more detailed?

7.4 Result of Flavour Sensitivity Measurements

Using the HESE-like sample, described in 7.2.2, a detector response tensor is generated using `toise`. Selection efficiency, detailed in 7.3, is a key factor in generating the detector's neutrino effective area. This efficiency is determined using Figure **??**, which shows the true deposited energy at which the analysis starts to select events. The plot illustrates the ratio of events passing all selection cuts in 7.2.2 to all simulated neutrinos reaching the fiducial volume, per energy bin. The curve is fitted, and the resultant plot shows that neutrinos are selected starting from approximately 200 TeV. This value is used as the selection threshold for events beginning or contained in the fiducial volume.

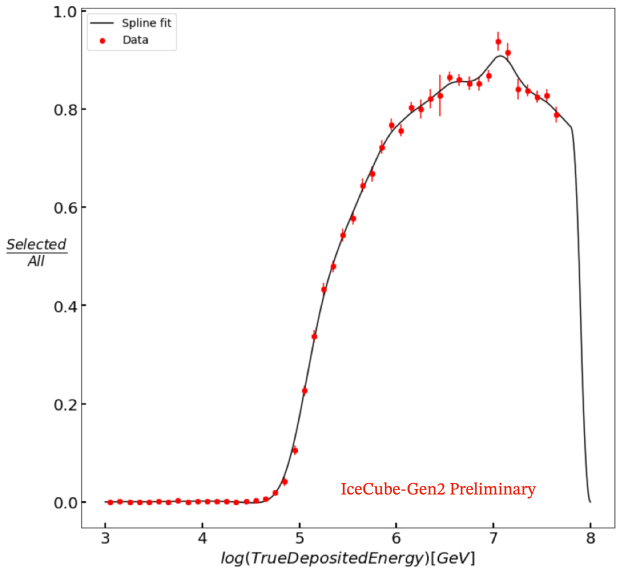

Figure 7.7: Selection Efficiency : Ratio of neutrinos that got classified into a topology to all the neutrinos that interacted in active volume. Data here refers to monte-carlo events per energy bin.

A specific parameterized tensor is used to determine the efficiency of particle identification during flavor measurements. Figure 7.8 shows how well the reconstruction process can identify different types of particles based on their shapes. In an ideal scenario, events involving charged current interactions with electron neutrinos (ν_e) are classified as single cascades, those involving muon neutrinos (ν_μ) as tracks, and those involving tau neutrinos (ν_τ) as double cascades (all neutral current events appear as single cascades, as explained in). The diagonal elements of the plot show how accurate the classifier is, while the off-diagonal elements indicate the fractions of misidentified flavors. The plot shows that as the true deposited energy increases, the number of double cascade events (from ν_τ interactions) initially plateaus and then decreases. This occurs because at higher energies, the individual energy depositions are further apart (due to correlation of L_{dc} and E_{tot}), making it easier for the reconstruction process to distinguish them apart. However, at even higher energies, one of the cascades may be partially or completely outside the detector, causing these events to be misclassified as single cascades due to strict containment criteria (). For single cascades involving ν_e, the efficiency decreases at high energies because some DOMs may become saturated, and their data is excluded from the analysis. In contrast, the efficiency for starting tracks remains relatively consistent across the entire energy range.

chapter 4 section 2

see reco section

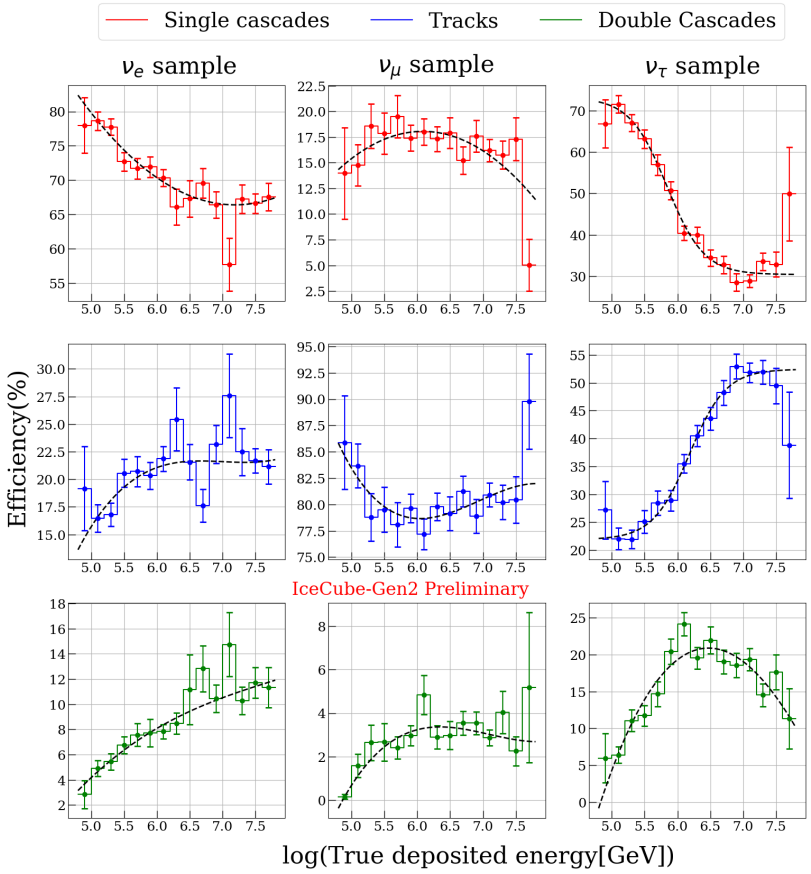

Figure 7.8: Classification Efficiency: Three subplot columns are true neutrino flavors, where each energy bin (true Monte Carlo energy) contains the fraction of topologies, summing to 100%. Diagonal plots show the flavor identification efficiency of the classifier, whereas off-diagonal plots show misidentification fractions.

Lastly, a significant advantage of `toise` is its ability to combine different event selections and detector types. The starting event sample from this detailed study can be combined with the efficiencies of through-going tracks (see Chapter 4). In toise, these efficiencies are included by extrapolating IceCube analysis limits [97] to calculate angular resolutions, PSF, etc. The flavor measurement presented here demonstrates the sensitivity of IceCube Gen2 by combining starting events with through-going muons, a method already realized and updated in IceCube [106].

Figure 7.9 shows the projected flavor measurement sensitivity of IceCube-Gen2 with 10 years of data [126]. The Asimov dataset assumes equal partition of all flavors, with a diffuse neutrino spectrum following a single power-law with an index of 2.5 and a per-flavor normalization of 2.3 [127]. It is worth to note that systematic errors are excluded from this study. Figure 7.10 illustrates the sensitivity change if no dedicated ν_τ identifier is used in the starting event sample, resulting in the sample containing only single cascades and tracks, making it impossible to resolve the ν_e and ν_τ fraction degeneracy.

[97]: Abbasi et al. (2022), *Improved Characterization of the Astrophysical Muon–neutrino Flux with 9.5 Years of IceCube Data*

[106]: Lad et al. (2023), *Summary of IceCube tau neutrino searches and flavor composition measurements of the diffuse astrophysical neutrino flux*

[126]: Lad et al. (2023), *Sensitivity of IceCube-Gen2 to measure flavor composition of Astrophysical neutrinos*

[127]: Aartsen et al. (2015), **title**

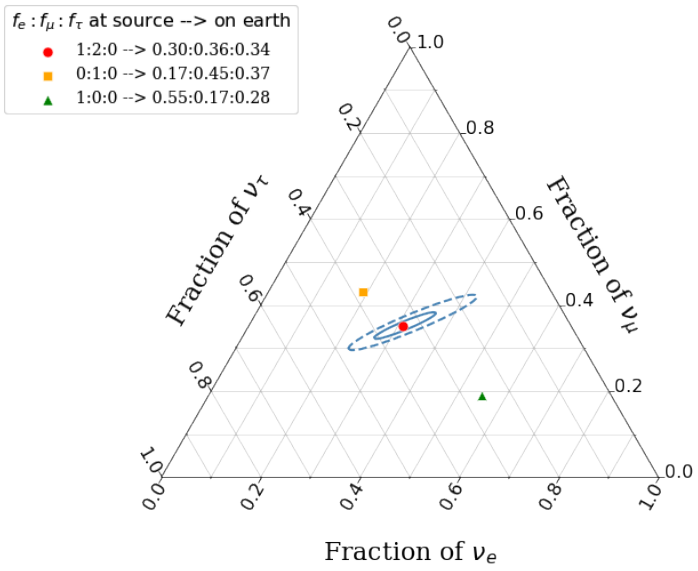

Figure 7.9: Projected sensitivity of IceCube-Gen2 to measure flavor composition of Astrophysical neutrino with 10 years of its lifetime. The dashed (solid) outlines depict the corresponding 99% (68%) constraints.

The sensitivity shown in Figure 7.9 and Figure 7.10 applies to the entire diffuse neutrino spectrum. With this study, flavour measurement for a given 'slice' of energy was also done to see if it has any dependence on it. Diffuse neutrinos originate from various high-energy sources in all directions. Depending on the environments of the acceleration sites (magnetic fields, accretion disks, dust, etc.), the production ratios of neutrinos at the sites may differ . The most commonly assumed model, described in Chapter 1, Section 4, is the pion decay scenario.

add proper citations here

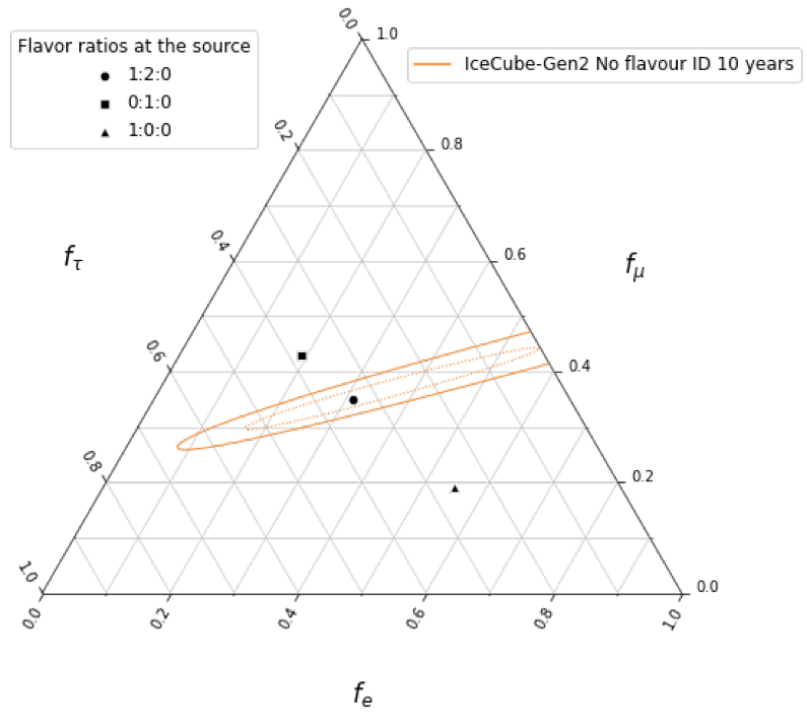

Figure 7.10: Projected sensitivity of IceCube-Gen2 to measure flavor composition of Astrophysical neutrino with 10 years of its lifetime, without a dedicated ν_τ identifier. The dashed (solid) outlines depict the corresponding 99%

combine Figure 7.9 and Figure 7.10 in 1 figure

Above a critical energy, however, the flux of electron neutrinos is suppressed due to strong magnetic fields, leading to muon damping [123] . This changes the neutrino production ratio ($\nu_e : \nu_\mu : \nu_\tau$) from 1:2:0 to 0:1:0. If such sources dominate the overall flux above a certain energy, a

[123]: Bustamante et al. (2015), *Theoretically Palatable Flavor Combinations of Astrophysical Neutrinos*

reference the muon-damped scenario, detailed in Chapter 1, Section 4

transition in measured neutrino flavor fluxes can be observed. Figure 7.11 shows IceCube-Gen2's sensitivity to detecting such a flavor transition. The assumed "critical energy" for this mechanism for the study is 2 PeV. This transition is detectable with IceCube-Gen2 due to its extended energy range, enabled by its approximately eightfold increase in volume [117].

[117]: "Abbasi et al. (2023), *The IceCube Gen2 Technical Design Report*

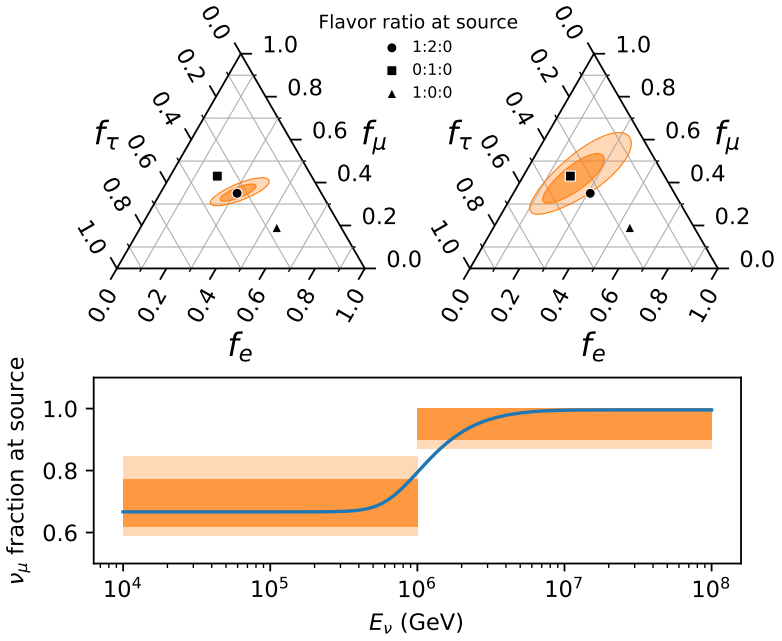

Figure 7.11: The bottom section displays the proportion of ν_μ at the source based on energy, with the assumption that the muon critical energy is 2 PeV. The error bars represent the 68% confidence level limitations on the ν_μ fraction below and above 1 PeV, derived from the observed flavor composition of ν_μ at Earth using IceCube-Gen2 and assuming standard oscillations. In the upper sections, the dark (light) shaded regions depict the corresponding 68% (99%) constraints, without making any assumptions about the mixing matrix.

8 Summary and Outlook

Appendix

List of Figures

List of Tables

Bibliography

Here are the references in citation order.

[1] W. Pauli. "Dear radioactive ladies and gentlemen". In: *Phys. Today* 31N9 (1978), p. 27 (cited on page 1).

[2] F. Reines et al. "Detection of the Free Antineutrino". In: *Phys. Rev.* 117 (1 Jan. 1960), pp. 159–173. DOI: 10.1103/PhysRev.117.159 (cited on page 1).

[3] R. Davis, D. S. Harmer, and K. C. Hoffman. "Search for Neutrinos from the Sun". In: *Phys. Rev. Lett.* 20 (21 1968), pp. 1205–1209. DOI: 10.1103/PhysRevLett.20.1205 (cited on page 1).

[4] H. A. Bethe. "Energy Production in Stars". In: *Phys. Rev.* 55 (5 1939), pp. 434–456. DOI: 10.1103/PhysRev.55.434 (cited on page 1).

[5] Q. R. Ahmad et al. "Measurement of the Rate $\nu_e + d \rightarrow p + p + e^-$ Solar Neutrinos at the Sudbury Neutrino Observatory". In: *Physical Review Letters* 87.7 (2001). DOI: 10.1103/physrevlett.87.071301 (cited on page 1).

[6] Y. Fukuda et al. "Evidence for Oscillation of Atmospheric Neutrinos". In: *Phys. Rev. Lett.* 81 (8 1998), pp. 1562–1567. DOI: 10.1103/PhysRevLett.81.1562 (cited on page 1).

[7] C. S. Wu et al. "Experimental Test of Parity Conservation in Beta Decay". In: *Phys. Rev.* 105 (4 Feb. 1957), pp. 1413–1415. DOI: 10.1103/PhysRev.105.1413 (cited on page 2).

[8] M. Aker et al. "Direct neutrino-mass measurement with sub-electronvolt sensitivity". In: *Nature Phys.* 18.2 (2022), pp. 160–166. DOI: 10.1038/s41567-021-01463-1 (cited on page 2).

[9] N. Aghanim et al. "Planck 2018 results". In: *Astronomy Astrophysics* 641 (2020), A6. DOI: 10.1051/0004-6361/201833910 (cited on page 2).

[10] B. Pontecorvo. "Neutrino Experiments and the Problem of Conservation of Leptonic Charge". In: *Zh. Eksp. Teor. Fiz.* 53 (1967), pp. 1717–1725 (cited on page 2).

[11] S. Schael et al. "Precision electroweak measurements on the Z resonance". In: *Phys. Rept.* 427 (2006), pp. 257–454. DOI: 10.1016/j.physrep.2005.12.006 (cited on pages 2, 9).

[12] R. Abbasi et al. "Measurement of atmospheric neutrino mixing with improved IceCube DeepCore calibration and data processing". In: *Phys. Rev. D* 108.1 (2023), p. 012014. DOI: 10.1103/PhysRevD.108.012014 (cited on page 3).

[13] I. Esteban et al. "The fate of hints: updated global analysis of three-flavor neutrino oscillations". In: *JHEP* 09 (2020), p. 178. DOI: 10.1007/JHEP09(2020)178 (cited on page 3).

[14] I. Gil-Botella. "Neutrino Physics". In: *6th CERN-Latin-American School of High-Energy Physics*. 2013, pp. 157–205. DOI: 10.5170/CERN-2013-003.157 (cited on page 3).

[15] L. Wolfenstein. "Neutrino oscillations in matter". In: *Phys. Rev. D* 17 (9 May 1978), pp. 2369–2374. DOI: 10.1103/PhysRevD.17.2369 (cited on page 4).

[16] L. Wolfenstein. "Neutrino oscillations and stellar collapse". In: *Phys. Rev. D* 20 (10 Nov. 1979), pp. 2634–2635. DOI: 10.1103/PhysRevD.20.2634 (cited on page 4).

[17] S. P. Mikheyev and A. Y. Smirnov. "Resonance Amplification of Oscillations in Matter and Spectroscopy of Solar Neutrinos". In: *Sov. J. Nucl. Phys.* 42 (1985), pp. 913–917 (cited on page 4).

[18] H. A. Bethe. "Possible Explanation of the Solar-Neutrino Puzzle". In: *Phys. Rev. Lett.* 56 (12 Mar. 1986), pp. 1305–1308. DOI: 10.1103/PhysRevLett.56.1305 (cited on page 5).

[19] S. P. Rosen and J. M. Gelb. "Mikheyev-Smirnov-Wolfenstein enhancement of oscillations as a possible solution to the solar-neutrino problem". In: *Phys. Rev. D* 34 (4 Aug. 1986), pp. 969–979. DOI: 10.1103/PhysRevD.34.969 (cited on page 5).

[20] S. Navas et al. "Review of Particle Physics". In: *Phys. Rev. D* 110 (3 Aug. 2024), p. 030001. DOI: 10.1103/PhysRevD.110.030001 (cited on pages 5, 20–23, 25).

[21] J. A. Formaggio and G. P. Zeller. "From eV to EeV: Neutrino Cross Sections Across Energy Scales". In: *Rev. Mod. Phys.* 84 (2012), pp. 1307–1341. DOI: 10.1103/RevModPhys.84.1307 (cited on pages 5, 6, 8).

[22] A. Gando et al. "Constraints on θ_{13} from A Three-Flavor Oscillation Analysis of Reactor Antineutrinos at KamLAND". In: *Phys. Rev. D* 83 (2011), p. 052002. DOI: 10.1103/PhysRevD.83.052002 (cited on page 6).

[23] F. P. An et al. "Measurement of electron antineutrino oscillation based on 1230 days of operation of the Daya Bay experiment". In: *Phys. Rev. D* 95.7 (2017), p. 072006. DOI: 10.1103/PhysRevD.95.072006 (cited on page 6).

[24] R. P. Feynman. "Very High-Energy Collisions of Hadrons". In: *Phys. Rev. Lett.* 23 (24 Dec. 1969), pp. 1415–1417. DOI: 10.1103/PhysRevLett.23.1415 (cited on page 6).

[25] J. Stasielak et al. "High-Energy Neutrino Astronomy—Baikal-GVD Neutrino Telescope in Lake Baikal". In: *Symmetry* 13.3 (2021). DOI: 10.3390/sym13030377 (cited on page 7).

[26] J. D. Bjorken. "Asymptotic Sum Rules at Infinite Momentum". In: *Phys. Rev.* 179 (5 Mar. 1969), pp. 1547–1553. DOI: 10.1103/PhysRev.179.1547 (cited on page 7).

[27] R. Gandhi et al. "Neutrino interactions at ultrahigh energies". In: *Physical Review D* 58.9 (Sept. 1998). DOI: 10.1103/physrevd.58.093009 (cited on page 7).

[28] A. Cooper-Sarkar, P. Mertsch, and S. Sarkar. "The high energy neutrino cross-section in the Standard Model and its uncertainty". In: *JHEP* 08 (2011), p. 042. DOI: 10.1007/JHEP08(2011)042 (cited on pages 8, 37).

[29] P. L. R. Weigel, J. M. Conrad, and A. Garcia-Soto. "Cross Sections and Inelasticity Distributions of High-Energy Neutrino Deep Inelastic Scattering". In: (Aug. 2024) (cited on page 8).

[30] K. Xie et al. "High-energy neutrino deep inelastic scattering cross sections". In: *Phys. Rev. D* 109 (11 June 2024), p. 113001. DOI: 10.1103/PhysRevD.109.113001 (cited on page 8).

[31] M. G. Aartsen et al. "Measurement of the multi-TeV neutrino cross section with IceCube using Earth absorption". In: *Nature* 551 (2017), pp. 596–600. DOI: 10.1038/nature24459 (cited on page 8).

[32] R. Abbasi et al. "Measurement of the high-energy all-flavor neutrino-nucleon cross section with IceCube". In: *Phys. Rev. D* 104 (2 July 2021), p. 022001. DOI: 10.1103/PhysRevD.104.022001 (cited on page 8).

[33] S. L. Glashow. "Resonant Scattering of Antineutrinos". In: *Phys. Rev.* 118 (1 Apr. 1960), pp. 316–317. DOI: 10.1103/PhysRev.118.316 (cited on page 8).

[34] M. G. Aartsen et al. "Detection of a particle shower at the Glashow resonance with IceCube". In: *Nature* 591.7849 (Mar. 2021), pp. 220–224. DOI: 10.1038/s41586-021-03256-1 (cited on page 8).

[35] M. G. Aartsen et al. "Measurements using the inelasticity distribution of multi-TeV neutrino interactions in IceCube". In: *Phys. Rev. D* 99.3 (2019), p. 032004. DOI: 10.1103/PhysRevD.99.032004 (cited on pages 8, 9, 37).

[36] S. R. Elliott, V. Gavrin, and W. Haxton. "The gallium anomaly". In: *Prog. Part. Nucl. Phys.* 134 (2024), p. 104082. DOI: 10.1016/j.ppnp.2023.104082 (cited on page 9).

[37] A. Aguilar et al. "Evidence for neutrino oscillations from the observation of $\bar{\nu}_e$ appearance in a $\bar{\nu}_\mu$ beam". In: *Phys. Rev. D* 64 (2001), p. 112007. DOI: 10.1103/PhysRevD.64.112007 (cited on page 9).

[38] A. A. Aguilar-Arevalo et al. "Improved Search for $\bar{\nu}_\mu \to \bar{\nu}_e$ Oscillations in the MiniBooNE Experiment". In: *Phys. Rev. Lett.* 110 (2013), p. 161801. DOI: 10.1103/PhysRevLett.110.161801 (cited on page 9).

[39] G. Mention et al. "The Reactor Antineutrino Anomaly". In: *Phys. Rev. D* 83 (2011), p. 073006. DOI: 10.1103/PhysRevD.83.073006 (cited on page 9).

[40] K. N. Abazajian et al. "Light Sterile Neutrinos: A White Paper". In: (Apr. 2012) (cited on page 9).

[41] K. N. Abazajian. "Sterile neutrinos in cosmology". In: *Phys. Rept.* 711-712 (2017), pp. 1–28. DOI: 10.1016/j.physrep.2017.10.003 (cited on page 9).

[42] E. Komatsu et al. "SEVEN-YEARWILKINSON MICROWAVE ANISOTROPY PROBE(WMAP) OBSERVATIONS: COSMOLOGICAL INTERPRETATION". In: *The Astrophysical Journal Supplement Series* 192.2 (2011). DOI: 10.1088/0067-0049/192/2/18 (cited on page 9).

[43] N. Aghanim et al. "Planck 2018 results. VI. Cosmological parameters". In: *Astron. Astrophys.* 641 (2020). [Erratum: Astron.Astrophys. 652, C4 (2021)], A6. DOI: 10.1051/0004-6361/201833910 (cited on page 10).

[44] M. Drewes et al. "A White Paper on keV Sterile Neutrino Dark Matter". In: *JCAP* 01 (2017), p. 025. DOI: 10.1088/1475-7516/2017/01/025 (cited on page 10).

[45] P. F. de Salas, R. A. Lineros, and M. Tórtola. "Neutrino propagation in the galactic dark matter halo". In: *Phys. Rev. D* 94.12 (2016), p. 123001. DOI: 10.1103/PhysRevD.94.123001 (cited on page 10).

[46] D. Hooper, D. Morgan, and E. Winstanley. "Lorentz and CPT invariance violation in high-energy neutrinos". In: *Phys. Rev. D* 72 (2005), p. 065009. DOI: 10.1103/PhysRevD.72.065009 (cited on page 10).

[47] A. Trettin. "Search for eV-scale sterile neutrinos with IceCube DeepCore". PhD thesis. Humboldt-Universität zu Berlin, Mathematisch-Naturwissenschaftliche Fakultät, 2024. DOI: http://dx.doi.org/10.18452/27595 (cited on page 10).

[48] L. Fischer. "First Search for Heavy Neutral Leptons with IceCube DeepCore". PhD thesis. Humboldt-Universität zu Berlin, Mathematisch-Naturwissenschaftliche Fakultät, 2024. DOI: http://dx.doi.org/10.18452/29182 (cited on page 10).

[49] R. Abbasi et al. "Search for neutrino lines from dark matter annihilation and decay with IceCube". In: *Phys. Rev. D* 108.10 (2023), p. 102004. DOI: 10.1103/PhysRevD.108.102004 (cited on page 10).

[50] R. W. Rasmussen et al. "Astrophysical neutrinos flavored with beyond the Standard Model physics". In: 96.8, 083018 (Oct. 2017), p. 083018. DOI: 10.1103/PhysRevD.96.083018 (cited on page 10).

[51] M. A. Markov. "On high energy neutrino physics". In: *10th International Conference on High Energy Physics*. 1960, pp. 578–581 (cited on page 13).

[52] J. Babson et al. "Cosmic-ray muons in the deep ocean". In: *Phys. Rev. D* 42 (11 Dec. 1990), pp. 3613–3620. DOI: 10.1103/PhysRevD.42.3613 (cited on page 13).

[53] I. Belolaptikov et al. "The Baikal underwater neutrino telescope: Design, performance, and first results". In: *Astroparticle Physics* 7.3 (1997), pp. 263–282. DOI: https://doi.org/10.1016/S0927-6505(97)00022-4 (cited on page 13).

[54] E. Andres et al. "The AMANDA neutrino telescope: principle of operation and first results". In: *Astroparticle Physics* 13.1 (2000), pp. 1–20. DOI: https://doi.org/10.1016/S0927-6505(99)00092-4 (cited on page 13).

[55] M. Ageron et al. "ANTARES: The first undersea neutrino telescope". In: *Nuclear Instruments and Methods in Physics Research Section A: Accelerators, Spectrometers, Detectors and Associated Equipment* 656.1 (2011), pp. 11–38. DOI: https://doi.org/10.1016/j.nima.2011.06.103 (cited on page 13).

[56] A. Margiotta. "The KM3NeT deep-sea neutrino telescope". In: *Nuclear Instruments and Methods in Physics Research Section A: Accelerators, Spectrometers, Detectors and Associated Equipment* 766 (2014). RICH2013 Proceedings of the Eighth International Workshop on Ring Imaging Cherenkov Detectors Shonan, Kanagawa, Japan, December 2-6, 2013, pp. 83–87 (cited on page 13).

[57] M. G. Aartsen et al. "The IceCube Neutrino Observatory: instrumentation and online systems". In: *Journal of Instrumentation* 12.03 (Mar. 2017), P03012–P03012. DOI: 10.1088/1748-0221/12/03/p03012 (cited on pages 14–16).

[58] R. Abbasi et al. "The design and performance of IceCube DeepCore". In: *Astroparticle Physics* 35.10 (2012), pp. 615–624. DOI: 10.1016/j.astropartphys.2012.01.004 (cited on page 14).

[59] M. G. Aartsen et al. "Measurement of atmospheric tau neutrino appearance with IceCube DeepCore". In: *Physical Review D* 99.3 (2019). DOI: 10.1103/physrevd.99.032007 (cited on page 14).

[60] R. Abbasi et al. “Search for GeV-scale dark matter annihilation in the Sun with IceCube DeepCore”. In: *Physical Review D* 105.6 (2022). DOI: 10.1103/physrevd.105.062004 (cited on page 14).

[61] R. Abbasi et al. “IceTop: The surface component of IceCube”. In: *Nuclear Instruments and Methods in Physics Research Section A: Accelerators, Spectrometers, Detectors and Associated Equipment* 700 (2013), pp. 188–220. DOI: https://doi.org/10.1016/j.nima.2012.10.067 (cited on page 14).

[62] R. Abbasi et al. “The IceCube data acquisition system: Signal capture, digitization, and timestamping”. In: *Nuclear Instruments and Methods in Physics Research Section A: Accelerators, Spectrometers, Detectors and Associated Equipment* 601.3 (2009), pp. 294–316. DOI: 10.1016/j.nima.2009.01.001 (cited on page 17).

[63] M. Ackermann et al. “Optical properties of deep glacial ice at the South Pole”. In: *J. Geophys. Res.* 111.D13 (2006), p. D13203. DOI: 10.1029/2005JD006687 (cited on page 18).

[64] M. Aartsen et al. “South Pole Glacial Climate Reconstruction from Multi-Borehole Laser Particulate Stratigraphy”. In: *Journal of Glaciology* 59 (Sept. 2013), pp. 1117–1129. DOI: 10.3189/2013JoG13J068 (cited on page 18).

[65] M. G. Aartsen et al. “Measurement of South Pole ice transparency with the IceCube LED calibration system”. In: *Nuclear Instruments and Methods in Physics Research Section A: Accelerators, Spectrometers, Detectors and Associated Equipment* 711 (May 2013), pp. 73–89. DOI: 10.1016/j.nima.2013.01.054 (cited on pages 18, 19).

[66] K. Woschnagg and D. Chirkin. “Age vs depth of glacial ice at South Pole”. In: *Geophysical Research Letters* 27 (July 2000), pp. 2129–2132. DOI: 10.1029/2000GL011351 (cited on page 18).

[67] R. Abbasi et al. “In situ estimation of ice crystal properties at the South Pole using LED calibration data from the IceCube Neutrino Observatory”. In: *The Cryosphere* 18.1 (2024), pp. 75–102. DOI: 10.5194/tc-18-75-2024 (cited on pages 19, 45).

[68] D. Chirkin et al. “An improved mapping of ice layer undulations for the IceCube Neutrino Observatory”. In: *PoS* ICRC2023 (2023), p. 975. DOI: 10.22323/1.444.0975 (cited on page 19).

[69] D. Hahn. “Light Scattering Theory”. In: (Jan. 2004) (cited on page 19).

[70] D. Chirkin and IceCube Collaboration. “Evidence of optical anisotropy of the South Pole ice”. In: *International Cosmic Ray Conference*. Vol. 33. International Cosmic Ray Conference. Jan. 2013, p. 3338 (cited on page 19).

[71] M. Usner. “Search for Astrophysical Tau-Neutrinos in Six Years of High-Energy Starting Events in the IceCube Detector”. PhD thesis. Humboldt-Universität zu Berlin, Mathematisch-Naturwissenschaftliche Fakultät, 2018. DOI: http://dx.doi.org/10.18452/19458 (cited on pages 19, 35).

[72] D. Chirkin and M. Rongen. “Light diffusion in birefringent polycrystals and the IceCube ice anisotropy”. In: *PoS* ICRC2019 (2019), p. 854 (cited on page 19).

[73] R. Abbasi et al. “A calibration study of local ice and optical sensor properties in IceCube”. In: *PoS* ICRC2021 (2021), p. 1023. DOI: 10.22323/1.395.1023 (cited on page 19).

[74] D. H. Perkins. *Particle astrophysics*. 2003 (cited on page 21).

[75] D. Chirkin and W. Rhode. “Propagating leptons through matter with Muon Monte Carlo (MMC)”. In: (Aug. 2004) (cited on pages 21, 22).

[76] L. Radel and C. Wiebusch. “Calculation of the Cherenkov light yield from electromagnetic cascades in ice with Geant4”. In: *Astropart. Phys.* 44 (2013), pp. 102–113. DOI: 10.1016/j.astropartphys.2013.01.015 (cited on pages 21, 23).

[77] L. D. Landau and I. Pomeranchuk. “Limits of applicability of the theory of bremsstrahlung electrons and pair production at high-energies”. In: *Dokl. Akad. Nauk Ser. Fiz.* 92 (1953), pp. 535–536 (cited on page 21).

[78] L. D. Landau and I. Pomeranchuk. “Electron cascade process at very high-energies”. In: *Dokl. Akad. Nauk Ser. Fiz.* 92 (1953), pp. 735–738 (cited on page 21).

[79] A. B. Migdal. "Bremsstrahlung and Pair Production in Condensed Media at High Energies". In: *Phys. Rev.* 103 (6 Sept. 1956), pp. 1811–1820. DOI: 10.1103/PhysRev.103.1811 (cited on page 21).

[80] C. A. Argüelles et al. "Tau depolarization at very high energies for neutrino telescopes". In: *Phys. Rev. D* 106.4 (2022), p. 043008. DOI: 10.1103/PhysRevD.106.043008 (cited on page 22).

[81] P. A. Cherenkov. "Visible radiation produced by electrons moving in a medium with velocities exceeding that of light". In: *Phys. Rev.* 52.4 (1937), pp. 378–379. DOI: 10.1103/PhysRev.52.378 (cited on page 23).

[82] I. M. Frank and I. E. Tamm. "Coherent visible radiation of fast electrons passing through matter". In: *Compt. Rend. Acad. Sci. URSS* 14.3 (1937). Ed. by V. L. Ginzburg, B. M. Bolotovsky, and I. M. Dremin, pp. 109–114. DOI: 10.3367/UFNr.0093.196710o.0388 (cited on page 23).

[83] M. G. Aartsen et al. "Energy Reconstruction Methods in the IceCube Neutrino Telescope". In: *JINST* 9 (2014), P03009. DOI: 10.1088/1748-0221/9/03/P03009 (cited on page 24).

[84] D. F. Cowen. "Tau neutrinos in IceCube". In: *J. Phys. Conf. Ser.* 60 (2007). Ed. by F. Halzen, A. Karle, and T. Montaruli, pp. 227–230. DOI: 10.1088/1742-6596/60/1/048 (cited on pages 24, 25).

[85] J. G. Learned and S. Pakvasa. "Detecting tau-neutrino oscillations at PeV energies". In: *Astropart. Phys.* 3 (1995), pp. 267–274. DOI: 10.1016/0927-6505(94)00043-3 (cited on page 25).

[86] R. Abbasi et al. "Observation of Seven Astrophysical Tau Neutrino Candidates with IceCube". In: *Phys. Rev. Lett.* 132.15 (2024), p. 151001. DOI: 10.1103/PhysRevLett.132.151001 (cited on page 25).

[87] O. Behnke and L. Moneta. *Parameter Estimation*. John Wiley and Sons, Ltd, 2013. Chap. 2, pp. 27–73 (cited on page 30).

[88] S. S. Wilks. "The Large-Sample Distribution of the Likelihood Ratio for Testing Composite Hypotheses". In: *Annals Math. Statist.* 9.1 (1938), pp. 60–62. DOI: 10.1214/aoms/1177732360 (cited on pages 31, 54).

[89] G. J. Feldman and R. D. Cousins. "Unified approach to the classical statistical analysis of small signals". In: *Phys. Rev. D* 57 (7 Apr. 1998), pp. 3873–3889. DOI: 10.1103/PhysRevD.57.3873 (cited on page 31).

[90] B. Sen, M. Walker, and M. Woodroofe. "On the unified method with nuisance parameters". In: *Statistica Sinica* 19 (Jan. 2009), pp. 301–314 (cited on page 31).

[91] G. Cowan et al. "Asymptotic formulae for likelihood-based tests of new physics". In: *Eur. Phys. J. C* 71 (2011). [Erratum: Eur.Phys.J.C 73, 2501 (2013)], p. 1554. DOI: 10.1140/epjc/s10052-011-1554-0 (cited on pages 31, 32, 57).

[92] C. A. Argüelles, A. Schneider, and T. Yuan. "A binned likelihood for stochastic models". In: *JHEP* 06 (2019), p. 030. DOI: 10.1007/JHEP06(2019)030 (cited on page 32).

[93] R. Abbasi et al. "IceCube high-energy starting event sample: Description and flux characterization with 7.5 years of data". In: *Physical Review D* 104.2 (2021). DOI: 10.1103/physrevd.104.022002 (cited on pages 34–36, 38, 45, 50, 61, 66).

[94] A. Fedynitch et al. "Calculation of conventional and prompt lepton fluxes at very high energy". In: *EPJ Web Conf.* 99 (2015). Ed. by D. Berge et al., p. 08001. DOI: 10.1051/epjconf/20159908001 (cited on page 34).

[95] T. K. Gaisser. "Spectrum of cosmic-ray nucleons, kaon production, and the atmospheric muon charge ratio". In: *Astroparticle Physics* 35.12 (2012), pp. 801–806. DOI: https://doi.org/10.1016/j.astropartphys.2012.02.010 (cited on page 34).

[96] F. Riehn et al. "The hadronic interaction model SIBYLL 2.3c and Feynman scaling". In: *PoS* ICRC2017 (2018), p. 301. DOI: 10.22323/1.301.0301 (cited on page 34).

[97] R. Abbasi et al. "Improved Characterization of the Astrophysical Muon–neutrino Flux with 9.5 Years of IceCube Data". In: 928.1 (2022), p. 50. DOI: 10.3847/1538-4357/ac4d29 (cited on pages 34, 61, 70).

[98] H. M. Niederhausen. "Measurement of the High Energy Astrophysical Neutrino Flux Using Electron and Tau Neutrinos Observed in Four Years of IceCube Data". PhD thesis. Stony Brook U., 2018 (cited on page 34).

[99] G. D. Barr et al. "Uncertainties in Atmospheric Neutrino Fluxes". In: *Phys. Rev. D* 74 (2006), p. 094009. DOI: 10.1103/PhysRevD.74.094009 (cited on page 34).

[100] A. Fedynitch and M. Huber. "Data-driven hadronic interaction model for atmospheric lepton flux calculations". In: *Phys. Rev. D* 106.8 (2022), p. 083018. DOI: 10.1103/PhysRevD.106.083018 (cited on page 35).

[101] R. Naab. "Evidence for a Break in the Diffuse Extragalactic Neutrino Spectrum". PhD thesis. Humboldt-Universität zu Berlin, Mathematisch-Naturwissenschaftliche Fakultät, 2024 (cited on pages 35, 36, 41).

[102] J. Stachurska. "Astrophysical Tau Neutrinos in IceCube". PhD thesis. Humboldt-Universität zu Berlin, Mathematisch-Naturwissenschaftliche Fakultät, 2020. DOI: http://dx.doi.org/10.18452/21611 (cited on pages 35, 56).

[103] M. G. Aartsen et al. "Efficient propagation of systematic uncertainties from calibration to analysis with the SnowStorm method in IceCube". In: *JCAP* 10 (2019), p. 048. DOI: 10.1088/1475-7516/2019/10/048 (cited on page 35).

[104] P. Eller et al. "A model independent parametrization of the optical properties of the refrozen IceCube drill holes". In: *PoS* ICRC2023 (2023), p. 1034. DOI: 10.22323/1.444.1034 (cited on page 37).

[105] R. Abbasi et al. "Detection of astrophysical tau neutrino candidates in IceCube". In: *The European Physical Journal C* 82.11 (2022). DOI: 10.1140/epjc/s10052-022-10795-y (cited on pages 37, 45, 55, 56, 67).

[106] N. Lad et al. "Summary of IceCube tau neutrino searches and flavor composition measurements of the diffuse astrophysical neutrino flux". In: *PoS* ICRC2023 (2023), p. 1122. DOI: 10.22323/1.444.1122 (cited on pages 38, 70).

[107] R. Naab et al. "Measurement of the astrophysical diffuse neutrino flux in a combined fit of IceCube's high energy neutrino data". In: *PoS* ICRC2023 (2023), p. 1064. DOI: 10.22323/1.444.1064 (cited on pages 43, 60).

[108] V. Basu et al. "From PeV to TeV: Astrophysical Neutrinos with Contained Vertices in 10 years of IceCube Data". In: *PoS* ICRC2023 (2023), p. 1007. DOI: 10.22323/1.444.1007 (cited on page 43).

[109] T. Yuan. "Detecting neutrinos in IceCube with Cherenkov light in the South Pole ice". In: *Nucl. Instrum. Meth. A* 1054 (2023), p. 168440. DOI: 10.1016/j.nima.2023.168440 (cited on page 45).

[110] V. Basu et al. "From PeV to TeV: Astrophysical Neutrinos with Contained Vertices in 10 years of IceCube Data". In: *PoS* ICRC2023 (2023), p. 1007. DOI: 10.22323/1.444.1007 (cited on page 60).

[111] M. G. Aartsen et al. "Characteristics of the Diffuse Astrophysical Electron and Tau Neutrino Flux with Six Years of IceCube High Energy Cascade Data". In: *Phys. Rev. Lett.* 125 (12 Sept. 2020), p. 121104. DOI: 10.1103/PhysRevLett.125.121104 (cited on page 61).

[112] M. G. Aartsen et al. "IceCube-Gen2: the window to the extreme Universe". In: *Journal of Physics G: Nuclear and Particle Physics* 48.6 (2021), p. 060501. DOI: 10.1088/1361-6471/abbd48 (cited on page 63).

[113] A. Ishihara. "The IceCube Upgrade - Design and Science Goals". In: *PoS* ICRC2019 (2021), p. 1031. DOI: 10.22323/1.358.1031 (cited on page 63).

[114] IceCube Collaboration and F. Schröder. *IceCube-Gen2 Surface Array: Science Case and Plans*. Vortrag gehalten auf DPG Frühjahrstagung: Fachverband Teilchenphysik (2024), Karlsruhe, Deutschland, 4.–8. März 2024. 51.13.04; LK 01. 2024 (cited on page 63).

[115] G. A. Askar'yan. "Excess negative charge of an electron-photon shower and its coherent radio emission". In: *Zh. Eksp. Teor. Fiz.* 41 (1961), pp. 616–618 (cited on page 64).

[116] Z. S. Meyers et al. *Radio Detection of EeV Neutrinos in Dielectric Media using the Askaryan Effect* *for Babies*. DESY, 2021, pp. 1–14 (cited on page 64).

[117] R. "Abbasi and others". *The IceCube Gen2 Technical Design Report*. https://icecube-gen2.wisc.edu/wp-content/uploads/2023/07/IceCube_Gen2_TDR_0.05_July27.2023_Part_I_and_II.pdf. [Accessed 18-06-2024]. 2023 (cited on pages 64, 65, 72).

[118] L. Classen et al. "The mDOM - A multi-PMT digital optical module for the IceCube-Gen2 neutrino telescope". In: *PoS* ICRC2017 (2017), p. 1047. DOI: 10.22323/1.301.1047 (cited on page 65).

[119] L. Classen et al. "A multi-PMT Optical Module for the IceCube Upgrade". In: *PoS* ICRC2019 (2019), p. 855. DOI: 10.22323/1.358.0855 (cited on page 65).

[120] R. Abbasi et al. "D-Egg: a dual PMT optical module for IceCube". In: *JINST* 18.04 (2023), P04014. DOI: 10.1088/1748-0221/18/04/P04014 (cited on page 65).

[121] M. "Aartsen et al. "Letter of Intent: The Precision IceCube Next Generation Upgrade (PINGU)". In: *E-Print: arXiv* 1401.2046 [physics.ins-det] (Jan. 2014) (cited on page 65).

[122] A. Omeliukh. "Optimization of the optical array geometry for IceCube-Gen2". Master's thesis. Kyiv, Ukraine: Taras Schevchenko national University of Kyiv, 2021 (cited on page 65).

[123] M. Bustamante, J. F. Beacom, and W. Winter. "Theoretically Palatable Flavor Combinations of Astrophysical Neutrinos". In: *Phys. Rev. Lett.* 115 (16 Oct. 2015), p. 161302. DOI: 10.1103/PhysRevLett.115.161302 (cited on pages 68, 71).

[124] A. Coleman et al. "The flavor composition of ultra-high-energy cosmic neutrinos: measurement forecasts for in-ice radio-based EeV neutrino telescopes". In: (Feb. 2024) (cited on page 68).

[125] J. van Santen et al. "toise: a framework to describe the performance of high-energy neutrino detectors". In: *Journal of Instrumentation* 17.08 (2022), T08009. DOI: 10.1088/1748-0221/17/08/t08009 (cited on page 68).

[126] N. Lad et al. "Sensitivity of IceCube-Gen2 to measure flavor composition of Astrophysical neutrinos". In: *PoS* ICRC2023 (2023), p. 1123. DOI: 10.22323/1.444.1123 (cited on page 70).

[127] M. G. Aartsen et al. In: *Astrophys. J.* 809.1 (2015), p. 98. DOI: 10.1088/0004-637X/809/1/98 (cited on page 70).